

Dissertation
submitted to the
Combined Faculties of the Natural Sciences and Mathematics
of the Ruperto-Carola University of Heidelberg, Germany
for the degree of
Doctor of Natural Sciences

Put forward by
Valeriy Vasilyev
born in Kugu-Shurga, Mari El Republic, USSR
Oral examination: February 7th, 2018

Dynamical model atmospheres for the abundance analysis of pulsating stars

Referees:

Prof. Dr. Norbert Christlieb

PD Dr. Andreas Koch

to my parents

SUMMARY

The chemical composition of Cepheid variables can provide information on the chemo-dynamical evolution of the Galaxy and beyond. The standard method for determining atmospheric parameters and abundances of Cepheids is based on one-dimensional plane-parallel hydrostatic model atmospheres, where convection is treated by Mixing Length Theory. The aim of the thesis is to investigate the impact of the atmospheric dynamics on observable spectroscopic properties. Two approaches are followed: firstly, I construct one-dimensional pulsating atmosphere models implementing a non-local, time-dependent theory of convection, and secondly check the validity of the quasi-static approach against a two-dimensional dynamical Cepheid model.

The spectroscopic analysis of the classical Cepheid KQ Scorpil with my one-dimensional model showed that pulsations do not produce strong enough velocity gradients in the line-formation region to explain the estimated microturbulent velocities. The spectroscopic investigation of the two-dimensional Cepheid model allowed to explain the residual line-of-sight velocity of Galactic Cepheids, long known as the “K-term”, by lineshifts of convective origin. Moreover, hydrostatic 1D model atmospheres can provide unbiased estimates of stellar parameters and abundances of Cepheids for particular phases of their pulsations. Summarizing, the main result is a change of paradigm in the context of spectroscopic investigations of Cepheids toward a greater importance of convection than thought previously.

ZUSAMMENFASSUNG

Die chemische Zusammensetzung von Cepheiden kann Informationen zur chemo-dynamischen Entwicklung unserer Galaxie und darüber hinaus liefern. Die Standardmethode zur Bestimmung der atmosphärischen Parameter und chemischen Häufigkeiten von Cepheiden basiert auf eindimensionalen planparallelen hydrostatischen Modellatmosphären, in denen Konvektion mit Hilfe der Mischungswegtheorie beschrieben wird. Ziel der Doktorarbeit ist es, die Auswirkungen der Dynamik der Atmosphäre auf beobachtbare spektrale Eigenschaften zu untersuchen.

Zwei Ansätze wurden nachgegangen: Erstens erstelle ich eindimensionale Modelle von pulsierenden Atmosphären, in die ich eine nichtlokale, zeitabhängige Konvektionstheorie implementiert habe, und zweitens prüfe ich die Gültigkeit des quasistatischen Ansatzes an einem zweidimensionalen dynamischen Modell eines Cepheiden.

Die Spektralanalyse des klassischen Cepheiden KQ Scorpil mit meinen eindimensionalen Modellen zeigt, dass Pulsationen keine Geschwindigkeitsgradienten in Bereichen, in denen Spektrallinien gebildet werden, hervorrufen, die stark genug sind, um die abgeschätzten mikroturbulenten Geschwindigkeiten zu erzeugen. Die Spektralanalyse des zweidimensionalen Modells eines Cepheiden ermöglichte es, die Restgeschwindigkeiten von galaktischen Cepheiden entlang der Sichtlinie, lange bekannt als “K-Term”, durch Linienverschiebungen zu erklären, die durch Konvektion verursacht sind. Zudem können hydrostatische 1D-Modellatmosphären verzerrungsfreie Abschätzungen der Atmosphärenparameter und Häufigkeiten von Cepheiden in bestimmten Phasen ihrer Pulsationen liefern. Zusammengefasst stellt das Hauptresultat einen Paradigmenwechsel im Hinblick auf spektrale Untersuchungen von Cepheiden dar, der auf eine grössere Bedeutung der Konvektion als bisher angenommen hinausläuft.

Contents

1	Introduction	4
1.1	The chemical evolution	4
1.1.1	Cosmological origin of chemical elements	4
1.1.2	Nucleosynthesis with cosmic rays	5
1.1.3	Nucleosynthesis in stars	6
1.1.4	The chemical evolution of the Galaxy	7
1.2	What is a stellar atmosphere?	8
1.3	Pulsating stars	12
1.3.1	Excitation of pulsations	12
1.3.2	The Period - Luminosity relation	13
1.3.3	The instability strip	14
1.3.4	Why are Cepheids of particular interest?	17
1.4	Dynamical models	19
1.5	The structure of this dissertation	20
2	One-dimensional dynamical atmosphere models	21
2.1	Some precursory trials and errors	21
2.2	The physical formulation of the problem	23
2.3	Convection in 1D	25
2.3.1	The criterion for convective stability	25
2.3.2	The mixing length theory	27
2.3.3	Stellingwerf's theory of convection	30
2.4	Radiative transfer	31
2.4.1	Calculation of the radiative flux	31

2.5	Boundary and initial conditions	32
2.5.1	Initial conditions	32
2.5.2	Excitation of pulsations	33
2.5.3	Boundary conditions	39
2.6	Numerical scheme of the LHD code.	39
2.6.1	Semi-implicit method for the update of energy equation	40
2.7	Numerical implementation of the Stellingwerf theory	44
2.7.1	Numerical scheme	45
2.7.2	Stability analysis	46
2.8	A model for the classical Cepheid KQ Scorpii	48
2.8.1	Observational data	48
2.8.2	The one-dimensional LHD model for KQ Scorpii	51
2.8.3	Theoretical line profiles and equivalent widths	53
2.9	Summary of the 1D modeling	56
3	Spectroscopic investigation of a 2D Cepheid model I.	59
3.1	Description of the 2D Cepheid model	60
3.1.1	Convective noise	66
3.1.2	Effects of the Cartesian geometry and grey radiative transfer	67
3.1.3	Relating velocity and luminosity amplitudes	69
3.2	Spectroscopic properties	69
3.2.1	Microturbulence	70
3.2.2	Spikes in the EW(t) curves	72
3.2.3	Line asymmetry	75
3.2.4	Line-depth ratio and the effective temperature	76
3.3	Interpretation of the "K-term"	78

3.4	Projection factor obtained from the 2D model	81
3.5	Summary	85
4	Spectroscopic investigation of a 2D Cepheid model II.	89
4.1	The grid of 1D LHD models	89
4.2	The list of artificial iron lines	91
4.3	Spectral line profiles of the dynamical 2D model	93
4.4	Methodology of the parameter fitting	95
4.4.1	Test with radial basis functions	97
4.4.2	Test with radial basis functions	97
4.4.3	Test with a quadratic form	97
4.4.4	Test with a sequence of cubic interpolations	98
4.5	Results and discussion	98
4.5.1	The four-parametric case	98
4.5.2	The three-parametric case	101
4.5.3	The two-parametric case	105
4.5.4	Connection between abundance and equivalent width fitting	106
4.5.5	Comparison of equivalent widths	107
4.6	Summary	107
5	Conclusions	110
5.1	Summary	110
5.2	Future plans	111
6	Supplementary Material	113
7	List of Abbreviations	116
8	Bibliography of own publications	117

1 INTRODUCTION

This PhD thesis is concerned with the study of atmospheres and spectroscopic properties of pulsating stars. Firstly, it describes physical and numerical aspects, including how I build one-dimensional pulsating stellar atmosphere models and apply them in chemical abundance analysis. Secondly, it describes a spectroscopic investigation of a multidimensional pulsating stellar atmosphere model. As we shall see in this introduction, the study of pulsating stellar atmospheres touches not only upon aspects of the structure and evolution of stars, but it has implications on the evolution of galaxies and the Universe as a whole. In order to prepare for the concepts presented in the following chapters and to understand the motivation for my work, in this introduction I look at the link between stellar atmosphere modeling, and the study of the chemical evolution of the Galaxy and the Universe. I explain physical mechanisms of excitations of pulsations, types of pulsating stars, and astrophysical and cosmological applications of these stars. Looking ahead, I argue that they will play an increasingly important role in astronomy. Since, in this work, the primary application of stellar atmosphere models is related to deriving stellar parameters, especially surface chemical abundances, I will start with a discussion on the origin of the elements and the chemical evolution of the Galaxy.

1.1 The chemical evolution

The world around us consists of above 90 different naturally-forming chemical elements. Their atomic nuclei are formed in nuclear reactions. Qualitatively, one can form heavier nuclei by synthesis from collisions between lighter elements, but the kinetic energy of colliding particles has to be sufficient to overcome the Coulomb barrier with the quantum tunneling effect and become bonded by the strong nuclear force. On the other hand, one can cleavage heavier nuclei into lighter by collisions. Nucleosynthesis occurs at different stages of the evolution of the Universe. Therefore, the chemical composition of the Universe has changed over the last 13.8 Gyr starting with metal-poor conditions.

1.1.1 Cosmological origin of chemical elements

Looking up at the night sky, the stars provide a stable reference against the often chaotic processes at work in our everyday lives. Throughout the life of a person, visible stars have an apparently unaltered brightness and location on the sky, keeping the habitual pattern of constellations. Only comets and planets slightly violate this apparent uniformity. However, the first impression of the immutability of the Universe is deceptive. The Universe is expanding (Hubble, 1929), and, according to observations of Ia supernovae by Perlmutter et al. (1999), the expansion is accelerating. If it is expanding, one can immediately extrapolate it back in time and assume, that

during its earlier evolution the Universe was hotter and denser than it is today (Lemaître, 1927).

Penzias and Wilson (1965) discovered the Cosmic Microwave Background (CMB), which is the radiation coming from all direction on the sky and having a close to black-body spectrum with a temperature of 2.73 K. The CMB is an echo of the hot early stage of the Universe, 10^5 years after the Big Bang. Then it was the optical radiation of a hot gas with a temperature of several thousands of Kelvins uniformly filling the entire Universe. During the expansion of the Universe, the temperature of the CMB diminished by a factor of thousand. The CMB was predicted by Gamow (1946) in the theory of Big Bang Nucleosynthesis (BBN). For temperatures $E = k_b T$ higher than 1 MeV, atomic nuclei cannot survive as they are destroyed by photons into individual nucleons, protons and neutrons. However, as the Universe cooled and expanded, protons and neutrons started to merge together and produced deuterium (D). Nuclear reactions with deuterium synthesized helium (^3He and ^4He). Helium "burned" into more heavy elements, lithium (^7Li) and beryllium (^7Be). Nevertheless, this reactions were going slower, because of absence in nature of the element with the atomic number 5 and 8. Additionally, the ^7Be nucleus is unstable, by β -decay it decays into ^7Li . Due to the cooling of the Universe, after $\approx 10^3$ s the further nuclear reactions have become impossible. It turns out, the standard BBN (Walker et al., 1991) predicts a primordial helium ^4He mass fraction of $\approx 24\%$. The primordial hydrogen mass fraction is $\sim 76\%$. ^4He is accompanied by lesser amounts of D and ^3He , $\text{D}/\text{H} \approx 10^{-5}$ and $^3\text{He}/\text{H} \approx 10^{-5}$ (by number). In the standard model ^7Li was produced with even lower abundances $^7\text{Li}/\text{H} \sim 10^{-10}$. The BBN also can predict the primordial abundances of isotopes of light elements (Smith et al., 1993), namely ^6Li , ^9Be , ^{10}B and ^{11}B , but their abundances are much smaller.

The recent Planck mission (Planck Collaboration et al., 2016) has analyzed the CMB and has allowed to determine to high precision the baryon-to-photon ratio as well as the primordial abundances, and has provided constrains on nuclear reaction rates. The CMB can thus tell us the state of the Universe 10^5 years after the Big Bang. To obtain information about the Universe at earlier epochs, one can study, for example, the ^7Li abundance. However, in order to do so in an accurate fashion, one has to take into account later production in particular by Galactic cosmic-ray nucleosynthesis (Fields and Olive, 1999).

1.1.2 Nucleosynthesis with cosmic rays

The light elements lithium, beryllium, and boron are difficult to produce in stars because of their small binding energies. They are destroyed at relatively low temperatures in stellar interiors.

Currently, the most plausible channel of production of Be and B is an interaction of the Galactic Cosmic Rays (GCR) with the interstellar medium (ISM), especially with C, N, and O nuclei. GCR particles, protons and α -particles, are efficiently accelerated in shock waves during supernovae explosions. Finally, collision of GCR particles with C, N, and O nuclei leads spallation of this heavier elements into lighter elements.

1.1.3 Nucleosynthesis in stars

After 13 Gyr of evolution of the Universe, its chemical composition has changed. The measurement of the solar chemical composition by Asplund et al. (2009) using a realistic three-dimensional (3D), time-dependent hydrodynamical model of the solar atmosphere shows, that the mass fraction of hydrogen is 73.81%, helium is 24.85%, and rest of elements is 1.34%.

Additionally, we can ask ourselves, where we came from, because we are a life form based on carbon. For the existence of our life, in addition to carbon, we need oxygen, and indeed most of the elements found in the periodic table. These elements are formed by stars, in one way or another. The first generation of stars had the primordial chemical composition. In interiors of the stars successive processes of thermonuclear burning of helium, carbon, and silicon were occurring, and in the latter process, most elements of the iron peak are synthesized. The first stars were very heavy and evolved rather quickly (Siess et al., 2002; Umeda and Nomoto, 2003), the final stage of the evolution of such stars was powerful explosions, which threw heavy elements synthesized in their interiors into the interstellar medium. Ejected into the interstellar medium, these heavy metals intermixed with hydrogen and helium. As a result, it was possible to form next generations of stars with higher metal content, such as, for example, our Sun. From this interstellar gas, enriched with carbon, oxygen and heavier elements, planetary systems were formed, and on one such planetary systems our life appeared.

In the case of the Sun, the main channel of energy production is the pp -cycle, in which four protons form an α -particle, ${}^4\text{He}$ nucleus. After the main sequence and contraction of the stellar core helium "burns" into carbon ${}^{12}\text{C}$ in the triple alpha-process. An additional reaction can occur, in which ${}^{12}\text{C}$ can be converted to ${}^{16}\text{O}$ releasing energy and ${}^{16}\text{O}$ into ${}^{20}\text{Ne}$. Further compression of the stellar core leads to an increase in temperature and the continuation of the subsequent chain of thermonuclear reactions. The number of progressive thermonuclear reactions is different between the low- and high-mass stars. For example, brown dwarfs with $M < 0.08$ solar masses (M_{\odot}) do not have a high enough temperature for hydrogen burning. In massive stars ($M > 8M_{\odot}$) the chain of reactions stops at iron, because the iron nucleus has the largest binding energy per nucleon, and the synthesis of heavier nuclei is energetically not beneficent.

Together with the production of new elements, neutrons are also one of the results of the thermonuclear reactions. Physically, the stellar core becomes more and more enriched in neutrons during the final stages of the stellar evolution. As a result, slow neutron captures can take place (the so-called s-process), and can form neutron-enriched nuclei, which subsequently undergo β -decay. The s-process happens in the stage of a red giant, when the neutron density in the stellar core is around $n_n \approx 10^{10} \text{ cm}^{-3}$. The formation of elements up to $Z=83$ can be explained by the s-process. Nuclei with $Z=84-89$ do not have stable isotopes and are radioactive. Therefore, it is impossible to overcome this region of Z in the s-process. At the same time in nature there are heavier nuclei. To explain the existence of these nuclei, it is necessary to take them as a result of

the rapid capture of neutrons by unstable nuclei.

The origin of heavier nuclei is explained by rapid neutron capture, via the so-called r-process. The rapid capture where the time scale for neutron capture is much shorter than the time for β decay ($t_r \ll \tau_\beta$) leads to the formation of heavier nuclei. For a short time during a supernova explosion the density of neutrons can be around 10^{20} cm^{-3} , and nuclei are overloaded with neutrons. Undergoing subsequent β -decays they can potentially form the heaviest elements. However, results of simulations of the production of r-process elements in supernova explosions are not consistent with observed abundances (Freiburghaus et al., 1997, 1999a). In order to get agreement with observations it was necessary to change the weak interaction properties (Engel et al., 1999; Martínez-Pinedo and Langanke, 1999) or cross sections of reactions (Fuller and Meyer, 1995). Freiburghaus et al. (1999b) performed calculations of the nucleosynthesis during the coalescence of two neutron stars and showed that this scenario can explain the amount of r-process nuclei in the Galaxy. Recently, such an event was observed by ground-based and space telescopes in different electromagnetic bands, as well as by the LIGO¹ and VIRGO² gravitational-wave antennas (Abbott et al., 2017). For this event Drout et al. (2017) estimated r-process heating and ejecta properties. However, detailed cross sections of r-process reactions are not very well-known in comparison to s-process cross sections. The reason is that measurements of the r-process cross sections are essentially non-existent since one cannot produce the necessary high neutron densities in the laboratory.

Because for cross sections measurements it is impracticable to produce high neutron densities in laboratory conditions.

1.1.4 The chemical evolution of the Galaxy

The Galaxy consists of a many components, which are evolving and interacting with each other. The chemical evolution of the Milky Way (MW) is controlled by a large number of processes, including, interaction of the Galaxy with surrounding galaxies, merging with dwarf galaxies and accretion of the circum-galactic gas, star formation, stellar evolution, and supernova feedback, migration of stars and dynamical effects in the Galactic disk. The study of elemental abundances in different stellar populations and Galactic components helps to restore the history of merging events and the chemical composition of gas clouds, from which they were formed, taking into account the impact of the stellar evolution on the chemical composition.

The measurement of elemental abundances in stars is based on the analysis of stellar spectra. A number of ongoing large spectroscopic surveys are investigating different components of the Galaxy, such as the Gaia-ESO survey (Gilmore et al., 2012), the Apache Point Observatory Galactic Evolution Experiment (APOGEE) (Allende Prieto et al., 2008), The Galactic Archaeology with HER-

¹<http://www.ligo.org/>

²<http://www.virgo-gw.eu/>

MES survey (GALAH) (Zucker et al., 2012), as well as proposed 4-metre Multi-Object Spectroscopic Telescope (de Jong et al., 2014).. These surveys intend to get detailed elemental abundances for hundreds of thousands to millions of stars. Combining this data with information about distance measurements and proper motions for the stars, one can put additional constrains on the chemodynamical evolution of the Galaxy. To infer elemental abundances, one needs to compare the observed spectra to theoretical, synthetic spectra. Synthetic spectra, in its turn, are based on stellar atmosphere models.

1.2 What is a stellar atmosphere?

Most of information about physical conditions in stars, their chemical composition is based on the analysis of the emitted radiation field in ultraviolet, optical and infrared bands. The radiation field at point \mathbf{r} is characterized by the specific intensity $I_\nu(\mathbf{r}, \mathbf{n}, t)$

$$I_\nu = \frac{dE}{\cos\theta dA dt d\nu d\Omega}, \quad (1)$$

which is an energy passing the surface element with an area of dA along a direction, which has an angle of θ to the normal vector \mathbf{n} of the surface, in the solid angle of $d\Omega$ within a frequency range of $d\nu$. The mean intensity is defined as the zero order angular moment of the radiation field

$$J_\nu(\mathbf{r}, t) = \frac{1}{4\pi} \oint I_\nu(\mathbf{r}, \mathbf{n}, t) d\Omega. \quad (2)$$

The radiation flux is the first order moment of the radiation field

$$F_\nu = \oint I_\nu(\mathbf{r}, \mathbf{n}, t) \mathbf{n} d\Omega. \quad (3)$$

The observed radiation is emitted by the stellar atmosphere, which is geometrically thin compared to the stellar radius. Within the stellar atmosphere the stellar material has a transition from "transparent" to "opaque" for the propagating radiation field. In order to characterize quantitatively, what is the "transparent" and "opaque" stellar material I will consider, how radiation field propagates in the stellar atmosphere. A fraction of photons can be emitted or absorbed. The change of the intensity of the radiation field during propagation of photons for a distance ds in the stellar material with emitting properties one can write in a form of

$$dI_\nu = j_\nu ds, \quad (4)$$

where j_ν is the emission coefficient characterizing emitted energy by an volume element in a frequency range of ν , $\nu + d\nu$ along the direction with the solid angle of $d\Omega$. In order to characterize the absorbed fraction of the intensity one can write

$$dI_\nu = -\kappa_\nu I_\nu ds, \quad (5)$$

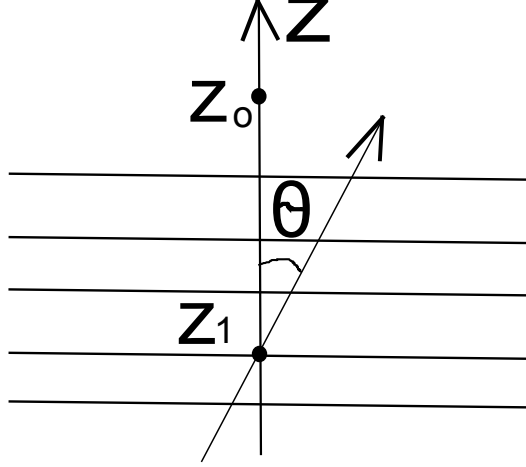


Figure 1: Scheme of the plane-parallel atmosphere. The vertical axis z is the geometrical depth.

where $[\kappa_\nu] = \text{cm}^{-1}$ is an opacity, which has contributions of free-free, bound-free, bound-bound transitions and scattering. Let us consider a plane-parallel, horizontally homogenous, atmosphere, where all parameters depend on geometrical depth z , and θ is the zenith angle as shown in Fig. 1. The length element ds along a ray with an inclination of $\mu = \cos\theta$ is related with the corresponding depth change $ds = dz/\mu$. Thus, combining Eq. 4 and 5 one can get the radiative transfer equation, describing propagation of the stationary radiation field ($\frac{dI_\nu}{dt} = 0$) in a plane-parallel atmosphere:

$$\mu \frac{dI_\nu(\tau_\nu, \mu)}{d\tau_\nu} = I_\nu(\tau_\nu, \mu) - S_\nu(\tau_\nu, \mu), \quad (6)$$

where $S_\nu(\tau_\nu, \mu) = \frac{j_\nu}{\kappa_\nu}$ is the source function, and $d\tau_\nu = -\kappa_\nu dz$ is the optical depth. Instead of the geometrical scale one can use the optical depth scale, $\tau_\nu(z = \infty) = 0$ and

$$\tau_\nu(z_1) = \int_{z_1}^{\infty} \kappa_\nu dz, \quad (7)$$

at deep regions of the atmosphere $\tau_\nu \rightarrow \infty$. The formal solution of the Eq. 6 for the radiation going outward ($\mu \geq 0$) at the optical depth of τ_ν is

$$I_\nu(\tau_\nu, \mu) = \int_{\tau_\nu}^{\infty} S_\nu(t) \exp(-(t - \tau_\nu)/\mu) dt / \mu. \quad (8)$$

At deep regions ($\tau_\nu \gg 1$) the mean free path of the photon is very short with respect to the characteristic geometrical scale of the change of the temperature. Propagation of photons one can describe as a diffusion process. Due to the frequent interactions of photons with the stellar material they are thermalized. The condition is very close to the thermodynamic equilibrium, so that the source function is the Planck function B_ν . The radiation field is almost isotropic and can be described according, in the energy transport can be described by a diffusion process. To see

this, one can represent the source function as a power series (Mihalas, 1978)

$$S_\nu(t_\nu) = B_\nu(\tau_\nu) + \frac{dB_\nu}{d\tau_\nu}(t_\nu - \tau_\nu) + \dots \quad (9)$$

Then, taking Eq. 9 one can represent the formal solution given by Eq. 8 for $0 \leq \mu \leq 1$ in a form

$$I_\nu(\tau_\nu, \mu) \approx B_\nu(\tau_\nu) + \mu \frac{dB_\nu}{d\tau_\nu}, \quad (10)$$

representing the mean intensity given by Eq. 2 as

$$J_\nu(\tau_\nu) \approx B_\nu(\tau_\nu), \quad (11)$$

and the monochromatic flux (Eq. 3) as

$$F_\nu(\tau_\nu) \approx \frac{4\pi}{3} \frac{dB_\nu}{d\tau_\nu}. \quad (12)$$

In Eq. 12 one can transform the gradient of the source function into a temperature gradient and gets

$$F_\nu(\tau_\nu) = -\frac{4\pi}{3\kappa_\nu} \frac{\partial B_\nu}{\partial T} \frac{dT}{dz}. \quad (13)$$

Finally, in order to get the total flux one has to integrate Eq. 13 over all frequencies

$$F = -\frac{4\pi}{3} \frac{dT}{dz} \int_0^\infty \frac{\partial B_\nu}{\partial T} \frac{1}{\kappa_\nu} d\nu. \quad (14)$$

This motivates the introduction of an averaged opacity, κ_R , called the Rosseland mean opacity, which satisfies

$$\frac{1}{\kappa_R} \int_0^\infty \frac{\partial B_\nu(T)}{\partial T} d\nu \equiv \int_0^\infty \frac{\partial B_\nu(T)}{\partial T} \frac{1}{\kappa_\nu} d\nu. \quad (15)$$

The frequency integral of the Planck function is given by the Stefan-Boltzmann law as

$$\int_0^\infty B_\nu(T) d\nu = \frac{\sigma}{\pi} T^4, \quad (16)$$

where σ is the Stefan-Boltzmann constant. Finally, one can write the total flux with help of the Rosseland mean as

$$F = -\frac{16\pi}{3} \sigma T^3 \frac{1}{\kappa_R} \frac{dT}{dz}. \quad (17)$$

One can directly calculate the total flux with Eq. 17 for a given thermal structure $\frac{dT}{dz}$. In deep regions of the stellar atmosphere the matter is optically thick, $\tau_R \gg 1$. At the upper regions there is a transition into the optically thin regime, where $\tau_R \ll 1$. In other words, in the "transparent" regions the mean free path of photons is longer than the typical spatial scale of the region. The radiation field here has non-local properties. The region near the transition between two the regimes with $\tau_R \sim 1$ is called the stellar photosphere. The photosphere emits the main fraction of the observable light. While the spectral continuum is formed in deep photospheric layers, lines are

typically formed in the higher and cooler layers. This happens since the stellar material remains optically thick for bound-bound transitions.

Traditionally, stellar atmosphere models are based on several assumptions:

1. The atmosphere is in hydrostatic equilibrium, when the gradient of the total pressure ∇p everywhere on the atmosphere is balanced by gravity

$$\frac{\nabla p}{\rho} = -g, \quad (18)$$

where g is the gravitational acceleration.

2. The atmosphere is in a local thermodynamic equilibrium (LTE). This means that the ionization balance is described by the Saha equation, the population of energy levels in atoms and ions is governed by the Boltzmann statistics. The source function is given by the Planck function.
3. The atmosphere is one-dimensional (1D), i.e. the structure of the atmosphere is a function of the depth. Physically, it implies horizontal homogeneity of the stellar atmosphere within a given depth or layer. The atmosphere can have a spherically-symmetric or plane-parallel geometry. The plane-parallel approximation is applicable to solar-like stars on the main sequence. The pressure scale height of the solar atmosphere is of the order of hundred kilometers which is much smaller than the stellar radius. Heiter and Eriksson (2006) investigated the effect of a geometric inconsistency in the calculation of synthetic spectra of giant stars. Geometry has a smaller effect on line formation than on the model atmosphere structure.
4. Energy in the stellar atmosphere can be transported by radiation or convection. The multi-dimensional phenomenon of convection is described with Mixing Length Theory, which will be described in the following sections.

With these assumptions, for example, Kurucz (1992) calculated plane-parallel stellar atmosphere models for a wide range of effective temperatures, surface gravities and chemical compositions (metallicities). For detailed studies of late-type stars ($T < 10000$ K) Gustafsson et al. (2008) calculated a grid of MARCS models in spherical symmetry. Comparing theoretical with observed spectra one can derive stellar parameters, such as the effective temperature T_{eff} , surface gravity acceleration and elemental abundances. For the analysis of non-pulsating stars, these assumptions are valid.

However, there are classes of stars which are variable due to pulsations. The atmospheres of these stars are not in hydrostatic equilibrium. In order to avoid biases in derived stellar parameters due to the incorrect model assumption of hydrostatic equilibrium, it is desirable to construct

dynamical stellar atmospheres of pulsating stars, and to check the validity of the hydrostatic approximation.

1.3 Pulsating stars

In the context of this thesis I restrict myself to radial pulsations where the planar or spherically shaped layers of the model atmosphere move only vertically up and down. In the following I will describe the mechanism by which the star taps into the radiation energy propagating from the center toward the surface and converts it into mechanical – pulsational – energy.

1.3.1 Excitation of pulsations

Eigenfrequencies of radial oscillations of gaseous self-gravitating spheres were investigated by Eddington (1926). In order to get excitation of pulsations the opacity of the stellar material has to increase during contraction absorbing more light, and decrease during the expansion. Partially ionized gas might provide the excitation of pulsations. Zhevakin (1957, 1963) showed, that regions of partially ionized helium below the photosphere can effectively excite pulsations. The mechanism of excitation emerging from opacity variations in zones of partial ionization is called the $\kappa - \gamma$ mechanism.

Bound-free and free-free transitions are dominating the opacity in deep regions of a star so that one can apply the Kramers' law for the mean Rosseland opacity of the stellar material with temperature of T and density ρ

$$\kappa_R \approx C\rho^2 T^{-7/2}, \quad (19)$$

where C is a constant depending on the chemical composition. An adiabatic compression changing the volume V of an element of neutral or fully ionized gas with pressure p by ΔV transforms the performed work $\Delta A = p\Delta V$ into kinetic energy $\Delta K = \frac{1}{2} m \Delta v^2$ of the gas particles (with mass m and mean velocity v) which corresponds to an increase of the temperature $\Delta T \sim \Delta v^2$. Assuming Kramers' opacity law to hold the increased temperature induces a decrease in the opacity (and vice-versa). Therefore, oscillations are damped because the stellar material is becoming more transparent during compression.

However, partially ionized gas has an increased heat capacity. During an adiabatic compression it stores work in the ionization of neutral atoms, so that the gas temperature as such changes only rather slightly. As a result, density variations dominate the change of the opacity. During compressions the stellar material can accumulate heat, which leads to an amplification of oscillations.

From a thermodynamic point of view one can consider a layer of the stellar material as an elementary heat engine. Work, which is done by the heat engine due to the passage of radiation, can be

positive (exciting oscillations) or negative (damping oscillations). Considering the whole star as a set of heat engines, in order to excite stellar pulsations one has to have a positive work over all layers $A > 0$. Otherwise, for $A < 0$ the star is stable against pulsations, and oscillations are going to be damped.

As the amplitude of an oscillation is growing in stars that are prone to pulsations, the opacity tends to grow during the maximum compression phase, and it leads to a growth of the work per pulsation cycle. However, the amplitude stops to grow when all atoms are ionized, and according Eq. 19, the opacity is controlled by temperature again. The stellar material becomes more transparent and, as a consequence, the mechanical work per cycle decreases. At the point when the the amplitude of pulsations no longer grows the star has reached the so-called limit cycle. The time scale to reach the limit cycle is short compared to the lifetime of a star in the pulsating phase so that typically stellar pulsations have reached a limit cycle.

1.3.2 The Period - Luminosity relation

The period P of pulsations of a star with mass M and radius R is related with its mean density according to $\bar{\rho} = \frac{3M}{4\pi R^3}$ (Eddington, 1926):

$$P\sqrt{\bar{\rho}} = Q, \quad (20)$$

where Q is a pulsational constant, which is a slowly varying function depending on the structure of the star. The luminosity of a star is related to its effective temperature and radius according to

$$L = 4\pi R^2 \sigma T_{\text{eff}}^4. \quad (21)$$

Combining Eq. 20 and 21 one can get the Period-Luminosity-Mass (PLM) relation

$$P \sim \frac{QL^{3/4}}{T_{\text{eff}}^3 \sqrt{M}}. \quad (22)$$

With stellar evolution models one can derive the Mass-Luminosity relation (LM) and transform Eq. 22 into a Period-Luminosity (PL) relation. Another commonly used method of derivation and calibration of the Period-Luminosity-Color (PLC), PLM, and PL relations is based on the dynamical non-linear stellar models of pulsating stars (Bono et al., 1999a, 2001; Ngeow et al., 2012).

However, the PL and PLC relations initially were discovered empirically (Leavitt, 1908; Leavitt and Pickering, 1912). These relations may be exploited to measure distances in the Universe (Riess et al., 2016). The PL relations for different types of pulsating stars are shown in Fig. 2.

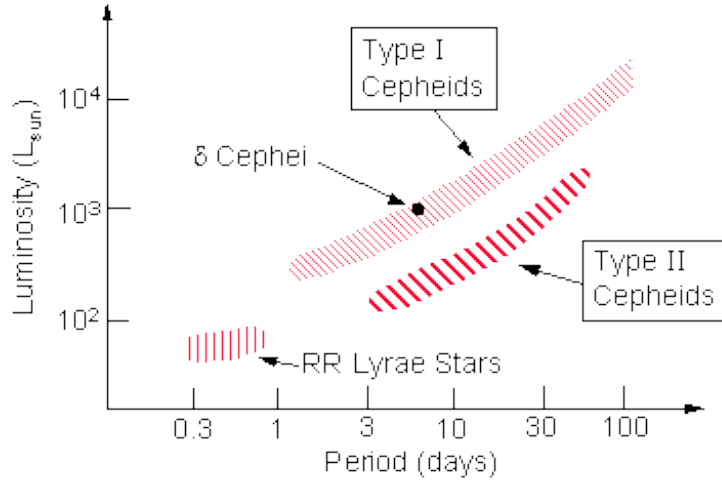


Figure 2: The period luminosity relation for classical pulsators, Cepheids and RR Lyraes. Image credits: http://ircamera.as.arizona.edu/astr_250/

1.3.3 The instability strip

During their evolution stars may pass through ranges in temperature, luminosity and metallicity where the $\kappa-\gamma$ mechanism can operate and excite pulsations. In the Hertzsprung-Russell-Diagram (H-R diagram) pulsating variable stars occupy the so-called "Instability Strip" which is shown in Fig. 3. In particular, the classical pulsating stars, RR Lyraes and Cepheids, are lying in the strip together with δ Scuti variables. δ Sct variables are short-periodic pulsating subgiants or main sequence stars. Their pulsations have periods of a few hours, and show luminosity variations of $\Delta m = 0.01^m \dots 0.9^m$. The δ Sct variables are located at the lower end of the Instability Strip.

Low-mass stars having evolved off the main sequence and have reached the horizontal branch can cross the Instability Strip and become short-periodic variable stars, RR Lyraes. They have typical periods of pulsation around $0.2 \text{ day} < P < 1 \text{ day}$ and show luminosity variations of $\Delta m = 0.2^m \dots 1.8^m$. The mean absolute magnitude $\approx +0.75^m$ in the V-band of RR Lyraes corresponds to around $40L_{\odot}$ (Layden et al., 1996). They belong to the metal-poor old population ($> 10 \text{ Gyr}$) of the Galaxy, i.e., are members of the Population II. RR Lyraes are important tracers of the chemical and dynamical properties of old stellar populations. Pietrukowicz et al. (2015) have discovered and analyzed around 30000 RR Lyrae stars in the Galactic bulge in the Optical Gravitational Lensing Experiment (OGLE) survey. Applying PLC relations and a correlation between the metallicity and luminosity (Smolec, 2005), they investigated the geometrical shape and metallicity distributions of the bulge. A similar investigation of the Magellanic System with over 45000 RR Lyrae stars was done by (Soszyński et al., 2016). Recently, Hernitschek et al. (2017) presented a comprehensive and precise description of the Sagittarius (Sgr) stellar stream's 3D geometry using a sample of $\sim 44,000$ RR Lyrae stars from the Pan-STARRS1 (PS1) 3π survey (Hernitschek et al., 2016). The resulting detailed geometric structure provides new constraints for dynamical stream models.

There are two types of Cepheid variables, which belong to different populations of stars: classical Cepheids and type II Cepheids. The type II Cepheids have periods between 1 and around 50 days (Wallerstein, 2002), and belong to the Population II, i.e., are typically metal-poor and old low-mass variables, whose luminosities lie below those of the classical Cepheids and above those of the RR Lyrae stars. Type II Cepheids with periods between 1 and 7 days are often referred to as BL Her stars. They are evolving from the horizontal branch toward the asymptotic giant branch (AGB) and appear in globular clusters and the Galactic disk. Type II Cepheids with periods between 4 and 20 days are the W Vir stars, which cross the instability strip during their blue-loop excursions from the AGB during helium-shell flashes. The brightest stars in the Population II Instability Strip are RV Tau stars, which are at the stage of leaving the AGB on the way to the white dwarf domain and having periods longer than 20 days. The OGLE survey discovered around 250 type II Cepheids in the Magellanic System (Soszyński et al., 2008, 2010b) and 357 in the Galactic Bulge (Soszyński et al., 2011).

The classical Cepheid variables have periods $1 \text{ day} < P < 100 \text{ days}$ and luminosities of $10^2 < L/L_{\odot} < 10^5$ (Turner et al., 2010). They are relatively young and massive Population I stars. In the HR-diagram they are located where the Instability strip crosses the super-giants branch. Effective temperatures of Cepheids lie between $\approx 5000 \text{ K}$ and 7000 K . A massive star with a mass in the range $M \sim 4 - 25 M_{\odot}$ (Turner, 1996) crosses the strip several times during its evolution. Above 8000 classical Cepheids were discovered in the Large Magellanic Cloud, Small Magellanic Cloud, towards the Galactic center, and in the Galactic disk (Pietrukowicz et al., 2013; Soszynski et al., 2008; Soszyński et al., 2010a, 2011) oscillating in the fundamental, first, or second overtone modes. Some classical Cepheids pulsate simultaneously in two or even three modes. In my investigation further I will primarily focus on modeling of classical Cepheid atmospheres oscillating in the fundamental mode.

The location of the high temperature – so-called blue – boundary of the Instability Strip can be physically understood as follows: a high effective temperature of a star leads to a very external location of the zone of partial ionization of hydrogen and helium. The low density and small mass fraction of the driving region renders the excitation of pulsations due to the $\kappa - \gamma$ mechanism inefficient, and beyond a certain effective temperature pulsations are not excited any longer.

The low temperature – red – boundary of the Instability Strip comes about by the following effect: a lower effective temperature tends to move the partially ionized regions where the pulsations are driven into deep, dense regions. The mass involved in the driving of pulsations becomes larger. However, convection also becomes more efficient at lower effective temperatures, because of opacity gradients in the driving regions are reduced by effects of convection. Qualitatively, it leads to a quenching of pulsations (Baker and Kippenhahn, 1965). For an accurate evaluation of the red boundary one has to take into account the coupling between convection and pulsation in the stellar envelope. Several attempts were made with non-local time-dependent theories of convection (Bono and Stellingwerf, 1994; Feuchtinger, 1998; Stellingwerf, 1982). The red and blue

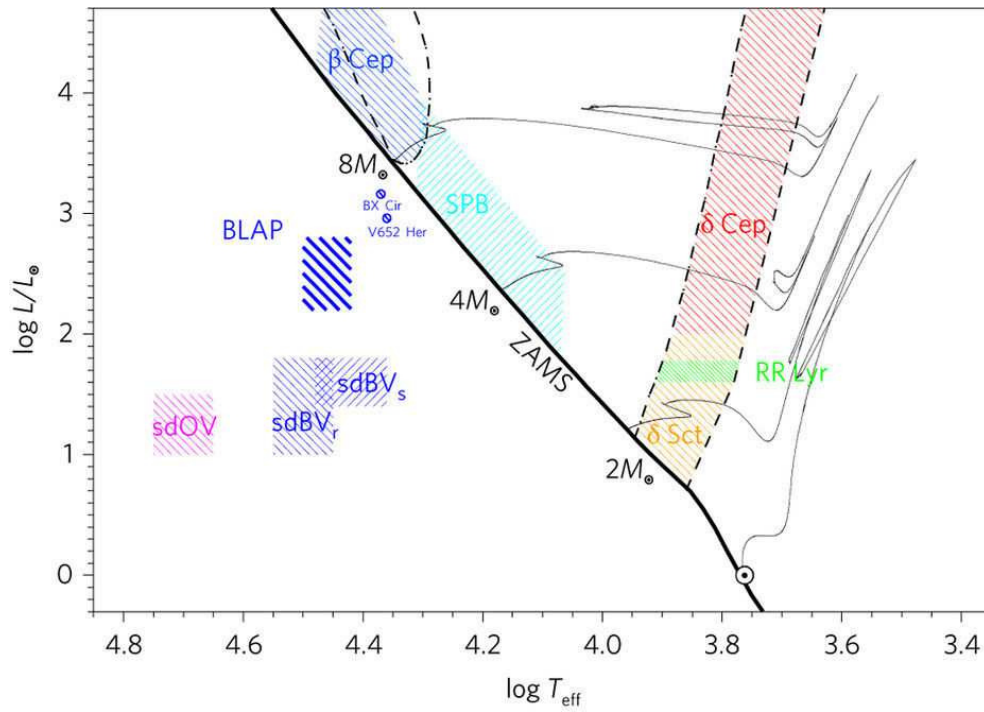


Figure 3: Various types of pulsating stars in H-R diagram from the paper of Pietrukowicz et al. (2017). The Instability Strip is located between the dashed dotted lines. Classical pulsating stars, RR Lyraes and classical Cepheids, are shown by green and red colors, respectively. The zero age main sequence (ZAMS) is shown by the solid black line, and evolutionary tracks for 1, 2, 4 and $8M_{\odot}$ by gray solid lines. Image credits: Pietrukowicz et al. (2017)

boundaries of the Instability Strip were theoretically derived by Bono et al. (1999a) with non-linear pulsating models for three different chemical compositions.

1.3.4 Why are Cepheids of particular interest?

Firstly, Cepheids are young evolving objects (< 100 Myr). Observing a Cepheid variable over long time intervals allows one to derive the change of the period and probe effects of stellar evolution. Analytically, one can derive an expression for the change of the period of pulsations combining Eqs. 20 and 21

$$\frac{d \ln P}{dt} = \frac{3}{4} \frac{d \ln L}{dt} - 3 \frac{d \ln T_{\text{eff}}}{dt}. \quad (23)$$

The typical evolution on the red giant branch or off the horizontal branch is dominated by changes in luminosity, the effective temperature changes rather little. One can see on evolutionary tracks for 4 and 8 solar mass stars in Fig. 3. Equation 23 shows that if the effective temperature decreases at constant luminosity the period becomes longer. According to Eq. 20 a longer period is related to a lower mean density, which is result of increase of the radius.

Turner et al. (2006) observed the rates of period change in over 200 Milky Way Cepheids and showed in general agreement with predictions from stellar evolution models. However, the observed sample displays features, which are inconsistent with some models from the literature. It indicates the absence of some important physical effects and factors in the models, and thus that the models need to be improved. Neilson et al. (2015) measured rates of period change for the classical Cepheids *l* Car and Polaris and comparing with stellar evolution models derived mass-loss rates. Besides the rather subtle feature of period changes, the observation of Cepheids constrains the location of the Instability Strip.

Bono et al. (2005) derived period-age (PA) and period-age-color (PAC) relations for fundamental and first-overtone classical Cepheids from homogeneous sets of evolutionary and pulsation models covering a broad range of stellar masses and chemical compositions. Anderson et al. (2016) has shown, that PA relations depend significantly on rotation, with rotation leading to older Cepheids. Using PA and PAC relations one can derive individual stellar ages with a precision of 10 – 20% in the Galaxy and in external Galaxies. The main advantage of this approach is its independence of distance.

For a long time there existed a Cepheid mass discrepancy problem (Christy, 1968; Stobie, 1969a,b,c) – the calculated evolutionary mass was higher than the one obtained from the pulsation theory by about 20% (Bono et al., 2006). Theoretically, according to Anderson et al. (2014) the mass discrepancy problem can be explained by a combination of increased luminosity due to rotation and luminosity differences between Cepheids at their second and third crossing of the Instability Strip. Practically, observation of Cepheids in eclipsing binary systems do contribute to the solution of the problem (Pilecki et al., 2016) and make additional tests of stellar evolution models possible.

In cosmological applications Cepheids are standard candles to measure Galactic and extragalactic distances with unprecedented precision Riess et al. (2016). Distance up to approximately 30 Mpc can be measured. Reddish (1956) predicted theoretically a dependence of the PL relation on the helium content. Recent theoretical studies of Bono et al. (1999a) showed a dependence of the zero point and the slope of the calculated PL relations on metallicity. Additionally, derived PLC relations for both visual and near-infrared photometric bands show the effect of metallicity decreases with increased wavelength. Romaniello et al. (2005, 2008) investigated the impact of the iron content on the period - luminosity relations in the V and K bands for Galactic and Magellanic Cepheids. Their results indicate that the Cepheid PL relation is not universal. As a consequence, systematic effects will affect the associated extragalactic distance scale. Most recent studies of Marconi et al. (2010) and Bono et al. (2010) combining both theory and observations show, that the slope of the PL relation becomes steeper when moving from optical to near-infrared (NIR) bands, and that the metallicity dependence of the slope decreases from the B- to the K band. Wielgorski et al. (2017) found a very small metallicity effect on the near-infrared absolute magnitudes of classical Cepheids, which can provide measurement of the Hubble constant with an accuracy of 1% combined with supernova Ia observations. One can calibrate the PL and PLC relations using precise GAIA measurements of parallaxes of the Galactic Cepheids.

The chemical composition of Cepheids can provide information on the chemo-dynamical evolution of galaxies. Abundances and abundance ratios of many chemical elements can be measured from Cepheid spectra to derive their distribution in different environments within the Galaxy and beyond. For instance, abundance gradients in the Galactic disk for 25 chemical elements (from carbon to gadolinium) have been derived by Andrievsky et al. (2002b); da Silva et al. (2016); Genovali et al. (2015); Lemasle et al. (2013). Because Cepheids are bright supergiants, they allow us to probe the inner disk (Andrievsky et al., 2016; Genovali et al., 2013; Martin et al., 2015) as well as the outermost regions (Andrievsky et al., 2004; Lemasle et al., 2008; Luck et al., 2011). Lemasle et al. (2017) spectroscopically studied the chemical composition of several Cepheids located in the same populous cluster, NGC 1866, in the Large Magellanic Cloud. They found a very spatially homogeneous chemical composition of NGC 1866. Using distances based on period-luminosity relations in the near- or mid-infrared, they investigated for the first time the metallicity distribution of the young population in the SMC in the depth direction. Preliminary results show no metallicity gradient along the SMC main body.

The standard method for determining Cepheid atmospheric parameters and abundances is based on one-dimensional plane-parallel hydrostatic stellar model atmospheres, allowing one to estimate the effective temperature, surface gravity, and microturbulent velocity, which change with pulsational phase, as well as the phase-independent abundances (see e.g. Andrievsky et al., 2005; Kovtyukh et al., 2005; Luck and Andrievsky, 2004; Luck et al., 2008). Physically, the pulsational period is of the same order as the dynamical timescale defined by the sound travel time across the star. The relaxation time for mechanical disturbances caused by pulsational waves in comparison with the pulsational period characterizes the deviation from hydrostatic conditions. For a Cepheid

model with a ten-day period, deviations from hydrostatic conditions are expected to be on the level of a few percent (Gautschy, 1987); this is also the case for thermal deviations. From this perspective one would expect that the standard approach should work rather satisfactorily.

1.4 Dynamical models

Dynamical non-linear stellar models of pulsating stars restricted to one spatial dimension (1D) have a long history, for instance see Bono and Stellingwerf (1994); Bono et al. (1999b); Christy (1962, 1964); Cox et al. (1966); Marconi et al. (2005); Smolec and Moskalik (2008); Stellingwerf (1982). In those works, the convective flux was modeled using a 1D time-dependent theory of convection and a characteristic scale length over which convection mixes mass, typically taken proportional to the pressure scale height. Additionally, the radiation flux was modeled in gray diffusion approximation neglecting the effects of frequency dependence and non-locality of the radiation field in the outermost, optically thin layers. Models were aimed to reproduce the light and radial velocity curves, and the location of the instability strip in the HR diagram. In order to do detailed spectroscopic studies and investigate effects of dynamics, convection, pulsations and shock propagation in atmospheres, one has to develop a numerical code, which takes into account the effects of the radiative transfer in optically thin regions.

Fleischer et al. (1992); Hoefner and Dorfi (1997); Hoefner et al. (1995, 1998) developed dynamical atmospheres models of long-periodic variable stars solving radiation-hydrodynamic equations. They derived the mass loss focusing on formation of circumstellar dust shells including formation, growth, and evaporation of amorphous carbon grains. They used a periodic disturbance at the inner boundary below the photosphere – a piston – to simulate a pulsation of the star.

Fokin (1991); Fokin and Gillet (1997); Fokin et al. (1996) developed 1D atmosphere models to perform spectral synthesis calculations to investigate shock propagation and turbulence in Cepheid and RR Lyrae atmospheres. The models considered spherically-symmetric self-excited oscillations of radiative stellar envelopes without magnetic fields and rotation assuming local thermodynamic equilibrium and gray radiative transfer. Gillet et al. (1998) and Fokin et al. (1999) showed that the turbulence amplification in the atmosphere of a radially pulsating star is not only due to the global compression of the atmosphere during the pulsation. Strong shock waves propagating from the deep atmosphere to the very low density layers also play a role in the variation of the degree of turbulence, especially when they become hypersonic. However, the energy transport in these models is provided solely by radiation, convection is not considered.

Recently, two-dimensional (2D) hydrodynamic simulations of Cepheid envelopes were performed by Mundprecht et al. (2013) and Mundprecht et al. (2015) including comparisons to convection prescriptions commonly applied in 1D modelling. Their simulations show that the strength of the convection zone varies significantly over the pulsation period and exhibits a phase shift

relative to the variations in radius. To successfully match this multi-dimensional result by a 1D static, or even time-dependent convection model appears challenging. The authors conclude that significant improvements are needed to make predictions based on 1D models more robust and to improve the reliability of conclusions on the convection-pulsation coupling drawn from them. Multi-dimensional simulations can provide guidelines for developing descriptions of convection thereafter applied in traditional 1D modelling. However, the calculation of a grid of multi-dimensional Cepheid atmosphere models is a sizable computational problem due to the presence of different spatial and temporal scales.

1.5 The structure of this dissertation

The thesis is structured as follow:

- In Chapter 2 I shall review the theory necessary for the construction of 1D time-dependent dynamical atmosphere models of pulsating stars, starting with the physical formulation of the problem, basic equations, theories of convection, boundary and initial conditions. I shall consider the numerical implementation of a time-dependent theory convection, investigation of the stability of the numerical scheme. Applications of the modeling for investigation spectroscopic properties of the classical Cepheid KQ Sco are presented in Sec. 2.8.
- In Chapter 3 I shall describe my published results of the next qualitative step in spectroscopic investigation of Cepheids. I check the adequacy of a two-dimensional envelope model of a Cepheid-like variable, where the non-local and time-dependent nature of convection is included from first principles, focusing on its spectroscopic properties. I evaluate the microturbulent velocity, line asymmetry, projection factor, and Doppler shifts. Additionally, I present a possible solution to the 80-year problem concerning the residual velocities of Galactic Cepheids.
- In Chapter 4 I shall present my published results of the validity of the quasi-static approximation for Cepheid variables focusing on the spectroscopic determination of the effective temperature T_{eff} , surface gravity $\log g$, microturbulent velocity ξ_t , and a generic metal abundance $\log A$.
- In Chapter 5 I shall summarize results of this thesis and describe some future plans.

2 ONE-DIMENSIONAL DYNAMICAL ATMOSPHERE MODELS

In this chapter I outline the basic physical ingredients for constructing the radiation-hydrodynamics models of pulsating stellar atmospheres with the LAGRANGIAN HYDRODYNAMICS (LHD) code, numerical aspects of LHD, and apply it for an investigation of the impact of pulsations on spectroscopic properties of Cepheids taking the classical Cepheid KQ Scorpii. LHD is a dynamical one-dimensional plane-parallel radiation-hydrodynamics code for calculation of stellar atmospheres. The theoretical basis of the code is discussed in Benz (1991). The code was written by Dr. Hans-Günter Ludwig including the convective energy transport, which is implemented in the framework of Mixing Length Theory (Böhm-Vitense, 1958) as described in Mihalas (1978), and widely used to calculate hydrostatic stellar atmosphere models (see e.g. Caffau and Ludwig, 2007; Caffau et al., 2009, 2011; Dobrovolskas et al., 2013; Kučinskas et al., 2013; Ludwig and Kučinskas, 2012; Ludwig et al., 1999; Tremblay et al., 2011).

In order to calculate pulsating stellar atmospheres, it is desirable to add further capabilities to the code. On the one hand, modifications concern putting pulsations into the atmosphere model. On the other hand, one has to implement a time-dependent non-linear theory of convection to bring calculated models closer to the widely used approach of Bono and Stellingwerf (1994) and Bono et al. (1999a,b). They extensively used the non-linear theory of convection in codes for modeling the radial velocity and light curves of pulsating stars. The advantage of this theory is it can describe convective overshoot and the interactions between pulsations and convection.

The initial goal for modeling pulsating stellar atmospheres and the reasons, which have led to model Cepheids instead of short-periodic variables, RR Lyraes, are presented in Section 2.1. The physical formulation of the problem and basic equations describing the dynamics of a pulsating stellar atmosphere I present in Section 2.2. In Section 2.3 I discuss theories of convection, Mixing Length Theory and the non-linear time-dependent convection theory of Stellingwerf, including the criterion for convective stability. The calculation of the radiation transport is described in Section 2.4. In order to complete the system of partial differential equations describing a pulsating stellar atmosphere, one has to add initial and boundary conditions. I discuss them in Section 2.5. The numerical scheme of the LHD code and implementation of the non-linear time-dependent theory of convection are presented in Sections 2.6 and 2.7, respectively. The application of the modified code for the calculation of the Cepheid KQ Sco and comparison of the spectral synthesis results to observed data are given in Section 2.8. Finally, I summarize the results in Section 2.9.

2.1 Some precursory trials and errors

The initial idea concerning the modeling of pulsating stellar atmospheres was to construct a model of a short-periodic pulsating star, RR Lyra. Preston (2009, 2011) and Gillet et al. (2013)

observed emission lines of helium, which are the result of the complex dynamics and shock wave propagation in the atmosphere. In order to derive the surface helium abundance in metal-poor Population II stars, one can perform the time-dependent spectral synthesis of the HeI $\lambda 5376\text{\AA}$ (D3), HeI $\lambda 5876\text{\AA}$, and HeII $\lambda 4685\text{\AA}$ lines taking the dynamical atmosphere model and compare it with observations. As a first approximation, it is reasonable to take a standard hydrostatic stellar atmosphere model, which is extended several pressure scale heights below the photosphere, covering a typical optical depth range of $\log \tau_R \approx -6 \dots 2$, and model pulsations by varying the dynamical or thermodynamical quantities on the bottom boundary. For example, one can change the energy flux or velocity.

In order to understand the pulsating properties of RR Lyraes, Dr. Marcella Marconi (private communication) calculated a nonlinear, time-dependent convective hydrodynamical model with $T_{\text{eff}} = 7000\text{ K}$, $\log g \approx 2.8$, and $[\text{Fe}/\text{H}] = -1$ dex having the period of pulsations around 0.6 days with a code (Bono and Stellingwerf, 1994; Bono et al., 1997a,b; Marconi et al., 2015) for the investigation of pulsational properties across the Instability Strip, and modeling of radial velocity and light curves.

This model allows one to determine the bottom boundary condition for the 1D LHD models. In order to get pulsations I experimented by varying the radiative flux, which was taken from the model of Marcella for a pure radiative region at a pressure of $p_{\text{gas}} = 7.5 \times 10^4 \text{ dyn/cm}^2$. This pressure defines the location of the bottom boundary of the 1D LHD model. The observed light curve of Marcella's model and variation of the radiative flux, which was taken as the bottom boundary condition, are shown in Fig. 4. Numerical test experiments showed excitation of oscillations in several modes with additional noise. As a consequence, the calculated 1D LHD model had unrealistic light and velocity curves showing additional spikes. Experiments with adding viscosity to damp oscillations in overtones and noise additionally suppressed propagating shock waves in the atmosphere, and, finally, did not yield satisfactory results. One has to emphasize, that RR Lyrae stars have strong dynamical effects in their atmospheres related with shock propagation and the high velocity amplitudes of the pulsations, which are of the order of $60\text{-}80 \text{ km s}^{-1}$. It makes the constructing of dynamical atmospheres of RR Lyraes computationally challenging. As a consequence, one should start from "simpler" atmosphere models of Cepheids, which have lower velocity amplitudes of $\approx 15 - 25 \text{ km s}^{-1}$ and do not exhibit strong shock waves compared to atmospheres of RR Lyraes.

One can use Cepheid models for the investigation of the velocity gradients and the generation of turbulence in the atmosphere, which impacts on spectroscopic properties, and make a prediction of the microturbulent velocity profile as a function of the pulsational phase. These additional constraints on the microturbulent velocity from pulsating stellar atmosphere models can be useful for the chemical analysis of Cepheids, which is based on hydrostatic stellar atmosphere models.

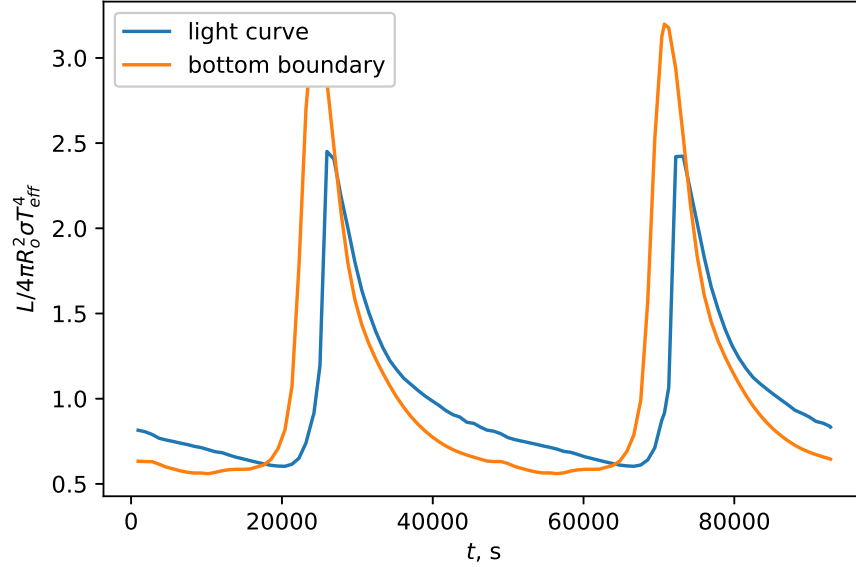


Figure 4: Variations of the radiative flux in a deep region at a pressure of $p_{\text{gas}} = 7.5 \times 10^4 \text{ dyn/cm}^2$ (orange), which was taken as the bottom boundary condition in numerical test experiments, and the luminosity at top boundary (blue) of the non-linear pulsating model of the RR Lyrae.

2.2 The physical formulation of the problem

Traditionally, hydrostatic stellar atmosphere models represent only the outer parts of a star. These models are extended toward low optical depths describing in detail the line forming region for subsequent spectral synthesis. However, in order to get stable pulsational properties in dynamical model atmospheres one has to extend the models toward deeper regions, where the temperature can exceed $\sim 10^6$ degrees, going from forced to free oscillations. One has to emphasize, it allows to change approach of setting pulsations by replacing the forced (see previous section) to free oscillations. The period of pulsations on a fundamental mode is around the sound-crossing time τ_{sc} across the envelope:

$$\tau_{\text{sc}} \approx 2 \int \frac{dz}{c_s(T, \rho)}, \quad (24)$$

where $c_s(T, \rho)$ is a sound speed, and z is a coordinate along the stellar radius. By changing the extension of the envelope toward deeper regions one can control the period of pulsations. However, in deep, dense regions of the stellar atmosphere the sound speed becomes significantly larger comparing with values in the photosphere, and the amplitude of oscillations decreases drastically.

I describe the one-dimensional plane-parallel envelope, in which the forces on the stellar material are due to gravity g and pressure P . The energy balance in the material is established by the energy flux f , which in general is transported by radiation f_{rad} and convection f_{conv} . I do not include

in the envelope model the effects of rotation, magnetic fields, non-LTE effects, or viscosity, with the exception of the artificial viscosity in regions undergoing strong compression by shock waves. These effects are assumed to be small compared to the influence of pulsations and convection on the structure of the atmosphere.

I want to calculate the spatial and temporal evolution of the radiative and convective fluxes, dynamic and thermodynamic quantities within the envelope for the given input parameters of the model, which are the effective temperature T_{eff} , surface gravitational acceleration $\log g$, and chemical composition [Fe/H]. In order to follow the evolution of these quantities, one has to solve the system of radiation hydrodynamics equations. Further, I shall use a Lagrangian description of the flow field with a mass column density m as independent coordinate, which is related to the geometrical coordinate by the transformation $dm = \rho dz$. Then, the equations of motion and energy are

$$\frac{Dv}{Dt} = -\frac{\partial p}{\partial m} + g, \quad (25)$$

$$\frac{De_i}{Dt} = -p \frac{\partial v}{\partial m} - \frac{\partial f}{\partial m}, \quad (26)$$

where $\frac{D}{Dt} = \frac{\partial}{\partial t} + v \frac{\partial}{\partial r}$ is the Lagrangian derivative and g is the gravitational acceleration. In addition, there is a kinematic relation

$$v = \frac{dz}{dt}, \quad (27)$$

where v is the velocity. The total pressure $p = p_{\text{gas}} + p_{\text{vis}} + p_{\text{turb}}$ has contributions of the gas p_{gas} , viscous p_{vis} , and turbulent p_{turb} pressures. The turbulent pressure is induced by convection, but in my calculations I set $p_{\text{turb}} = 0$, because its contribution is significantly smaller with respect to p_{gas} in the line formation regions. A viscous pressure is calculated according to the method of Von Neumann and Richtmyer (1950), which simplifies the procedures needed for stepwise numerical solution of the equations in problems involving shocks. The internal energy e_i for the fixed chemical composition at each instance in time is related with the gas pressure and density by the equation of state in forms of

$$T = T(e_i, \rho) \quad (28)$$

and

$$P_{\text{gas}} = P(e_i, \rho). \quad (29)$$

The equation of state in the LHD code is tabulated. The total flux at each depth point is a sum of the radiation and convective fluxes

$$f = f_{\text{rad}} + f_{\text{conv}}. \quad (30)$$

On the bottom boundary the total flux is transported by radiation and defined by the input effective temperature $f_{\text{bottom}} = \sigma T_{\text{eff}}^4$. The radiation flux at each instance in time is based on the solution of

the radiative transfer equation for the given thermal structure of the envelope. The convective flux is calculated according to the adopted theory of convection.

2.3 Convection in 1D

In stars sometimes a small fluctuation of thermodynamic or dynamic quantities can lead to a small displacement of a parcel of gas, an element of gas or fluid element, from its equilibrium position. If the fluid element was lifted, and it is lighter with respect to the new environment, then, it continues to move up producing macroscopic motions of a matter. These motions can have a strong influence on the stellar structure, such as mixing of the stellar material and transporting energy. In this case the original equilibrium state was unstable. If the lifted fluid element is heavier with respect to the new environment, it moves back to his initial position, and the original equilibrium state is stable. The criterion for the stability or instability of the material against convection was introduced by K. Schwarzschild in 1906. In the next section I outline the quantitative description of this criterion.

2.3.1 The criterion for convective stability

Let us consider a small element of gas in the atmosphere. Let us assume, it is initially hotter due to fluctuations than its surroundings. Because of its higher temperature, it has a lower density than the background and will tend to rise. Let us assume, it travels upward a distance Δr adiabatically, the motion of the element of gas is so slow, that it remains in the pressure equilibrium and exchanges no thermal energy with its surroundings. The background pressure drops as the element rises; hence it expands, and its density decreases by $(d\rho/dr)_{ad}\Delta r$. The density in the background decreases by $(d\rho/dr)_{bg}\Delta r$. At the new position, the density in the fluid element has changed by an amount

$$\Delta\rho = [(d\rho/dr)_{ad} - (d\rho/dr)_{bg}]\Delta r \quad (31)$$

relative to the background. A finite $\Delta\rho$ gives the buoyancy force $K = -g\Delta\rho$, where g is the absolute value of the acceleration of the gravity.

For the case with $\Delta\rho < 0$ the element is lighter and K is directed upwards, generating an unstable situation. The original perturbation is being increased.

If $\Delta\rho > 0$, the density in the fluid element at its new position is greater than the ambient density, so gravitational force acting on it will tend to draw it back toward its original position, the layer with the fluid element is stable. Thus, the atmosphere is stable against convection if

$$(d\rho/dr)_{ad} > (d\rho/dr)_{bg}. \quad (32)$$

I assume, that the material is an ideal gas, the background is in the radiative equilibrium, and the fluid element moves adiabatically. On the one hand, for the background in the radiative equilibrium the next expression is fulfilled for the gas element

$$\ln \rho_{\text{ad}} = \ln p_{\text{bg}} - \ln T_{\text{bg}} + C^*, \quad (33)$$

where C^* is constant. On the other hand, one can apply the adiabatic condition for the fluid element,

$$\ln \rho_{\text{ad}} = (1/\gamma) \ln p_{\text{ad}} + C, \quad (34)$$

where C^* is constant. So, the material is stable against convection with the pressure equilibrium between the fluid elements and the background when

$$\left(-\frac{d \ln T}{dr}\right)_{\text{bg}} < \frac{\gamma-1}{\gamma} \left(-\frac{d \ln p}{dr}\right)_{\text{ad}} \quad (35)$$

or

$$\nabla_{\text{bg}} \equiv \left(\frac{d \ln T}{d \ln p}\right)_{\text{bg}} < \frac{\gamma-1}{\gamma} = \left(\frac{d \ln T}{d \ln p}\right)_{\text{ad}} \equiv \nabla_{\text{ad}}. \quad (36)$$

A gradient $\nabla_{\text{rad}} = (d \ln T / d \ln p)_{\text{rad}}$ describes the temperature gradient for the case that the energy is transported by radiation (or conduction). In a layer that transports all energy by radiation $\nabla_{\text{bg}} = \nabla_{\text{rad}}$. The radiation layer with the homogeneous chemical composition is stable if

$$\nabla_{\text{rad}} < \nabla_{\text{ad}}. \quad (37)$$

This is Schwarzschild stability criterion, which describes the linear stability against convection. In the stellar atmosphere due to the ionization effects and radiation pressure the stellar material is not an ideal gas. In order to take into account these effects, one generalizes the adiabatic exponent γ introducing Γ , which is not equal to $\gamma = 5/3$, and putting $\nabla_{\text{ad}} = \left(\frac{d \ln T}{d \ln p}\right)_{\text{ad}} \equiv (\Gamma - 1)/\Gamma$. Generalizing the criterion given by Eq. 37 for a layer with ∇ , where energy at the same time can be transported by radiation and convection, one can get

$$\nabla < \nabla_{\text{ad}}. \quad (38)$$

This stability is linear, because the change of the density of the fluid element given by Eq. 31 is described only by linear terms in Δr . To be more strict one should work with the linearized Navier-Stokes equations. This would also allow to include effects of viscosity. The derived criterion here is normally used to determine if convection will or will not occur in a given layer of a star.

Since, I construct the dynamical atmosphere model for pulsating star, one has to characterize a time scale of growth of the convective instability. The buoyancy force of the fluid element is $f_b = -g\Delta\rho$. In order to include ionization effects and radiation, let us allow for the effective mean molecular weight μ be variable and write the change of density $d \ln \rho = d \ln p - d \ln T + d \ln \mu =$

$d \ln p - \delta d \ln T$, where $\delta \equiv 1 - (\partial \ln \mu / \partial \ln T)_p = -(\partial \ln \rho / \partial \ln T)_p$. Then in the pressure equilibrium ($\Delta p \equiv 0$), $\Delta \rho = -\delta \rho \Delta T / T$, the buoyancy force is

$$f_b = \frac{\rho g \delta}{T} \Delta T = \frac{\rho g \delta}{T} \left[\left(\frac{dT}{dr} \right)_{\text{el}} - \left(\frac{dT}{dr} \right) \right] \Delta r. \quad (39)$$

Introducing the pressure scale

$$H_p \equiv -\frac{dr}{d \ln p} = -p \frac{dr}{dp}, \quad (40)$$

which is $H_p = \frac{p}{\rho g}$ for the hydrostatic case, one rewrites Eq. 39 in a form

$$f_b = -\frac{g \delta}{H_p} (\nabla_{\text{el}} - \nabla) \Delta r. \quad (41)$$

The acceleration of the fluid element producing by the buoyancy force one can write in a form

$$\frac{\partial^2 (\Delta r)}{\partial t^2} = -\frac{g \delta}{H_p} (\nabla_{\text{el}} - \nabla) \Delta r. \quad (42)$$

Let us assume for this derivation, that the fluid element moves adiabatically $\nabla_{\text{el}} = \nabla_{\text{ad}}$ in the convectively stable atmosphere, $\nabla_{\text{ad}} > \nabla$. So, Equation 42 describes oscillations of a fluid element around the equilibrium position with a characteristic angular frequency of

$$\omega_{\text{BV}}^2 = \frac{g \delta}{H_p} (\nabla_{\text{ad}} - \nabla), \quad (43)$$

which is the so-called Brunt-Väisälä frequency. If the layer is convectively unstable, $\nabla_{\text{ad}} < \nabla$, then the time dependance of the displacement grows in the exponential regime $\Delta r \sim e^{t/\tau_{\text{ci}}}$, where the time scale of growth of the convective instability is given by

$$\tau_{\text{ci}} = 2\pi / \omega_{\text{BV}} = 2\pi \sqrt{H_p / g \delta |\nabla_{\text{ad}} - \nabla|}. \quad (44)$$

The derivation of this time scale was based on an assumption about the adiabatic behavior of the fluid element. Additional radiative losses of the fluid element lead in average to a smaller difference in temperature gradients between the element and background, $|\nabla_{\text{el}} - \nabla| < |\nabla_{\text{ad}} - \nabla|$. As a consequence, the time scale of growth of the convective instability becomes longer.

2.3.2 The mixing length theory

The energy flux, which can be carried by convection, one can compute using Mixing Length Theory (Böhm-Vitense, 1958) (MLT). It describes convection as a local phenomenon using the basis of gas properties at the place of interest. In the mixing length theory all fluid elements have the same shape, mass, velocity, and lifetime $\tau_{\text{conv}} \gg l_m / c_s$, where c_s is sound speed and l_m is the mixing length, the distance traveled up or down by a parcel of gas before it mixes into the

surrounding gas, losing its identity. Traditionally, the mixing length l_m is taken proportional to the pressure scale H_p :

$$l_m \equiv \alpha H_p \quad (45)$$

The proportionality coefficient α is a free parameter in this theory.

The convective fluid element during the displacement Δr with the mean velocity v_{conv} , which is the convective velocity, produces the convective energy flux

$$f_{\text{conv}} = \rho C_p v_{\text{conv}} \Delta T = \rho C_p v_{\text{conv}} \left[\left(\frac{dT}{dr} \right)_{\text{el}} - \left(\frac{dT}{dr} \right) \right] \Delta r, \quad (46)$$

where C_p is the heat capacity with constant pressure.

The buoyancy force f_b and the convective energy flux are linear on the displacement Δr . Integrating over a total displacement Δr and averaging the result over all convective elements by setting $\Delta r = \frac{l_m}{2}$, the average work done on all elements passing a given point is

$$\langle w \rangle = \int_0^{\Delta} f_b(\Delta r) d(\Delta r) = \frac{1}{8} \frac{\rho g \delta}{T} \left[\left(\frac{dT}{dr} \right)_{\text{el}} - \left(\frac{dT}{dr} \right) \right] l_m^2 = f_1 \frac{\rho g \delta \beta l_m^2}{T}, \quad (47)$$

where f_1 is commonly assumed to be $\frac{1}{8}$, and β is the difference of temperature gradients within the fluid element and surrounding medium. One can transform β taking into account pressure scale given by Eq. 40 and the hydrostatic condition

$$\beta \equiv \left[\left(\frac{dT}{dr} \right)_{\text{el}} - \left(\frac{dT}{dr} \right) \right] = \frac{\rho T g}{p} (\nabla - \nabla_{\text{el}}) = \frac{T}{H_p} (\nabla - \nabla_{\text{el}}). \quad (48)$$

If half of this work is converted to kinetic energy, i.e., $\frac{1}{2} \langle w \rangle \approx \frac{1}{2} \rho v_{\text{conv}}^2$, then one can get an estimation of the convective velocity

$$v_{\text{conv}}^2 = f_1 \frac{g \delta \beta l_m^2}{T} = f_1 \frac{g \delta l_m^2}{H_p} (\nabla - \nabla_{\text{el}}). \quad (49)$$

Combining Eq. 46 and 48 and taking the displacement $\Delta r = \frac{l_m}{2}$ one can get an expression for the convective energy flux

$$f_{\text{conv}} = f_2 \frac{\rho v_{\text{conv}} C_p T l_m}{H_p} (\nabla - \nabla_{\text{el}}), \quad (50)$$

where $f_2 = 1/2$. However, in order to derive the convective velocities and fluxes with Eq. 49 and 50 one has to know the difference between the background gradient ∇ and the gradient of convective element ∇_{el} . Convective fluid elements exchange heat with surrounding material. The temperature difference δT between the fluid element and surrounding material produce radiative losses of the convective fluid elements, and, as a result, the gradient ∇_{el} differs from the adiabatic gradient ∇_{ad} .

Thus, one can characterize the efficiency of the radiative losses during the lifetime of a convective

element as

$$\Gamma = \frac{\text{surplus energy over lifetime}}{\text{radiative losses over lifetime}}. \quad (51)$$

The surplus energy in a fluid element is proportional to $(\nabla - \nabla_{\text{el}})$. This energy for the adiabatic motion is proportional to $(\nabla - \nabla_{\text{a}})$. So, the radiative losses is the differens between this gradient differences, $(\nabla - \nabla_{\text{ad}}) - (\nabla - \nabla_{\text{el}}) = \nabla_{\text{el}} - \nabla_{\text{ad}}$ and the efficiency of the radiative losses Γ

$$\Gamma = \frac{\nabla - \nabla_{\text{el}}}{\nabla_{\text{el}} - \nabla_{\text{ad}}}. \quad (52)$$

The exceeded heat energy of a convective element with a volume of V with respect to the surrounding medium is $\rho C_p V \delta T$. The radiative losses are different for the optically thin and optically thick convective elements. The rate of the radiative losses of the convective element in the optically thin regime is $4\pi\kappa_{\text{R}} \frac{\Delta B}{\Delta T} \Delta T$ at time scale of $l_{\text{m}} / \nu_{\text{conv}}$, where $\frac{\Delta B}{\Delta T} = 4\sigma T^3 / \pi$. Assuming the mean temperature difference of $\Delta T = \delta T / 2$ during losses, one can get

$$\Gamma_{\text{thin}} = \frac{\rho C_p \nu_{\text{conv}}}{8\sigma T^3 \tau_{\text{el}}}, \quad (53)$$

where $\tau_{\text{el}} \ll 1$ is the optical depth of the convective element with the typical size of l and $\tau_{\text{el}} = \kappa_{\text{R}} l$. For the optically thick limit $\tau_{\text{el}} \gg 1$ one can apply the diffusion approximation $-\frac{dT}{dr} \approx \frac{\delta T}{l}$. Adopting the surface area of the convective element as A and assuming a spherical shape of the convective elements $(V/A) = l/3$ one can get

$$\Gamma_{\text{thick}} = \frac{1}{16} \tau_{\text{el}} \frac{\rho C_p \nu_{\text{conv}}}{\sigma T^3}. \quad (54)$$

The assumption about shapes of convective elements is an additional source of uncertainties of the theory. Generalizing Eq. 53 and 54 one can get

$$\Gamma = \frac{\rho C_p \nu_{\text{conv}} \tau_{\text{el}}}{f_3 \sigma T^3} \left(1 + \frac{f_4}{\tau_{\text{el}}^2} \right), \quad (55)$$

where $f_3 = 16$ and $f_4 = 2$ are constants. Finally, in order to derive the convective fluxes and velocities with Eq. 49 and 50 one has to use additional conditions given Eq. 52 and 55.

Mixing Length Theory is applicable for non-variable stars. However, in a context of pulsating stars one has to include the time dependance of the convective fluxes and velocities. Zero order approximation is considering the pulsating atmosphere as a set of hydrostatic stages and calculation of the convective fluxes and velocities according to Eq. 49 and 50, respectively.

However, MLT does not contain convective overshoot. The momentum of a convective element can provide further motion beyond the convectively unstable region. Additionally, one has to include the interaction between pulsations and convection. Time-dependent non-linear theories (Bono and Stellingwerf, 1994; Kuhfuss, 1986; Stellingwerf, 1982) of convection take into account these effects.

2.3.3 Stellingwerf's theory of convection

One of the common time-dependent non-linear theories of convection, which is applicable for the analysis of pulsating stars is presented in papers of Bono and Stellingwerf (1994); Bono et al. (1999b); Marconi et al. (2005); Smolec and Moskalik (2008); Stellingwerf (1982). According to the Stellingwerf theory the phenomenon of convection is modeled as the advection-diffusion process. In a context of this theory the MLT solution is a non-linear, asymptotic energy of the convective motions for thick convection zones with zero velocity field. Stellingwerf (1982) describes temporal and spatial evolutions of the twice convective kinetic energy $\omega = 2E_t = v_{\text{conv}}^2$ of the mass unit in 1D case by the next equation:

$$\frac{D\omega}{Dt} = \frac{\partial}{\partial z} \left(\omega^{1/2} l \frac{\partial \omega}{\partial z} \right) + \frac{\omega^{1/2}}{l} (\omega_0 - \omega) - 2\omega \frac{\partial v}{\partial z}, \quad (56)$$

where l is the diffusion scale length of the Stellingwerf theory, ω_0 is a time-independent solution of the equation for thick convection zones, for which boundary effects produced by the diffusion can be neglected, with zero velocity field. The change in convective energy is composed of a diffuse component (first term) representing convective overshoot, a "phase-lag" term (second term) containing the "driver", ω_0 , and a term representing the interaction of convection and the velocity field v (third term).

The "driver" ω_0 is also a time independent solution of Eq. (56) for thick convection zones with zero velocity:

$$\omega_0 = -2Ql\nabla P \frac{\langle v' T' \rangle}{\sqrt{\omega}}, \quad (57)$$

where $Q = \left(\frac{\partial(l/\rho)}{\partial T} \right)_p$ is a thermodynamic derivative, and $\langle v' T' \rangle$ is a correlation between temperature and velocity fluctuations. The driver is basically given by the MLT. However, a stationary solution of the Stellingwerf equation does not coincide with the MLT due to the presence of the diffuse component. The correlation is related with the convective energy flux

$$f_{\text{conv}} = \rho C_p \langle v' T' \rangle. \quad (58)$$

To better define the structure of the boundaries between the convective and radiative regions and describe the overshooting regions taking into account the convective flux inversion according to Shaviv and Salpeter (1973)

$$\langle v' T' \rangle = \text{sign}(\beta) \omega \sqrt{\left| \frac{2l_m \beta}{\alpha P Q} \right|}, \quad (59)$$

where β is defined by Eq. 48. Concerning the diffusion length, it has been assumed that the overshooting region cannot be more extended than the local pressure scale height, so that $l \approx l_m/10$ has been assumed (Bono and Stellingwerf, 1994). The mixing length l_m is proportional to the pressure scale $l_m = \alpha H_p$, where the parameter $\alpha = 0.375$. It is the analog of the alpha

coefficient set equal to 1.5 in the MLT (Eq. 45).

A solution of Eq. 56 starting with initial MLT values gives spatial and temporal evolutions of the twice convective kinetic energy $\bar{\omega}$, which one can transform into the convective velocity $v_{\text{conv}} = \sqrt{\bar{\omega}}$. The convective flux is calculated according to Eq. 58. At the top and bottom boundaries I assume zero convective fluxes and velocities.

2.4 Radiative transfer

Historically, in one-dimensional non-linear stellar models of pulsating stars ((Bono and Stellingwerf, 1994; Bono et al., 1999b; Christy, 1962, 1964; Cox et al., 1966; Marconi et al., 2005; Stellingwerf, 1982) the radiative flux was calculated in the diffusion approximation described in Section 1.2. The diffusion approximation is also were used in the optically thin regions neglecting by non-local properties of the radiation field. However, one has to keep in mind, that these models are aimed at reproducing of pulsation properties, light and radial velocity curves. The effects in optically thin layers have a negligible influence on pulsating properties of those models.

In my work, I extend the optically thin layers of modeled pulsating stellar atmosphere up to $\log \tau_{\text{R}} \approx -6$ in order to perform subsequent spectral synthesis of interested lines. In this approach, one has to take into account the non-local properties of the radiation field and perform solution of the radiative transfer equation.

2.4.1 Calculation of the radiative flux

In order to calculate the radiative flux f_{rad} at each depth point one has to know the angular distribution of the specific intensity $I_{\nu\mu}$, where ν is a frequency, and $\mu = \cos\Theta$ defines direction. The specific intensity is a result of solution of the radiative transfer equation

$$\mu \frac{dI_{\nu\mu}}{d\tau_{\nu}} = I_{\nu\mu} - S_{\nu}, \quad (60)$$

where $d\tau_{\nu} = -\kappa_{\nu} dz$ is the optical depth, $S_{\nu\mu} = B_{\nu}$ – the source function taking in the LTE approximation is symmetric relative to μ . The frequency integrated source function for the LTE case is

$$S = \int B_{\nu} d\nu = \frac{\sigma}{\pi} T^4, \quad (61)$$

So, after getting solutions of the Eq. 60 for each frequency and direction one can calculate the radiation flux

$$f_{\text{rad}} = 2\pi \int_0^{\infty} d\nu \int_{-1}^1 d\mu I_{\nu\mu} \mu. \quad (62)$$

On can rewrite the Eq. 60 considering separately the intensities I_{ν}^{+} and I_{ν}^{-} along directions μ and

$-\mu$, respectively

$$\pm \mu \frac{dI_{\nu\mu}^{\pm}}{d\tau_{\nu}} = S_{\nu} - I_{\nu\mu}^{\pm}, \quad (63)$$

where $0 \leq \mu \leq 1$. Introducing two variables $u = (I_{\nu}^{+} + I_{\nu}^{-})/2$ and $v = (I_{\nu}^{+} - I_{\nu}^{-})/2$, one can transform the Eq. 63

$$\mu^2 \frac{d^2 v}{d\tau_{\nu}^2} = v - \mu \frac{dS_{\nu}}{d\tau}. \quad (64)$$

One can get similar second-order differential equation for u . However, from numerical point of view Eq. 64 for v is better adapted to energy conservation. In order to solve the second-order linear differential equation one needs two additional constrains, boundary conditions. Physically, the atmosphere model does not have external sources of radiation

$$I_{\nu}^{-}(\tau = 0) = 0. \quad (65)$$

At the bottom boundary $\tau = \tau_{\max} \gg 1$ the diffusion approximation is valid for the radiation field:

$$v_{\nu} = \mu \frac{dB_{\nu}(\tau = \tau_{\max})}{d\tau_{\nu}}, \quad (66)$$

where $B_{\nu}(\tau = \tau_{\max})$ is the Planck function at the bottom optical depth point. Numerical solution of the Eq. 64 – 66 is performing for the discrete set of directions μ and frequency ν taking the condition for the radiative flux given by Eq. 62 for each depth, which has to be consistent with the convective and total fluxes. Numerical solution of the radiative transfer equation is computationally expensive according to Eq. 64. In the LHD code the equation is solving adopting the Feautrier scheme (Feautrier, 1964). In my calculations I shall use assumption about grey radiative transfer, i.e. opacity is independent on frequency. The reason of it is the computationally expensive frequency-dependent radiative transfer and absence of frequency dependent opacity tables for high temperatures and densities, which are in deep regions of constructed models. In details I shall discuss the grey radiative transfer in Section 3.1.2.

2.5 Boundary and initial conditions

Equations 25-30, 49-56, and 60 describe the dynamics of a pulsating stellar atmosphere, where energy is transported by convection and radiation. They have to be supplemented by the boundary and initial conditions.

2.5.1 Initial conditions

One can put various initial thermal structures of the model, which can be far from the thermal and hydrostatic equilibrium. However, I start with the thermal structure of the model in the hydrostatic and thermal equilibrium, which can be calculated adopting $\frac{D}{Dt} = 0$ for the equations.

The advantage of this approach is that disturbances of the thermal structure of the model, which produce an additional high frequency noise in pulsations with low damping, do not appear in further dynamical calculations ($\frac{D}{Dt} \neq 0$). One can set different perturbations of the initial model in order to accelerate reaching of the limiting cycle.

2.5.2 Excitation of pulsations

Depending on the application one can model the pulsation in a variety of ways. In order to get a thorough investigation of the edges of the instability strip, mechanisms of oscillations, and analyses of light and radial velocity curves one needs to obtain the natural excitation of pulsations in non-linear pulsating models largely omitting the atmospheric dynamics.

I construct pulsating stellar atmosphere models, which have reached a limit cycle. I am more focused on spectroscopic properties and being less interested on the mechanism of excitation of pulsations. For spectroscopic studies one can apply two different approaches in order to get pulsations:

1. The pulsation is introduced by perturbing the atmosphere model with a "piston", has a certain period and amplitude. These parameters are specific for each Cepheid. For example, velocity of the piston at the inner boundary varies harmonically

$$V_{\text{bot}}(t) = V_0 \sin(2\pi t/P). \quad (67)$$

There are additional input parameters: the velocity amplitude V_0 , which simulates the interior pulsation of the star, and the pulsation period P , which identifies "the period of pulsations". Fleischer et al. (1992) and Hoefner et al. (1998) applied the piston model as a reasonable first-order approximation to model the stellar pulsation of atmospheres of long periodic pulsating stars. The piston is located a few scale heights below the photosphere. This chosen location serves a practical purpose since it avoids the extension of the model towards deep hot regions, which requires long computational time due to the long thermal relaxation time scale in order to get a hydrostatically and thermal relaxed model, i.e. the system is in hydrostatic and radiative equilibrium.

Light curves of test calculations of the short-periodic variable with the parameters of $T_{\text{eff}} = 6000$ K, $\log g = 2.0$, and $[\text{Fe}/\text{H}] = 0$ and including the piston model is shown in Fig. 5. In order to obtain the relative variation of the luminosity $\delta L/L$ of the model as in a case of observations of real pulsating stars, one has to impose large amplitudes of the piston.

Parameters of the piston have a strong influence on the global atmospheric structure and its dynamics. For the piston model, the atmosphere shows the linear response, and as a result, the light curve is symmetric, which contradicts the asymmetric shape as seen as in observations. One "injects" a fraction of kinetic energy energy flux $E_{\text{kin}} \sim \rho_{\text{bot}} V_0^2$ on the

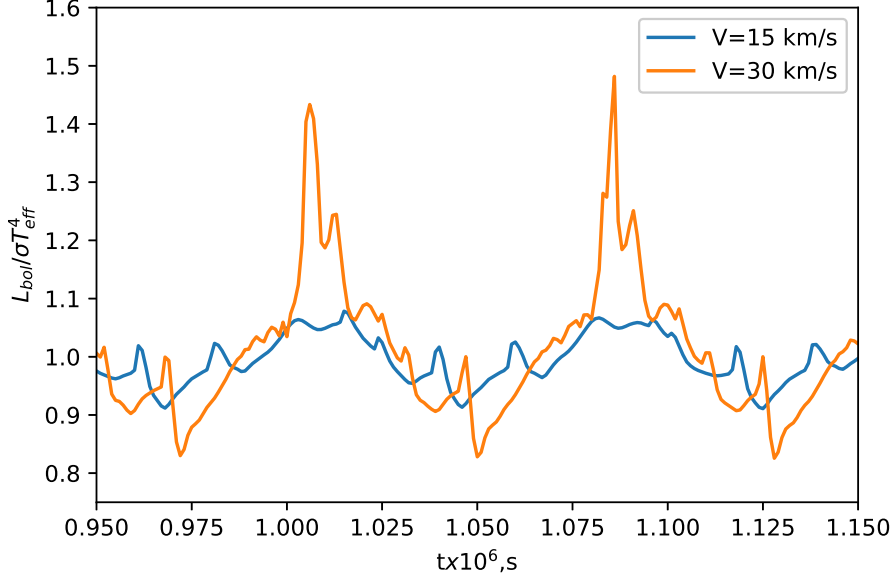


Figure 5: Test bolometric light curves of the piston model for two different velocity amplitudes $V_0 = 15$ and 30 km s^{-1} .

bottom, such that the perturbation waves transport this energy upward. According to the energy conservation law and assuming the amplitude of perturbations to be 1 km s^{-1} and the relative density difference between the bottom and optically thin regions to be on a level of $\frac{\rho_{\text{top}}}{\rho_{\text{bot}}} \sim 10^{-4}$, one would expect an amplitude of in the order of $V_{\text{top}} \sim 100 \text{ km s}^{-1}$, which is quite large even for a short-periodic class of pulsating stars, such as RR Lyraes. A more critical effect proves to be a problem is excitation of oscillations in a fundamental mode and its harmonics, as well as the overtones of the piston including additional noise. As a result all of this, the light curve contains spikes. The real pulsating stars exhibits dominant oscillations on fundamental modes or a few subsequent overtones, and they have smooth radial velocity and light curves (Kovacs et al., 1990). The normalized amplitude Fourier spectrum of the radial velocity of the photospheric layer with $\tau_R = 1.0$ is shown in Fig. 6. In this figure, perturbations of the velocity field on the bottom have an amplitude of 15 km s^{-1} and a pulsational period of 0.925 days, which is equal to the fundamental period of the initial equilibrium model. As one can see on the amplitude Fourier spectrum, the piston with the frequency of $\nu_{\text{piston}} \approx 1.3 \times 10^{-5} \text{ Hz}$ shows wider FWHM as compared to those of higher frequency components. From a physical point of view this means, that the atmosphere model itself has a higher damping factor for oscillations for the piston frequency. The piston perturbs the thermal structure of the modeled atmosphere, which in turn causes the fundamental frequency to differ from the initial equilibrium value. The additional excited oscillations strongly distort the radial velocity curve. To produce qualitatively realistic radial

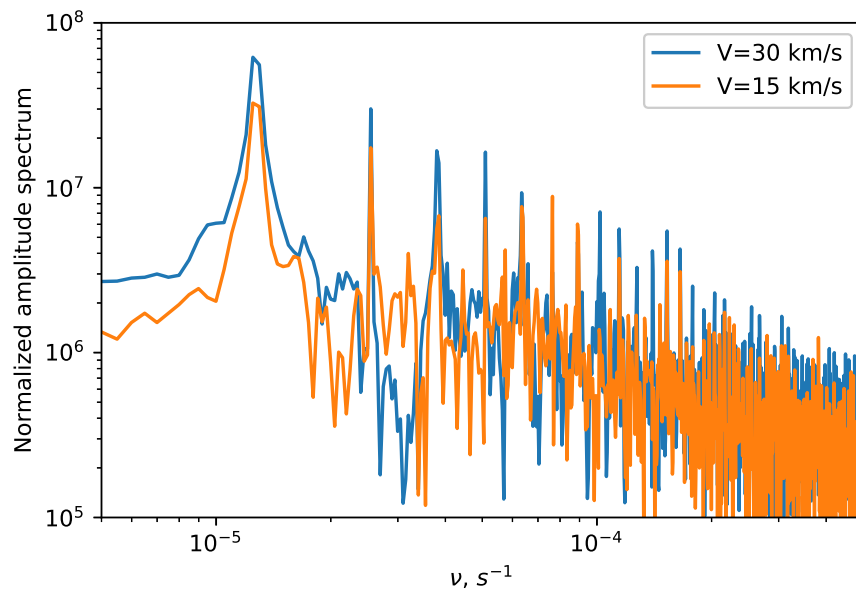


Figure 6: Normalized amplitude spectrum of the radial velocity of the photospheric layer at optical depth $\tau_R = 1.0$. Pulsations are excited at the bottom with in amplitudes of 15 km s^{-1} and 30 km s^{-1} with the fundamental period of 0.925 days. The spectrum shows excitation of oscillations at different frequencies as well as the fundamental frequency and overtones, which have a significant amplitude with respect to the piston amplitude.

velocity and light curves, one has to develop alternative methods of modeling of pulsations.

2. One can put the initial perturbation at $t = 0$ in a form of the depth dependent velocity profile in the fundamental frequency, which is based on the solution of the wave equation. As one can see, according to this approach pulsations are considered as free oscillation.

One can consider small adiabatic perturbations under the hydrostatic atmosphere,

$$\frac{\delta p}{p_o} = \gamma \frac{\delta \rho}{\rho_o}, \quad (68)$$

$$\frac{\partial p_o}{\partial z} = -g\rho_o, \quad (69)$$

where δP and $\delta \rho$ are the Lagrangian perturbations of the pressure and density, i.e. the perturbations suffered by a fluid element as it moves back and forth, p_o and ρ_o are the unperturbed pressure and density, and γ is the adiabatic exponent related with the sound speed,

$$c_s^2 = \gamma \frac{p_o}{\rho_o}. \quad (70)$$

For the displacement ξ of a fluid element from its equilibrium position, the Lagrangian perturbations denoted by δ are related with the Eulerian perturbations, the perturbations at fixed point, denoted by index "1"

$$\delta \rho = \rho_1 + \xi \frac{\partial \rho_o}{\partial z}, \quad (71)$$

$$\delta p = p_1 + \xi \frac{\partial p_o}{\partial z}, \quad (72)$$

The displacement related with the velocity of the oscillating fluid element

$$v_1 = \frac{\partial \xi}{\partial t}. \quad (73)$$

The linearized continuity and momentum equations in the Eulerian specification of the flow field one can write in the following form:

$$\rho_1 - \frac{\partial}{\partial x}(\rho_o \xi) = 0, \quad (74)$$

$$\rho_o \frac{\partial v_1}{\partial t} = -\frac{\partial p_1}{\partial z} - g\rho_1. \quad (75)$$

Taking into account Eq. 68-73 one can derive from Eq. 74 and 75 the wave equation for the displacement ξ :

$$\frac{\partial^2 \xi(z, t)}{\partial t^2} = c_s^2(z, t) \frac{\partial^2 \xi(z, t)}{\partial z^2} + \left[c_s^2(z, t) \frac{\partial \ln \gamma(z, t)}{\partial z} - \gamma(z, t) g \right] \frac{\partial \xi(z, t)}{\partial z}. \quad (76)$$

The sound speed and the adiabatic exponent are functions of the geometrical depth, and

they are given by the initial hydrostatic atmosphere model. One can expand the solution of Eq. 76 as Fourier series

$$\xi = \sum_n \xi_n = \sum_n A_n e^{i\omega_n t} e^{ik_n z}, \quad (77)$$

where A_n , ω_n , and k_n are the amplitude, angular frequency, and wave number of the Fourier component ξ_n , respectively. Equation 76 is a second order differential equation. Thus, in order to find a solution, which is the displacement $\xi_n(z, t)$ as well as the eigenfrequency ω_n , one has to supplement boundary conditions. I consider the bottom boundary as a node:

$$\xi_{\text{bot}}(t) = 0. \quad (78)$$

For a top boundary I put zero Lagrangian pressure perturbations

$$\delta P_{\text{top}}(t) = 0, \quad (79)$$

which one can transform into

$$P_{1,\text{top}} = -\xi g \rho_{0,\text{top}}. \quad (80)$$

The goal to calculate the fundamental frequency with a condition of having a node at the bottom boundary. In order to find the frequency one can numerically solve Eq. 76 for given boundary conditions. Then, according to Eq. 77 one can derive the profile of initial displacements and transform it into an initial velocity perturbation profile. The amplitude of the velocity perturbation at the top of the model is an input parameter. In order to get a typical amplitude of oscillation for Cepheids one has to take a velocity amplitude of $\approx 20-40 \text{ km s}^{-1}$. Since these perturbations are not small, they produce some disturbances, which have a tendency to be damped during the first ~ 30 pulsation periods. The price to pay for working with free oscillations is that the model has to get deeper according to Eq. 24, if one wants to get longer periods. The temporal evolution of the radial velocity of the layer with $\tau_r = 1$ and bolometric light curve of a Cepheid model are showed in Fig. 7. The model has the effective temperature of $T_{\text{eff}} = 5000 \text{ K}$, the surface gravity acceleration of $\log g = 1.0$, and solar chemical composition. Pulsations excited by an initial perturbation of the velocity field at the fundamental frequency with an amplitude of 35 km s^{-1} . A normalized amplitude spectrum of the radial velocity of the photospheric layer with $\tau_R = 1.0$ is shown in Fig. 8 after the limit cycle has been reached. The method yields pulsations in the fundamental frequency. The power of overtones decreases exponentially with increase of frequencies. The amplitude spectrum does not show noise components, and the model has smooth radial velocity and light curves.

The period of pulsations of stellar atmosphere models excited by an initial depth dependent velocity profile is defined by the sound-crossing time τ_{sc} across the envelope. So, one has to extend the model toward deeper hotter regions. From technical point of view, it requires long computational time to get the initial relaxed model due to the long Kelvin-Helmholtz

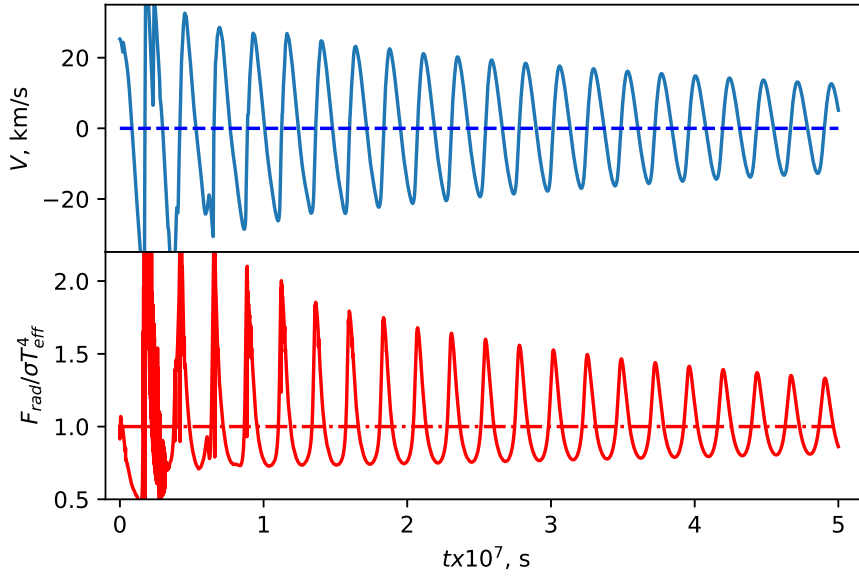


Figure 7: The initial temporal evolution of the radial velocity of the layer with $\tau_r = 1$ (top panel) and bolometric light curve for pulsations excited by an initial perturbation of the velocity field on a fundamental frequency (bottom panel).

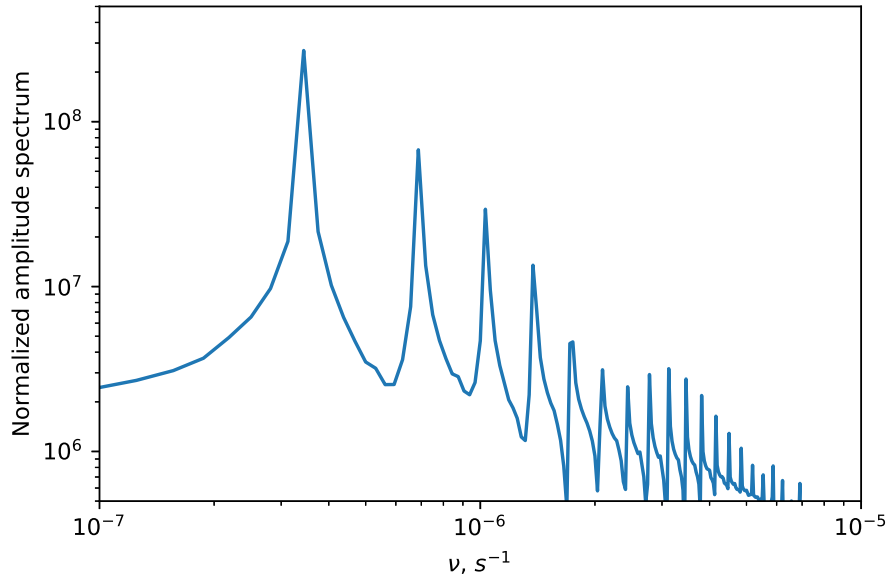


Figure 8: The normalized amplitude spectrum of the radial velocity of the photospheric layer with $\tau_R = 1.0$. Pulsations are excited by perturbations of the velocity field based on a solution of the wave equation (Eq. 76) with the amplitude on the top $V_{\text{top}}(t = 0) = 20 \text{ km s}^{-1}$.

time scale.

In further presented work I shall use the method (2) to excite pulsations of dynamical atmosphere models.

2.5.3 Boundary conditions

Boundary conditions for the system of radiation hydrodynamics equations can be split into two groups:

- Radiation: the bottom boundary is pure radiative, $f_{\text{bottom}} = \sigma T_{\text{eff}}^4$, where the flux is defined by one of the input parameters, effective temperature. With this setup, the convective energy flux is zero on the bottom and on the top. At the top, radiation can leave unimpeded and additionally, there is no irradiation from above.
- Hydrodynamics: since I produce the initial perturbation on a fundamental mode, the bottom boundary is a node with zero velocity, $v_{\text{bottom}}(t) = 0$. Formulation of the top boundary condition, which is transparent for running acoustic waves, is not trivial from the mathematical point of view. According to Landau and Lifshitz (1959), for the incident acoustic wave, which falls along the normal to a boundary between two mass elements j and $j + 1$ with densities, ρ_j , and ρ_{j+1} , and sound speeds, c_j and c_{j+1} , the reflection index is

$$R = \left(\frac{\rho_{j+1}c_{j+1} - \rho_jc_j}{\rho_{j+1}c_{j+1} + \rho_jc_j} \right)^2 \quad (81)$$

In order to avoid reflection, one needs to gradually change thermodynamic quantities within two mass elements, $\rho_{j+1}c_{j+1} \approx \rho_jc_j$. Therefore I add an additional ghost mass element in order to provide the pressure gradient based on the hydrostatic equation

$$p_{\text{ghost}}(t) = p_N(t) - \Delta m_N g \quad (82)$$

Then, one can take the estimated pressure of the ghost boundary in the momentum equation (Eq. 25),

$$v_{\text{top}}(t + \Delta t) = v_n(t) - \Delta t[(p_{\text{ghost}}(t) - p(t))/\Delta m_N + g] \quad (83)$$

I shall use the top boundary given by Eq. 83. The prescribed pressure p_{ghost} provides a very stable reference point, such that the point is not being catapulted during pulsations.

2.6 Numerical scheme of the LHD code.

In order to calculate a dynamical stellar atmosphere, one has to choose main three input parameters: the effective temperature T_{eff} , surface gravity $\log g$, and metallicity $[\text{Fe}/\text{H}]$. The first

parameter defines the total energy flux passing the bottom boundary, which is constant and physically defined by energy production rate in close to the stellar core regions. The surface gravity acceleration $\log g$ is constant within the envelope. The chemical composition controls opacity and sound speed, which, finally, has an impact on the pulsating properties of the model.

For the given combination of input parameters in the first step the LHD code calculates the hydrostatically stratified 1D atmosphere. Then, for this structure the code calculates the initial velocity perturbation profile in a fundamental frequency. Depending on the choice, it performs calculation of the convective flux according to MLT or Stellingwerf's theory. The basic problem is related with calculation of the energy equation (Eq. 26) for the next time step. In order to avoid numerical problems due to significant changes of convective and radiation fluxes or steep velocity gradients, one has to accurately choose the time step. When the energy equation is solved, then one can update the dynamical equation and recalculate the fluxes for further iterations of the energy equation. Within the LHD code, the update of the energy equation is implemented with the semi-implicit fashion, which will be described in Sec. 2.6.1. A complete numerical scheme of the LHD is shown in Fig. 9. My own contribution and modifications are indicated by the blue color, which includes the initial and boundary conditions to excite pulsations. I included an implementation of the Stellingwerf time-dependent theory of convection.

The mass of the 1D modeled atmosphere is partitioned by approximately 260 mass elements representing a plane-parallel "layer". The material within each "layer" is considered to be thermodynamically homogeneous. The LHD code functions by using a staggered mesh. Thermodynamic quantities are calculated in centers of mass elements. But dynamic quantities, optical depths, and convection velocities as well as fluxes are calculated on edges of mass elements.

2.6.1 Semi-implicit method for the update of energy equation

The evolution of the internal energy e of the volume element depends on the energy flux differences across cell interfaces. The solution of the energy equation is implemented numerically by the explicit time stepping. One can try to implement a fully implicit scheme, but it usually leads to large, complicated systems of equations to solve, and has to be well tested. Hence, one seeks a simpler approximate method.

The time step has to agree with the characteristic time scales. The convection time scale is

$$\tau_{\text{conv}} \sim \frac{H_p}{v_{\text{conv}}}, \quad (84)$$

where H_p is a pressure scale and v_{conv} is convective velocity.

The time scale, which is related with the change of the thermal energy of a mass element due to

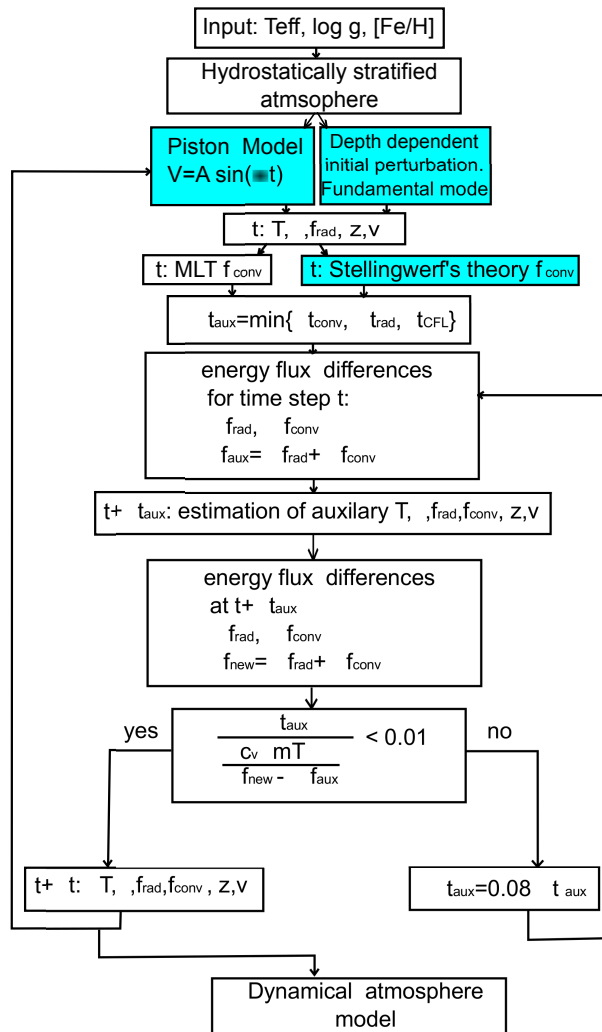


Figure 9: The block scheme of the LHD code, which performs calculations of 1D plane-parallel LTE atmosphere models. I marked the blocks of which I have contributed to get dynamical stellar atmosphere models with a blue color.

the convective and radiative transport of energy defined as,

$$\tau_{\text{th}} \sim \frac{C_v T}{f_{\text{rad}} + f_{\text{conv}}}. \quad (85)$$

The other time scale that one needs to take into account is related to the Courant–Friedrichs–Lewy (CFL) condition, which is the necessary condition for stability while solving equations numerically by the explicit method of finite differences,

$$\tau_{\text{CFL}} \sim \frac{\Delta z}{c_s}, \quad (86)$$

where Δz is a cell size related with a mass element $\Delta z = \Delta m / \rho$.

Let's assume, that all dynamic and thermodynamic parameters are known for the current time level t_0 , or in other words, the structure of the stellar atmosphere is known for the instance in time t_0 . The goal is then to calculate the heating rate. In order to do so, one can compute the total flux divergence $\text{div} f$ by taking total flux differences across cell boundaries into account. For the j -th cell with boundaries z_{j+1} and z_j , one can write

$$\text{div} f = \frac{f_{j+1} - f_j}{z_{j+1} - z_j}, \quad (87)$$

where the total flux on the boundary z_j is $f_j = f_{\text{rad},j} + f_{\text{conv},j}$, which is a sum of the convective and radiative fluxes.

This energy flux difference leads to a change in the thermal energy e for the cell element such that $\frac{De}{Dt} = -\frac{1}{\rho} \text{div} f \equiv R$, where R is the rate of change of the thermal energy.

In the case where the explicit time step, strong energy fluxes produce drastic changes of thermodynamic parameters. As a consequence, it leads to loss of the numerical accuracy and, potentially, numerical stability. Therefore it is preferable to deal with the implicit time stepping, which provides numerical stability and independence of the stability on a time step. However, in order to know the physical conditions in the model at a given future time $t_0 + \Delta t$, one has to solve a complicated non-linear system of equations. Another method to find a solution is considering a local approximation.

One can apply a simpler, semi-implicit method in order to obtain a solution for the energy equation. Let's assume that there is an estimate of the rate \hat{R} for the time step $t_0 + \Delta t$. The approximate rate of change of the thermal energy at the current time step can be estimated as mean rate $\frac{R_0 + \hat{R}}{2}$ between t_0 and $t_0 + \Delta t$ with the second order accurate:

$$\Delta \hat{e} = \frac{R_0 + \hat{R}}{2} \Delta t \quad (88)$$

From the other side, the estimate of the thermal energy with second order accurate is a mean

between the second order accurate estimate of rate R at time $t_0 + \Delta t$, which is unknown, and the current value R_0 :

$$\Delta e = \frac{R_0 + R}{2} \Delta t \quad (89)$$

So, a difference δe between the second order accurate estimate and approximate rates is

$$\delta e \equiv \Delta e - \Delta \hat{e} = \frac{R - \hat{R}}{2} \Delta t \quad (90)$$

The difference is related also with a temperature difference δT assuming constant density:

$$\delta e = C_v \delta T \quad (91)$$

One can arrive at the the next expression for the temperature difference:

$$\delta T = \frac{R - \hat{R}}{2c_v} \Delta t \quad (92)$$

For the approximate rate \hat{R} one can calculate the approximate pressure \hat{p} and temperature \hat{T} for the time step $t_0 + \Delta t$, and then, derive the radiative \hat{F}_{rad} and convective \hat{F}_{conv} fluxes. So, one can get a new estimate of the rate R^* .

The difference between the second order accurate estimate R and the new R^* estimated rates is related with a certain temperature difference δT :

$$\frac{R^* - R}{\delta T} = \Theta, \quad (93)$$

where Θ describes the change of the flux divergence. Combining (92) and (93) one can get the second order accurate estimate of rate R :

$$R = \frac{R^* + \frac{\beta_0 \Delta t}{2} \hat{R}}{1 + \frac{\beta_0 \Delta t}{2}}, \quad (94)$$

where $\beta_0 = \frac{\Theta}{c_v}$ is in units of inverse time s^{-1} . Physically, $\frac{1}{\beta_0}$ is a characteristic time scale of changing of the temperature for δT with a given rate R .

Mathematically, the rate R is a weighted mean rate between the approximate \hat{R} and new estimated R^* values:

$$R = \hat{w} \hat{R} + w^* R^*, \quad (95)$$

where the $\hat{w} = \frac{1}{1 + \frac{\beta_0 \Delta t}{2}}$ and $w^* = \frac{\frac{\beta_0 \Delta t}{2}}{1 + \frac{\beta_0 \Delta t}{2}}$ are weights related with a condition $\hat{w} + w^* = 1$.

To summarize, the algorithm of the iterative solution of the energy equation is as follow:

1. Initial estimation of the time step $\Delta t = \Delta t_{\text{ini}}$ from comparison of the time scales given by

Eq. 84 - 86.

2. Taking the approximate rate $\hat{R} = R_0$ one derives all dynamic and thermodynamic parameters (R^*, T^*, p^*, \dots) for the new time step $t_0 + \Delta t$. Then, one calculates the new rate $R^* = -\frac{\text{div}F(T^*, p^*)}{\rho^*}$.

- An estimation of the factor $\beta_0 \Delta t$, which shows changing of the rate during the time step Δt .
- If this factor is greater than the threshold value $r_{\max} = 0.01$, there is a huge difference between the new derived parameters (R^*, T^*, p^*, \dots) and the approximate values ($\hat{R}, \hat{T}, p^* \dots$). Physically, this means that the thermodynamic parameters of the system at the new instance in time $t_0 + \Delta t$ change drastically with respect to the previous instance at time t_0 . One has to decrease the time step $\Delta t = r_t \Delta t$, where $r_t < 1.0$, and go to step 2.
- If the factor $\beta_0 \Delta t < r_{\min} = 10^{-5}$ then the code performs the next time step without iteration.
- In a case of $r_{\min} < \beta_0 \Delta t < r_{\max}$ the code performs the iteration in step 3.

3. Calculation of a new approximate rate $\hat{R} = \frac{R^* + \frac{\beta_0 \Delta t}{2} \hat{R}}{1 + \frac{\beta_0 \Delta t}{2}}$ and go to the step 2.

Since R linearly depends on the total energy flux, one can split the equation (94) into radiative and convective flux rates:

$$R_{\text{rad}} = \frac{R_{\text{rad}}^* + \frac{\beta_{0,\text{rad}} \Delta t}{2} \hat{R}_{\text{rad}}}{1 + \frac{\beta_{0,\text{rad}} \Delta t}{2}} \quad (96)$$

and

$$R_{\text{conv}} = \frac{R_{\text{conv}}^* + \frac{\beta_{0,\text{conv}} \Delta t}{2} \hat{R}_{\text{conv}}}{1 + \frac{\beta_{0,\text{conv}} \Delta t}{2}}, \quad (97)$$

where $1/\beta_{0,\text{conv}}$ and $1/\beta_{0,\text{rad}}$ describe typical time scales of change the thermal energy of a cell due to the convective or radiative transport of energy.

2.7 Numerical implementation of the Stellingwerf theory

The numerical implementation of Eq. 56 describing the temporal and spatial evolution of the twice convective kinetic energy per unit of mass consists of two steps. First, one has to construct a difference scheme. Secondly, the numerical stability of the difference scheme has to be investigated. However, the equation is non-linear, which introduces difficulties when computing a solution and investigating the stability.

2.7.1 Numerical scheme

My goal is to construct a second-order linear implicit numerical scheme, that can be solved easily. I introduce the integer indexes j and n , that are related with cell centered parameters, where j is a spatial index, and n is a temporal index. Fractional indexes $j \pm \frac{1}{2}$, $n \pm \frac{1}{2}$ are related with edge centered parameters. All parameters are known at n -th time step. One wants to derive the twice convective kinetic energy per unit of mass ω_j^{n+1} at instance in time of t_{n+1} . I assume, the time step in my calculation is not so big to produce significant changes of parameters. It allows to replace the non-linear terms $\sqrt{\omega_j^{n+1}}$ at the next instance in time by current values $\sqrt{\omega_j^{n+1}} \approx \sqrt{\omega_j^n}$ as well as dynamic and thermodynamic quantities. This leads to the numerical scheme, which is linear relative to ω_j^{n+1} :

$$\frac{\omega_j^{n+1} - \omega_j^n}{\Delta t} = F(\omega_j^{n+1}, \rho_j^n, \sqrt{\omega_j^n}, \dots), \quad (98)$$

where F is a linear function of ω_j^{n+1} . One can write all cell centered spatial derivatives in the Lagrangian formalism using $dr = \frac{dm}{\rho}$. Then, the diffusion term splits into two terms:

$$l \frac{\partial \sqrt{\omega}}{\partial z} \frac{\partial \omega}{\partial z} = l_j^n \cdot \left(\frac{\rho_j^n}{\Delta m_j} \right)^2 \left(\sqrt{\omega_{j+\frac{1}{2}}^n} - \sqrt{\omega_{j-\frac{1}{2}}^n} \right) \cdot \left(\omega_{j+\frac{1}{2}}^{n+1} - \omega_{j-\frac{1}{2}}^{n+1} \right), \quad (99)$$

where $\omega_{j \pm \frac{1}{2}}^{n+1} = (\omega_j^{n+1} + \omega_{j \pm 1}^{n+1})/2$, and

$$l \sqrt{\omega} \frac{\partial^2 \omega}{\partial z^2} = l_j^n \sqrt{\omega_j^n} \frac{\rho_j^n}{\Delta m_j} \left[\frac{\rho_{j+\frac{1}{2}}^n}{\Delta m_{j+\frac{1}{2}}} \left(\omega_{j+1}^{n+1} - \omega_j^{n+1} \right) - \frac{\rho_{j-\frac{1}{2}}^n}{\Delta m_{j-\frac{1}{2}}} \left(\omega_j^{n+1} - \omega_{j-1}^{n+1} \right) \right]. \quad (100)$$

One gets a simple expression for the source term

$$\sqrt{\omega} \cdot \frac{\omega_0 - \omega}{\lambda_0} = \frac{\sqrt{\omega_j^n}}{l_j^n} \left[\omega_{0j}^n - \omega_j^{n+1} \right] \quad (101)$$

and for the part describing the interaction of convection with velocity field

$$2\omega \frac{\partial u}{\partial z} = 2\omega_j^{n+1} \frac{\rho_{j+\frac{1}{2}}^n}{\Delta m_{j+\frac{1}{2}}} \left(u_{j+\frac{1}{2}}^n - u_{j-\frac{1}{2}}^n \right) \quad (102)$$

Let's introduce the following variables:

$$A_j = \Delta t \left[l_j^n \sqrt{\omega_j^n} \frac{\rho_j^n}{\Delta m_j} \frac{\rho_{j-\frac{1}{2}}^n}{\Delta m_{j-\frac{1}{2}}} - 0.5 \cdot l_j^n \cdot \left(\frac{\rho_j^n}{\Delta m_j} \right)^2 \cdot \left(\sqrt{\omega_{j+\frac{1}{2}}^n} - \sqrt{\omega_{j-\frac{1}{2}}^n} \right) \right], \quad (103)$$

$$B_j = \Delta t \left[-l_j^n \sqrt{\omega_j^n} \frac{\rho_j^n}{\Delta m_j} \left(\frac{\rho_{j-\frac{1}{2}}^n}{\Delta m_{j-\frac{1}{2}}} + \frac{\rho_{j+\frac{1}{2}}^n}{\Delta m_{j+\frac{1}{2}}} \right) - \frac{\sqrt{\omega_j^n}}{l_j^n} - 2 \frac{\rho_{j+\frac{1}{2}}^n}{\Delta m_{j+\frac{1}{2}}} \left(u_{j+\frac{1}{2}}^n - u_{j-\frac{1}{2}}^n \right) \right] - 1 \quad (104)$$

$$C_j = \Delta t \left[l_j^n \sqrt{\omega_j^n} \frac{\rho_j^n}{\Delta m_j} \frac{\rho_{j+\frac{1}{2}}^n}{\Delta m_{j+\frac{1}{2}}} + 0.5 \cdot l_j^n \cdot \left(\frac{\rho_j^n}{\Delta m_j} \right)^2 \cdot \left(\sqrt{\omega_{j+\frac{1}{2}}^n} - \sqrt{\omega_{j-\frac{1}{2}}^n} \right) \right] \quad (105)$$

$$D_j = -\omega_j^n - \Delta t \frac{\sqrt{\omega_j^n}}{l_j^n} \omega_{0j}^n \quad (106)$$

Omitting intermediate mathematical steps one, finally, gets the tridiagonal system of linear algebraic equations to calculate ω^{n+1} :

$$A_j \omega_{j-1}^{n+1} + B_j \omega_j^{n+1} + C_j \omega_{j+1}^{n+1} = D_j, \quad (107)$$

where $[A, B, C]$ is the $M \times M$ tridiagonal matrix, D is a $M \times 1$ vector. At the top $j = N$ and bottom $j = 0$ boundaries I put $\omega_0 = \omega_N = 0$. System of the equations one can easy solve with taken boundary conditions for the each time step. However, one has to investigate the numerical stability of the numerical scheme on a size of the time step.

2.7.2 Stability analysis

Generally, the investigation of the stability of a numerical scheme of a non-linear differential equation is a complex problem. In this section, I shall use the Von Neumann stability analysis in order to investigate the stability of the difference scheme applied for the linearized equation. The resulting condition is necessary but not sufficient for stability. The goal is to understand the behavior of the amplitude of the solution in plane-wave regime as a function of the time step. The amplitude of the stable scheme has to be bounded.

First, I perform a linearization of the scheme by introducing several physical time scales:

- The diffusion time scale $\tau_{\text{diff}} \equiv dz^2/D$, which is related to the diffusion coefficient $D(z, t) \equiv l\omega^{1/2}$.
- The source time scale $\tau_s(z, t) \equiv \frac{\omega^{1/2}}{l}$.
- The time scale of the interaction of convective energy with the velocity field $\tau_u(z, t) \equiv \frac{\partial z}{\partial u}$.

The linearized equation is

$$\frac{\partial \omega}{\partial t} = D \frac{\partial^2 \omega}{\partial z^2} + \frac{\partial D}{\partial z} \frac{\partial \omega}{\partial z} + \frac{(\omega_0 - \omega)}{\tau_s} - 2 \frac{\omega}{\tau_u} \quad (108)$$

The difference scheme with implicit time stepping as in a previous section is

$$\begin{aligned} \frac{\omega_j^{n+1} - \omega_j^n}{\Delta t} &= \frac{D_j^n}{\Delta z^2} (\omega_{j+1}^{n+1} - 2\omega_j^{n+1} + \omega_{j-1}^{n+1}) + \frac{1}{4\Delta z^2} (\omega_{j+1}^{n+1} - \omega_{j-1}^{n+1})(D_{j+1}^n - D_{j-1}^n) + \\ &+ \frac{1}{(\tau_s)_j^n} ((\omega_0)_j^{n+1} - \omega_j^{n+1}) - 2\omega_j^{n+1} \frac{1}{(\tau_u)_j^n}, \end{aligned} \quad (109)$$

One can find the the solution of Eq. 109 in the form of Fourier series

$$\omega_j^n = \sum_k A_k e^{i\alpha_k j \Delta z} e^{i\Omega n \Delta t} \quad (110)$$

and

$$(\omega_0)_j^n = \sum_k \widetilde{A}_k e^{i\alpha_k j \Delta z} e^{i\Omega n \Delta t} \quad (111)$$

So, the initial values could be expressed in a form

$$\omega_j^0 = \sum_s A_s e^{i\alpha_s j \Delta z} \quad (112)$$

and

$$\omega_{j-1}^n = \sum_s A_s e^{i\alpha_s (j-1) \Delta z} e^{i\Omega n \Delta t}, \quad (113)$$

$$\omega_j^{n+1} = \sum_s A_s e^{i\alpha_s j \Delta z} e^{i\Omega (n+1) \Delta t}, \quad (114)$$

$$\omega_{j+1}^n = \sum_s A_s e^{i\alpha_s (j+1) \Delta z} e^{i\Omega n \Delta t}, \quad (115)$$

$$\omega_{j+1}^{n+1} = \sum_s A_s e^{i\alpha_s (j+1) \Delta z} e^{i\Omega (n+1) \Delta t}. \quad (116)$$

Let's consider evolution of the individual Fourier components:

$$\begin{aligned} \frac{e^{i\Omega \Delta t} - 1}{\Delta t} &= \frac{D_j^n e^{i\Omega \Delta t}}{\Delta z^2} (e^{i\alpha_k \Delta z} - 2 + e^{-i\alpha_k \Delta z}) + \frac{e^{i\Omega \Delta t}}{4\Delta z^2} (e^{i\alpha_k \Delta z} - e^{-i\alpha_k \Delta z}) \cdot \\ &\cdot (D_{j+1}^n - D_{j-1}^n) + \frac{e^{i\Omega \Delta t}}{(\tau_s)_j^n} \left(\frac{\widetilde{A}_k}{A_k} - 1 \right) - 2 \frac{e^{i\Omega \Delta t}}{(\tau_u)_j^n}, \end{aligned} \quad (117)$$

which could be transformed to

$$e^{i\Omega \Delta t} \left(1 + \frac{4D_j^n \Delta t}{\Delta z^2} \sin^2 \frac{\alpha_k \Delta z}{2} - \frac{i \cdot \Delta t}{2\Delta z^2} \sin \alpha_k \Delta \cdot (D_{j+1}^n - D_{j-1}^n) + \frac{\Delta t}{(\tau_s)_j^n} \left(1 - \frac{\widetilde{A}_k}{A_k} \right) + 2 \frac{\Delta t}{(\tau_u)_j^n} \right) = 1 \quad (118)$$

Stability requires $|e^{i\Omega\Delta t}| \leq 1$, so

$$|e^{i\Omega\Delta t}| = \left| \frac{1}{1 + \frac{4D_j^n \Delta t}{\Delta z^2} \sin^2 \frac{\alpha_k \Delta z}{2} - \frac{i \cdot \Delta t}{2\Delta z^2} \sin \alpha_k \Delta \cdot (D_{j+1}^n - D_{j-1}^n) + \frac{\Delta t}{(\tau_s)_j^n} \left(1 - \frac{\widetilde{A}_k}{A_k}\right) + 2 \frac{\Delta t}{(\tau_u)_j^n}} \right| \leq 1, \quad (119)$$

which one can transform into the next expression

$$\left| 1 + \frac{4D_j^n \Delta t}{\Delta z^2} \sin^2 \frac{\alpha_k \Delta z}{2} - \frac{i \cdot \Delta t}{2\Delta z^2} \sin \alpha_k \Delta \cdot (D_{j+1}^n - D_{j-1}^n) + \frac{\Delta t}{(\tau_s)_j^n} \left(1 - \frac{\widetilde{A}_k}{A_k}\right) + 2 \frac{\Delta t}{(\tau_u)_j^n} \right| \geq 1. \quad (120)$$

Then, one can use the inequality $|\alpha + \beta| \leq |\alpha| + |\beta|$ and apply for Eq. 120

$$1 + \Delta t \left[\frac{4D_j^n}{\Delta z^2} \left| \sin^2 \frac{\alpha_k \Delta z}{2} \right| + \frac{1}{2\Delta z^2} \cdot |\sin \alpha_k \Delta z| \cdot |D_{j+1}^n - D_{j-1}^n| + \frac{1}{(\tau_s)_j^n} \left| 1 - \frac{\widetilde{A}_k}{A_k} \right| + 2 \frac{1}{(\tau_u)_j^n} \right] \geq 1, \quad (121)$$

which is always holds, because the expression in brackets is larger or at least equal to zero. That means, the numerical scheme (Eq. 109) is unconditionally stable. One can implement the numerical scheme and perform further calculations of Cepheid models.

2.8 A model for the classical Cepheid KQ Scorpii

Dynamical model atmospheres of pulsating stars can help to model the impact of pulsations on spectroscopic properties and chemical analysis. The thermal structure of the pulsating star changes during the pulsational cycle. During compressions and expansions the velocity field within the stellar atmosphere changes. One of the key questions of these modeling trying to understand a change of the velocity field of line formation regions during the pulsational cycle. The microturbulent velocity, ξ_t , is one of parameters in spectroscopic analysis, which physically characterizes velocities on scales having $\Delta\tau \lesssim 1$, and it can depend on the large-scale velocity field. In order to get the qualitative answers for the addressed questions I investigated the classical Cepheid of KQ Sco. The reason for the choice was that belonged to an observational survey of Cepheids led by Dr. Maria Bergemann and Dr. Laura Inno.

2.8.1 Observational data

KQ Sco is a classical fundamental mode Cepheid with the period of pulsations 29 days. The radial velocity curve is shown on Fig.10, and it is based on measurements of Coulson and Caldwell (1985). Photometric light curves in H, J and K bands are shown in Fig.11, and were measured by Coulson and Caldwell (1985); Laney and Stobie (1992); Welch et al. (1984).

Spectroscopic data were downloaded from the European South observatory (ESO) archive. Eight

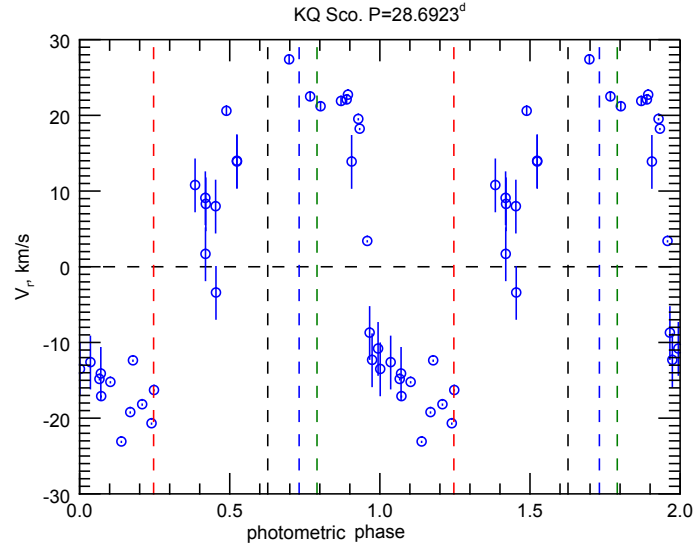


Figure 10: Radial velocity curve of KQ Sco. The systemic velocity of -30.30 km s^{-1} , which is based on measurements of Storm et al. (2011), was removed from the curve. Vertical dashed lines show photometric phases, for which spectroscopic data is given. By definition, zero photometric phase corresponds to the maximum light on a light curve.

high-resolution spectra ($R \approx 38000$) for four different pulsational phases were collected with the Ultraviolet and Visual Echelle Spectrograph³ (UVES) at the ESO Very Large Telescope (VLT) covering wavelength ranges of $4790 - 5750 \text{ \AA}$ and $5833 - 6806 \text{ \AA}$. The mean S/N ratios of the spectra for the spectral wavelength are around 100. One has to emphasize, that spectra have the barycentric velocity correction, and the velocity zero point in spectra is relative to the barycenter of the Solar System. Within ranges of around 100 \AA around considered lines, which will be described further, spectra were normalized with 2-nd order polynomials.

A spectroscopic investigation of KQ Sco was conducted by Andrievsky et al. (2002a) with 1D plane-parallel hydrostatic stellar atmosphere models for the photometric phase of $\phi_{\text{ph}} = 0.940$. The photometric phase of zero corresponds to the phase of maximum light of the light curve. Estimated atmospheric parameters were $T_{\text{eff}} = 5058 \text{ K}$, $\log g = 1.10$, $\xi_t = 5.70 \text{ km s}^{-1}$, and $[\text{Fe}/\text{H}] = 0.16 \text{ dex}$, which should be physically independent of the phase of pulsations, for one particular phase of pulsations. Then derived parameters were improved by studies of Genovali et al. (2014, 2015) with high-resolution data. The iron abundance was obtained to $[\text{Fe}/\text{H}] = 0.22 \text{ dex}$. Due to the high metallicity the spectra show strong blending. Taking into account the observational data and a line list, which was used by Genovali et al. (2014, 2015), I select 3 spectral lines of Fe I for further investigation. The line data with wavelengths, oscillator strengths, excitation potential, and van der Waals line broadening parameter are presented in Table 1. The lines were selected with a condition of minimum blending, allowing one to measure the equivalent widths (EW) W of the

³<http://www.eso.org/sci/facilities/paranal/instruments/uves.html>

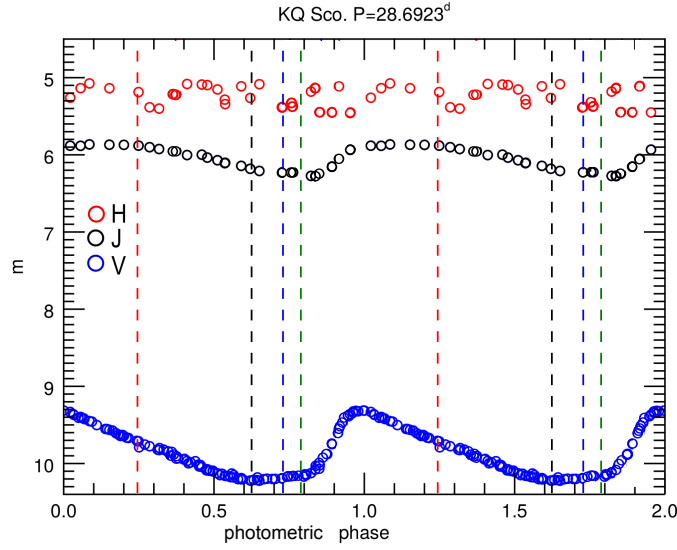


Figure 11: Photometric light curves of KQ Sco in the H, J and K band. Vertical dashed lines show photometric phases, for which spectroscopic data are given.

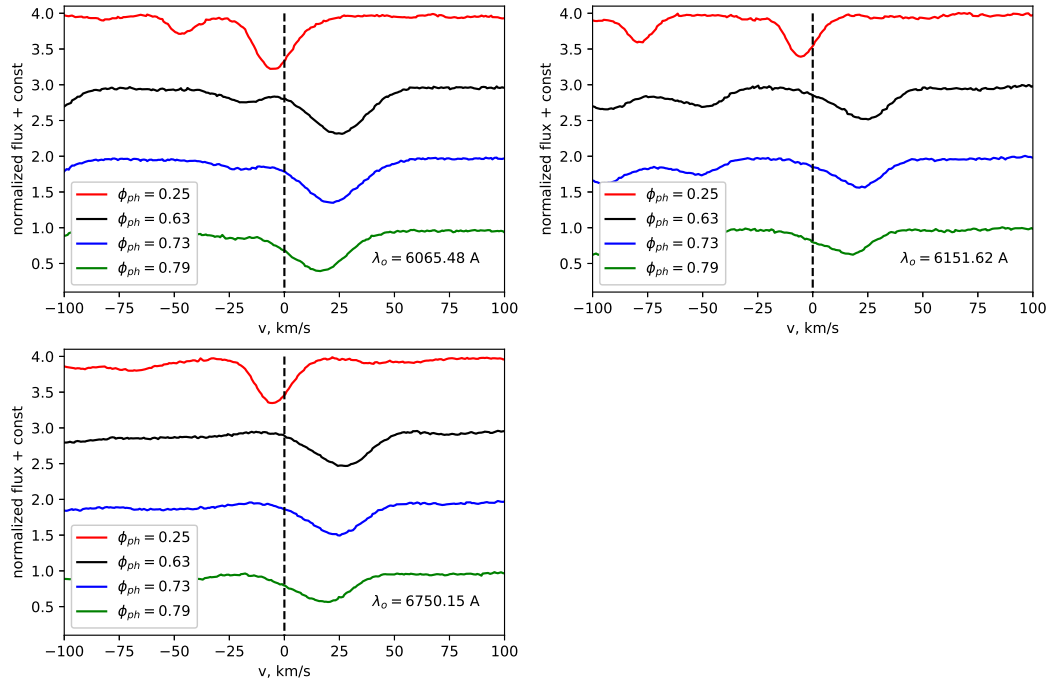


Figure 12: Observed Fe I 6065 Å, 6151 Å, and 6750 Å line profiles during the pulsational cycle of KQ Sco.

lines, defined by the expression:

$$W_\lambda = \int (1 - F_\lambda / F_c) d\lambda, \quad (122)$$

Table 1: The list of lines, which was selected for further spectroscopic investigation. The oscillator strengths $\log gf$, excitation potentials χ_i , and van der Waals line broadening parameter $\frac{\gamma_6}{N_H}$ were taken from the Vienna Atomic Line Database (VALD).

element	λ , Å	$\log gf$	χ_i , eV	$\log \frac{\gamma_6}{N_H}$
Fe I	6065.48	-1.53	2.609	-7.77
Fe I	6151.62	-3.27	2.176	-7.76
Fe I	6710.31	-4.88	1.49	-7.78

where F_c is the continuum flux and F_λ is the flux variation as a function of wavelength across the line profile. The equivalent width is used in the chemical analysis in order to derive the abundance of the chemical element.

Variations of the line profiles for four photometric phases are shown in Fig. 12. Lines are blue shifted for the photometric phase of 0.25 with an amplitude of the radial velocity $\approx 5 \text{ km s}^{-1}$ near the phase of maximum expansion. Line profiles are almost symmetric. However, for three next phases $\phi_{\text{ph}} = 0.63, 0.73,$ and 0.79 line profiles have the classical asymmetric pulsational shape (Shapley and Nicholson, 1919) due to the higher velocity amplitudes of $15 - 25 \text{ km s}^{-1}$. However, to first approximation, I derive equivalent widths of these lines with Gaussian fitting, which is shown in Sec. 6 in Figs. 54-56. For line profiles of blending lines I also assumed a Gaussian shape.

2.8.2 The one-dimensional LHD model for KQ Scopii

A one-dimensional dynamical LHD model was calculated for an initially hydrostatically stratified atmosphere model with $T_{\text{eff}} = 5000 \text{ K}$, $\log g = 1.0 \text{ dex}$, and $[\text{Fe}/\text{H}] = 0.0$ applying Stellingwerf's theory of convection. I took a metallicity of $[\text{Fe}/\text{H}] = 0.0$, because the tabulated equation of state and opacity tables are given on a grid of metallicities only. I choose the nearest available value to the metallicity of KQ Sco.

The depth of the bottom boundary was chosen to get a fundamental period close to the one observed in KQ Sco. The initial top amplitude of velocity perturbation was chosen to 35 km s^{-1} . Evolutions of the bolometric, V band fluxes, and radial velocity are showed on Fig. 13 after reaching the pulsational limit cycle with a pulsational period of 34 days, which is quite close to the period of KQ Sco.

As one can see, the shape of the light curve of the model is more symmetric relatively to the phase of maximum light at $\phi_{\text{ph}} = 0$. The peak to peak variation in the V band $\Delta m_V = 1.3^{\text{m}}$, while KQ Sco exhibits a variation of $\Delta m_V = 1.1^{\text{m}}$. The observed radial velocity curve is based on spectroscopic measurements of spectral lines, which are disk integrated including limb darkening and expansion effects. The observed spectroscopic radial velocity v_{spec} is proportional to the velocity of the photosphere v_{ph} . The constant of proportionality is the p-factor defined via $v_{\text{ph}} = p v_{\text{spec}}$, the key-quantity for the Baade-Wesselink method for the determination of distances (Baade, 1926;

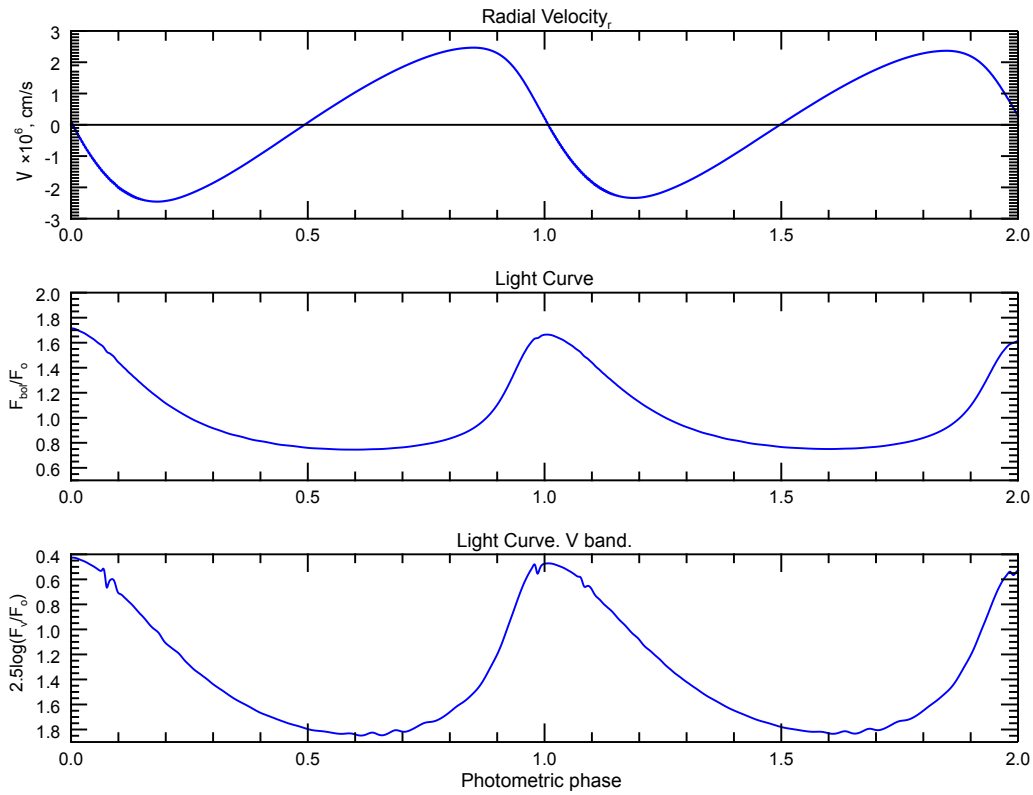


Figure 13: Dynamical 1D LHD model of a Cepheid with $T_{\text{eff}} = 5000$ K, $\log g = 1.0$ dex, and $[\text{Fe}/\text{H}] = 0.0$ with a period of pulsations of 34 days. Top panel: radial velocity of the optical depth surface near the photosphere with $\log \tau_R = -0.5$. Middle panel: Bolometric light curve. Bottom panel: Light curve in the V band.

Wesselink, 1946). The velocity of the photosphere according to the radial velocity in Fig. 13 is $v_{\text{ph}} \approx 25 \text{ km s}^{-1}$, taking a p-factor $p = 1.3$ one gets the spectroscopic velocity amplitude of the model of $\sim 19 \text{ km s}^{-1}$, which is very close to the observed value.

However, my goal is not related with the precise calculation and analysis of the radial velocity and light curves. I am more focused on spectroscopic properties, formation of spectral lines in the dynamical atmosphere. I have "snapshots" from the dynamical atmosphere model for each modeled instance of time. I select 25 snapshots with a step $\Delta\phi_{\text{ph}} = 0.04$ in photometric phase in order to cover one full pulsational cycle and perform further spectral synthesis.

2.8.3 Theoretical line profiles and equivalent widths

The spectral synthesis of the Fe I 6065 Å, 6151 Å, and 6750 Å lines has been done with the Linfor3D⁴ code in LTE approximation. Originally, Linfor3D is a code to perform the spectral synthesis of local-box 2D and 3D radiation-hydrodynamical convective atmospheres. In order to perform the spectral synthesis with the calculated model I construct a horizontally uniform plane-parallel 3D cube based replicating horizontally the calculated 1D structure. In the present case, Linfor3D was set-up to solve the radiative transfer equation for a specified interval of wavelengths along three inclined angles for two azimuthal angles for the continuum and line intensities for each wavelength. It also computes line profiles in terms of flux and equivalent widths of input lines individually for 25 instances in time, "snapshots", equidistantly covering the pulsational cycle.

The microturbulent velocity, which is physically characterizing velocities on scales within the line formation region and spectroscopically introduced to explain the observed fact that the equivalent widths of strong lines are greater than predicted by models based on thermal and damping broadening alone, was varied from 3.5 to 6 km s^{-1} . The equivalent width of a weak spectral line depends on the product of the abundance A and oscillator strength gf , on a logarithmic scale as $\log A + \log gf$. For a fixed $\log gf$ the iron abundance, metallicity, $[\text{Fe}/\text{H}]$ was changed between $-0.5 \dots -0.25$ dex and $0.25 \dots 0.5$ dex with in steps of 0.25 dex.

Figure 14 shows the temporal evolution of the normalized theoretical Fe I $\lambda = 6151 \text{ Å}$ line profiles within the pulsational cycle for four metallicities of -0.25, 0, 0.25, and 0.5 for a microturbulent velocity of $\xi = 3.5 \text{ km s}^{-1}$. The calculated line profiles have an infinite signal-to-noise ratio an infinite instrumental resolution, and tend to show a multicomponent structure. The line profiles are broadened only by thermal broadening, microturbulence, and van der Waals broadening. For phases with maximum velocities of expansion and contraction the line profiles have an asymmetrical shape.

I compare equivalent widths of observed and calculated spectral lines. It is motivated due to the strong dependance of the line profile on the pulsational velocity, blending effects, infinite

⁴<http://www.aip.de/Members/msteffen/linfor3d/>.

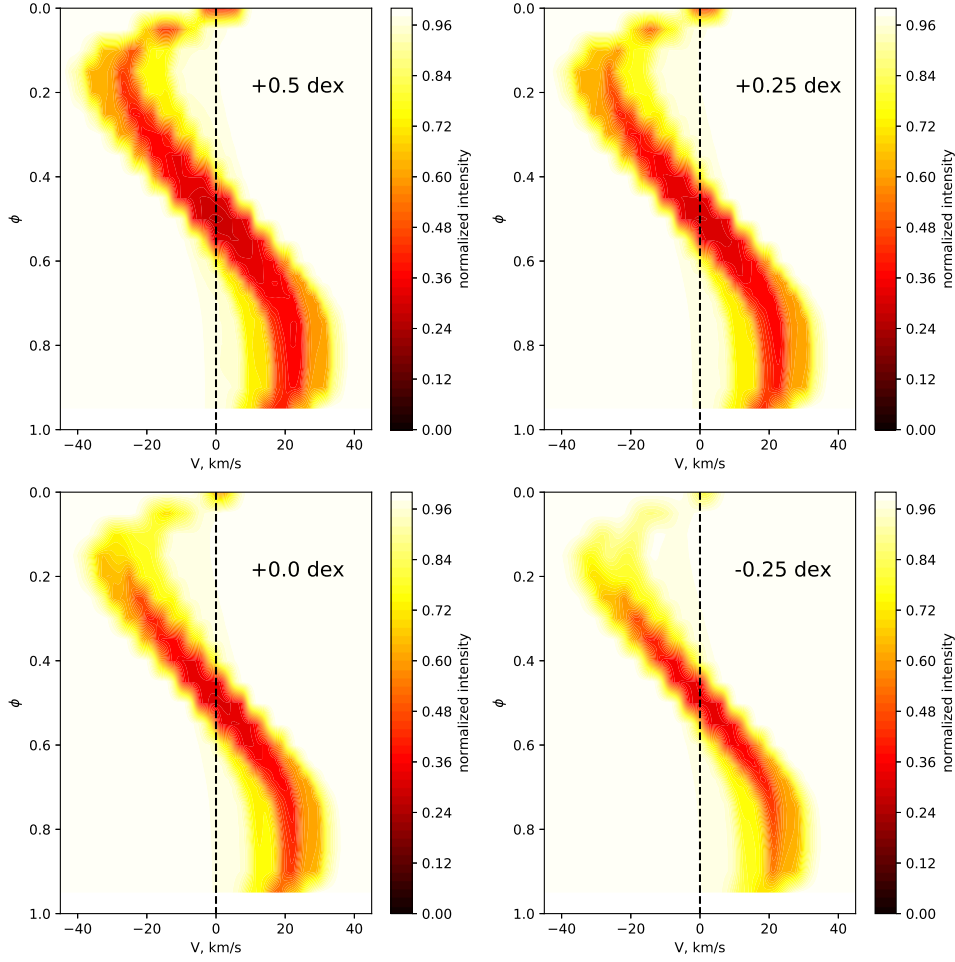


Figure 14: Normalized theoretical line profiles of Fe I $\lambda = 6151 \text{ \AA}$ line for four different metallicities and a microturbulent velocity $\xi = 3.5 \text{ km s}^{-1}$ as a function of the pulsational phase. The pulsational phase is indicated along the vertical direction. Positive velocities correspond to receding motion (red-shifted). The color bar for each line (indicating the flux) is from 0.0 to 1.0.

resolution of theoretical line profiles, which one has to convolve with the instrumental profile, and due to additional systematic effects produced by different radial velocities of the model and in observations. Additionally, the equivalent width of a spectral line is an invariant in the convolution procedure.

Theoretical and observed equivalent widths of the Fe I 6065 \AA , 6151 \AA , and 6750 \AA lines as functions of the pulsational phase are shown in Fig. 15, 16, and 17. Theoretical equivalent widths were calculated for five different metallicities and microturbulent velocities.

EWs have a clear modulation with the phase of pulsations. For the lowest effective temperatures during the pulsational cycle with a photometric phase $\phi_{\text{ph}} = 0.5 - 0.6$, which corresponds to maximum expansion and start of contraction, theoretical EWs reach their maximum. At the

phase of maximum compression $\phi_{\text{ph}} = 0$, which coincides with the maximum light, and, as a consequence, highest effective temperature of ≈ 5700 K, the equivalent widths have a clear minimum. Hence, there is a clear anti-correlation between the effective temperature and EWs of the Fe I lines. There is a physical reason for it. The equivalent width of a spectral line is most sensitive to temperature variations. For a temperature range near maximum compression most of the neutral iron is ionized, i.e. Fe II is the majority species. Due to the expansion the temperature drops, and more neutral iron atoms form from Fe I. As a result, one has more neutral iron, which absorbs more light at given wavelengths, and equivalent widths increase.

As one can see, the increase of the microturbulent velocity and metallicity has the same effect, they increase the line strength. In other words, the equivalent width of a strong line is degenerated with respect to ξ and [Fe/H]. In order to resolve the degeneracy, traditionally, one takes a weak line of the same element, which is insensitive to the change of the microturbulent velocity. Thus, taking together weak and strong lines one derives ξ and [Fe/H] trying to get the same abundance for all lines. However, the measurement of EWs of weak lines is difficult because of blending. As a consequence, it is not trivial to resolve the degeneracy. My goal is to characterize the microturbulent velocity and dynamical properties of the pulsating atmosphere. One can apply an independent method for fixing of the metallicity applying relations between the pulsational period, luminosity, and metallicity (Marconi et al., 2005; Nemeč et al., 1994; Ngeow et al., 2012; Szabados and Klagyivik, 2012). Let us assume, that one fix the metallicity, which is constant over the pulsational cycle. In my analysis of the microturbulent velocity I take the estimation of metallicity of the KQ Sco by Genovali et al. (2014), [Fe/H] = 0.22. Fixing the metallicity one can solve the degeneracy for the considered lines.

For the Fe I 6065 Å line one has to change the microturbulent velocity in a range $\xi \approx 4.25 \dots 6 \text{ km s}^{-1}$ in order to match observed equivalent widths. For the Fe I 6151 Å line one has to change the microturbulent velocity in a range $\xi \approx 3.9 \dots 5.15 \text{ km s}^{-1}$ in order to match observed equivalent widths. The microturbulent velocity of Fe I 6759 Å line varies in a range $\xi \approx 4.4 \dots 5.1 \text{ km s}^{-1}$. The microturbulent velocity, which is a result of averaging over all lines, is in agreement with the derivation of Andrievsky et al. (2002a). All lines show the maximum of the microturbulent velocity at the photometric phase $\phi_{\text{ph}} \approx 0.6 \dots 0.7$. The microturbulent velocity characterizes motions on scales $\Delta\tau_{\text{R}} \lesssim 1$ smaller than the line-formation region. These "small-scale" motions can be induced by convection or pulsations and, finally, produce velocity gradients along the line-of-sight, which one sees as microturbulence. From this point of view, one can analyze velocity gradients in the calculated one-dimensional dynamical atmosphere model. Figure 18 shows the variation of the pulsational velocity, velocity of the optical depth surfaces, as a function of the optical depth and the phase of pulsations. For each instance in time the mean pulsational velocity was reduced in order to see variations around the mean. The line formation regions of the considered lines are lying between optical depths $\log \tau_{\text{R}} = -4 \dots 0.5$. As one can see, pulsational velocity varies in a quite narrow range $\approx -2 \dots 2 \text{ km s}^{-1}$ within the line-formation regions omitting fine structures. Around the photometric phase of $\phi_{\text{ph}} \approx 0.0 \dots 0.15$, when the expansion starts, there are small

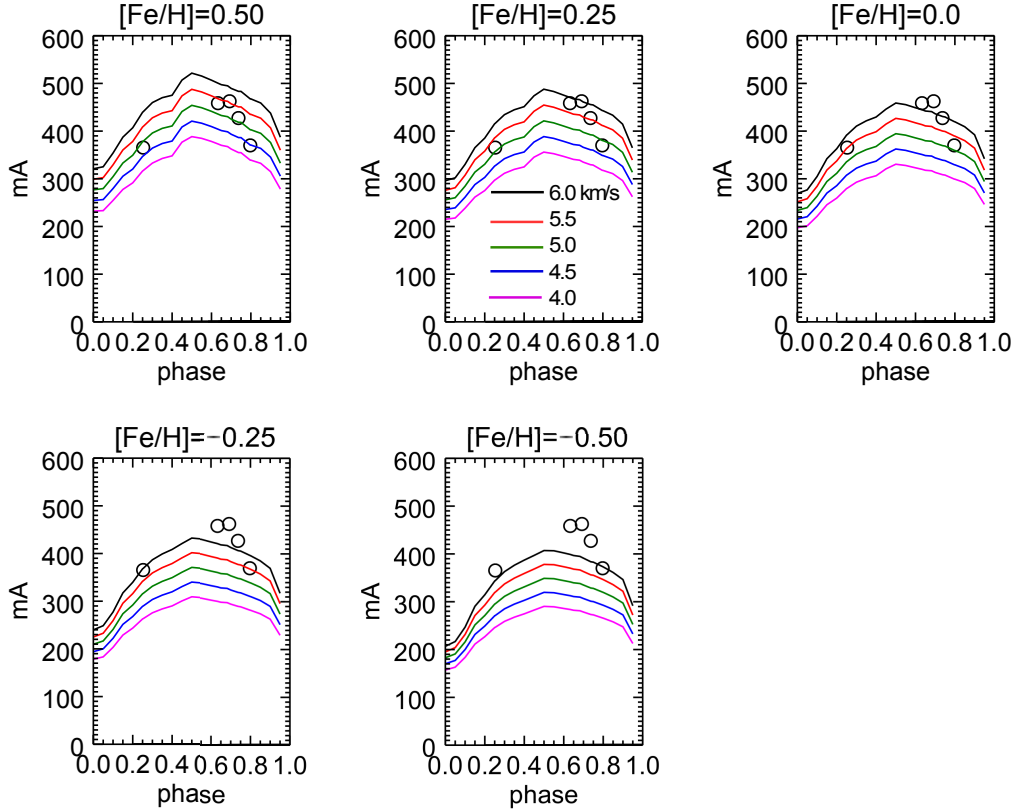


Figure 15: Theoretical and observed equivalent widths of Fe I 6065 Å lines as functions of the pulsational phase. Theoretical equivalent widths calculated for five different metallicities and microturbulent velocities. Measured equivalent widths are showed by circles.

scale propagating waves. The velocity varies in a range of $\approx -6 \dots 6 \text{ km s}^{-1}$. At the maximum of the microturbulent velocity with $\phi_{\text{ph}} \approx 0.6 - 0.7$ the model does not show strong variations of the pulsational velocity. So, one can immediately conclude, that pulsations qualitatively move the atmosphere up and down without producing strong disturbances. Velocity gradients due to pulsations can not explain the derived microturbulent velocities. The change of thermal structure of the pulsating atmosphere and, as consequence, the strong dependance of the EW on temperature can play a more important role. Microturbulence can compensate for the matches in the thermal structure between the 1D model and the star (see Chapter 4). Convection may add small scale turbulence.

2.9 Summary of the 1D modeling

I summarize the key results in this chapter concerning one-dimensional modeling of pulsating stellar atmospheres:

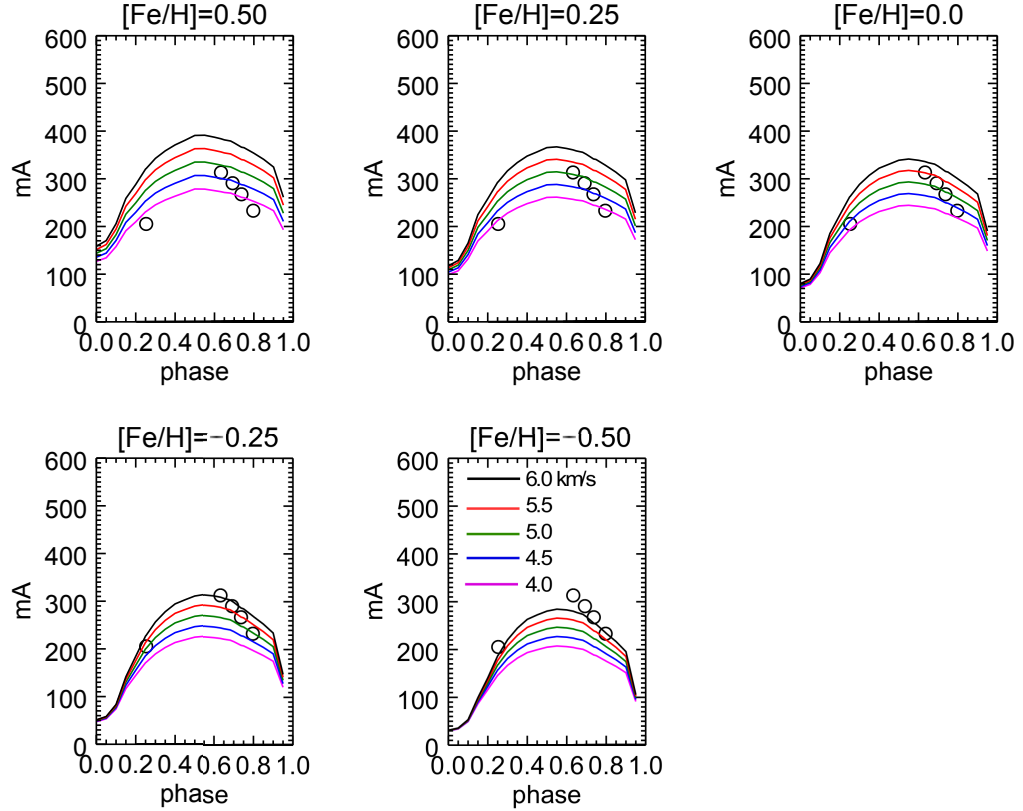


Figure 16: Theoretical and observed equivalent widths of Fe I 6151 Å lines as functions of the pulsational phase. Theoretical equivalent widths calculated for five different metallicities and microturbulent velocities. Measured equivalent widths are showed by circles.

1. I implemented the time-dependent 1D non-local theory of convection in the LHD code.
2. A dynamical 1D LHD model of Cepheid with $T_{\text{eff}} = 5000$ K, $\log g = 1.0$ dex, $[\text{Fe}/\text{H}] = 0.0$, and a period of pulsations of 34 days was calculated. The model qualitatively reproduces the asymmetry of line profiles and the shape of the light and velocity curves.
3. Velocity gradients in the line-formation regions can not explain the derived microturbulent velocities. The gradients are small with respect to the spectroscopically estimated microturbulent velocities.
4. Pulsations do not produce strong velocity gradients in line-formation regions.
5. The change of thermal structure of the pulsating atmosphere during the pulsational cycle play a more relevant role.
6. In order to investigate effects of convection one has to analyze a multidimensional Cepheid atmosphere, where convection is modeled according conservation laws without introducing additional parameters as the mixing length.

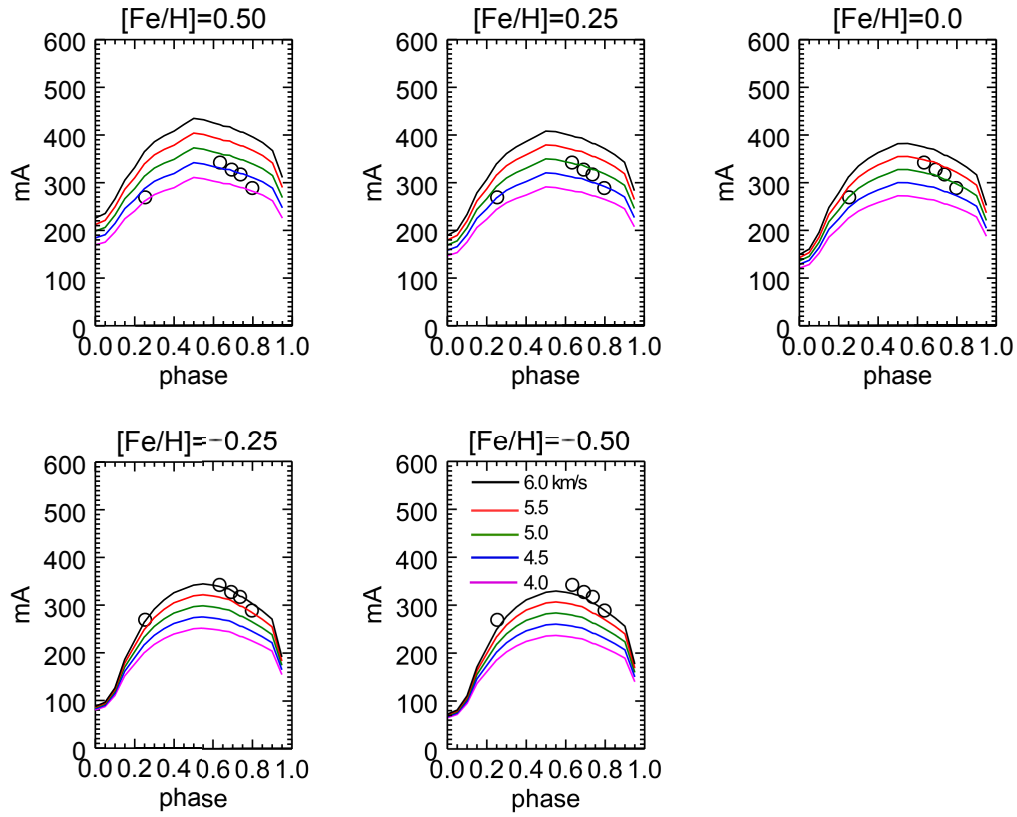


Figure 17: Theoretical and observed equivalent widths of Fe I 6750 Å lines as functions of the pulsational phase. Theoretical equivalent widths calculated for five different metallicities and microturbulent velocities. Measured equivalent widths are showed by circles.

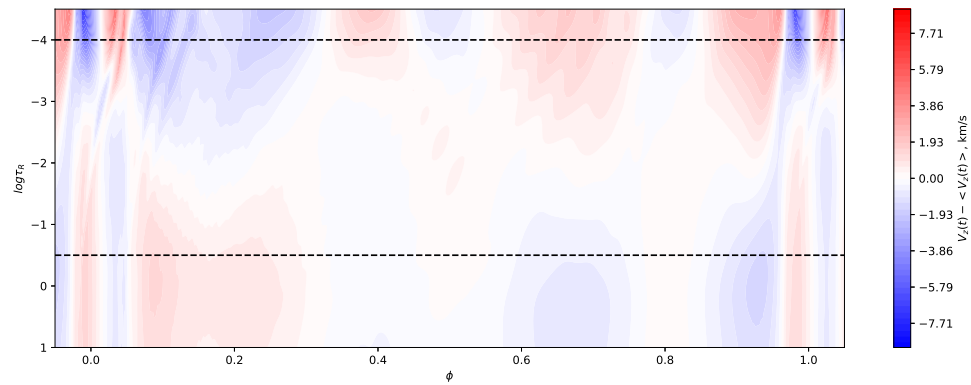


Figure 18: Radial velocity variation $V(\tau_R, t) - \langle V(\tau_R, t) \rangle_{\tau_R}$ in the Cepheid model during the pulsational cycle shown by color. The vertical axis shows the optical depth $\log \tau_R$, and the horizontal axis the pulsational phase.

3 SPECTROSCOPIC INVESTIGATION OF A 2D CEPHEID MODEL I.

Based on Vasilyev et al. (2017a).

One-dimensional pulsating stellar atmosphere models are traditionally based on the 1D theories of convection with an additional parameter characterizing the mixing length. Nobody studied the impact of convection on spectroscopic properties of pulsating stars based on the 2D and 3D pulsating stellar atmosphere models, where convection is included from the first principles. Calculation of the multidimensional Cepheid envelope models is a sizable computational problem due to the presence of different spatial and temporal scales. However, Mundprecht et al. (2013, 2015) performed hydrodynamic simulations of 2D Cepheid envelopes focusing on properties of convective regions and on the interaction between pulsations and convection. Freytag et al. (2017) used the CO5BOLD radiation-hydrodynamics code to produce an exploratory grid of global 3D "star-in-a-box" models of the outer convective envelope and the inner atmosphere of AGB stars to study convection, pulsations, and shock waves as well as the dependence of these parameters on stellar and numerical parameters. For these stars with low-effective temperatures and gravitational accelerations, the lifetime of convective cells is comparable to the pulsational time-scale, which makes it possible to model pulsations, though the spatial resolution is not high enough for detailed spectral synthesis.

In the next two chapters, I present original work of the spectroscopic investigation of a 2D envelope model of a Cepheid-like variable where the non-local and time-dependent nature of convection is included from first principles. The model was calculated by Dr. Bernd Freytag from Department of Physics and Astronomy at Uppsala University, who has been working painstakingly for several years on this simulation. I performed detailed spectroscopic investigations of the 2D model, from which the results will be discussed in this chapter and the next. They are based on two my first author paper, Vasilyev et al. (2017a,b). Specifically, I demonstrate in this chapter that the model is able to capture relevant features of the Cepheid physics despite the employed approximations, such as plane-parallel geometry with the constant surface gravity and grey radiative transfer. In Section 3.1 I describe the model, in Section 3.2 I study its spectroscopic properties. In more detail, I derive the microturbulent velocity from the 2D model and report on the methodology behind its derivation, and additionally I describe the behavior of the line equivalent widths and asymmetries. In Section 3.3, I discuss line shifts, and give an interpretation of the residual spectroscopic line-of-sight radial velocity. A derivation of the projection factor (p -factor), which is a key parameter in the Baade-Wesselink method of the distance determination to Cepheids, is discussed in Section 3.4. Finally, I summarize the results in Section 3.5.

3.1 Description of the 2D Cepheid model

Radiation-hydrodynamics simulations of a short-periodic Cepheid-like variable employing grey radiative transfer were calculated with the CO5BOLD code (Freytag et al., 2012) in 2D Cartesian geometry. The models gt56g20n01 to gt56g20n04 have a nominal effective temperature of $T_{\text{eff}} = 5600$ K, and a constant depth-independent gravitational acceleration of $\log g = 2$. The pulsation period of the Cepheid model comes out to ≈ 2.8 days. The simulations use an equidistant spatial grid of $N_x \times N_z = 600 \times 500$ (model gt56g20n01) to 580 (gt56g20n04) points along the horizontal and vertical direction, respectively. The corresponding geometrical size of the largest model is $l_x \times l_z = 1.12 \cdot 10^{12}$ cm \times $5.4 \cdot 10^{11}$ cm. The size of the grid cells is $1.88 \cdot 10^9$ cm \times $9.38 \cdot 10^8$ cm. For the flow, impenetrable boundaries are imposed at the top and bottom of the domain; the side boundaries are periodic. A radiative flux according to the nominal effective temperature is prescribed at the bottom. Radiation can pass unimpeded through the top of the modelled box. The chemical composition of the model is close to solar. Specifically, the hydrogen abundance is $\log \epsilon_{\text{H}} = 12.0$, helium abundance $\log \epsilon_{\text{He}} = 11.0$, silicon abundance $\log \epsilon_{\text{Si}} = 7.5$, and iron abundance $\log \epsilon_{\text{Fe}} = 7.46$.

Figure 19 depicts images of entropy, temperature, pressure, density, and He II ionization fraction at an instance in time during the expansion phase as a function of geometrical coordinates. Convection produces horizontal inhomogeneities so that surfaces of constant optical depth are not flat. The pulsating model exhibits strong shocks. Low density gas is falling down from above and collides with expanding photospheric and sub-photospheric material. At the so-formed accretion front, density and pressure jump by up to three orders of magnitude. We checked that such jumps cannot be simply understood as the result of the Rankine–Hugoniot (adiabatic) shock conditions but further factors must play a role. As evident from the lines of constant optical depth, line formation typically takes place in the region between the accretion front and optical depth unity.

We emphasize that the construction of the model was a numerical challenge. The largest obstacle is the extremely small numerical time step imposed by the short radiative relaxation time on a time-explicit scheme (for a detailed discussion, see Mundprecht et al., 2013). It enforces the restriction to 2D models, at the moment. In addition, strong pulsations can tend to cause an imbalance between mass in- and outflow resulting in a net time-averaged mass flow across the top boundary. To avoid it, the closed top boundary was chosen. However, the closed top boundary enhances strong artificial velocity gradients close to the boundary. To decrease the influence of them on dynamics of optically thin regions, we applied an artificial drag force in a number of grid layers close to the top, reducing the velocities by a certain fraction per time interval. This numerical approach impacts on the dynamics of the line formation regions of strong lines, which like the Ca triplet form at the outer atmosphere near the chromosphere. To avoid the impact of boundary effects we consider lines that are forming deeper in the range $\log \tau_{\text{R}} = -3 \dots 0$.

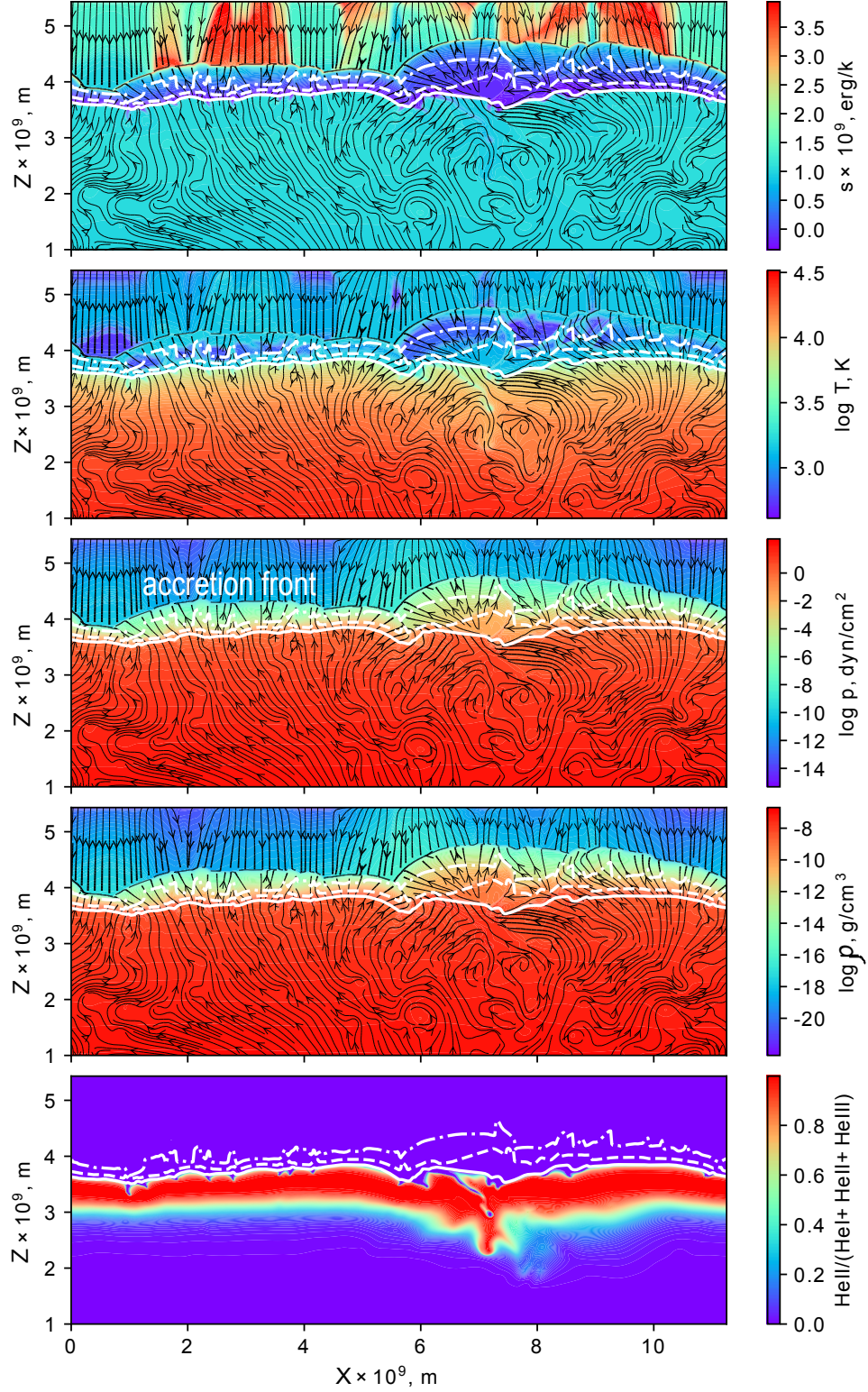


Figure 19: Entropy (top panel), temperature, pressure, density, and He II ionization fraction $n_{\text{He II}}/(n_{\text{He I}} + n_{\text{He II}} + n_{\text{He III}})$ (bottom panel) as function of the horizontal and vertical coordinates at time $t = 1.40 \times 10^7$ s, which corresponds to an expanding phase. Pseudo-streamlines are shown as black solid lines. Surfaces of constant Rosseland optical depth are shown by white lines: $\tau_{\text{R}} = 1$ (solid line), $\tau_{\text{R}} = 10^{-2}$ (dashed line), $\tau_{\text{R}} = 10^{-4}$ (dashed-dotted line).

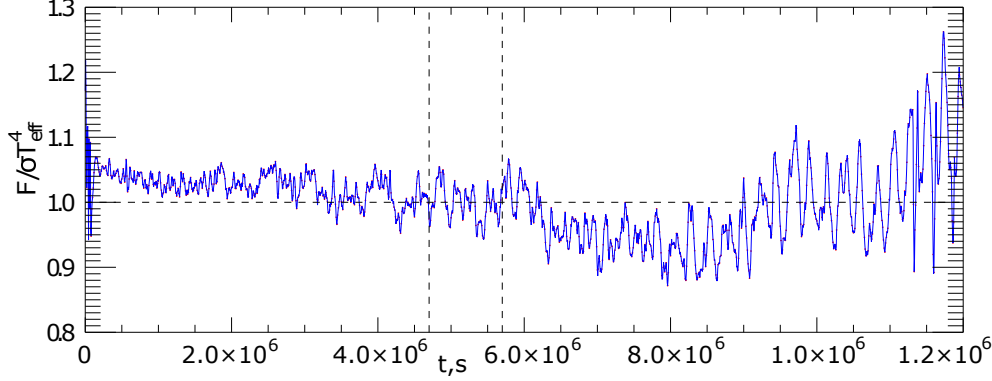


Figure 20: Initial evolution in time of the bolometric flux of the model. Pulsations set in at $t \approx 10^6$ s. Dotted lines indicate the time interval without pulsations for which spectral synthesis calculations were performed.

The model shows self-excited fundamental mode pulsations starting from initially plane-parallel static conditions (adding random small amplitude disturbances to break the symmetry). The initial evolution in time of the bolometric flux of the model is shown in Fig. 20. Pulsations set in at around $\approx 6 \times 10^6$ s. They are excited by the κ -mechanism (Eddington, 1917; Zhevakin, 1963). In particular, around 4 % of the radiative flux σT_{eff}^4 is spent to ionize hydrogen, which is fully ionized for Rosseland optical depth $\tau_R > 1$, due to the steep temperature gradient, and is largely neutral for $\tau_R < 1$. The main driver of pulsations is the region of singly ionized helium (see bottom panel in Fig. 19). The thickness of the He II ionization zone varies; He II ionization stores and releases 16 % of the radiative energy passing the layer during a pulsational cycle.

Before pulsations have set in, the flow evolution is mostly governed by convection. Regions with up- and down-flows at the photosphere affect the outgoing radiation field. The spatio-temporal evolution of the emergent intensity (in vertical direction, $\mu = 1$) when pulsations have not set in is shown in the top panel of Fig. 21. The intensity map exhibits a typical convective pattern. In particular, convection generates a few large-scale down-flows, which exist for long timescales $> 10^6$ s. Smaller-scale down-flows of cooled gas have a tendency to get “sucked” into the dominant larger-scale flows. Down-flows correlate with lower intensities, the bluer regions in Fig. 21.

The intensity map for later phases when pulsations have set in is shown in the bottom panel of Fig. 21. The convective pattern now consists of a dominant large-scale down-flow in the right part of the intensity map, and small-scale flows that evolve independently. For the given atmospheric parameters and assuming a mass of roughly $5 M_{\odot}$, one can expect around 300 granulation cells on the visible hemisphere. The mass was motivated from inspection of the PADova and TRIeste Stellar Evolution Code (PARSEC) evolutionary tracks (Bressan et al., 2012).

The phase of maximum compression roughly coincides with the phase of maximum brightness (see also Fig. 22). Maximum brightness is not reached at exactly the same time at all locations but depends slightly on the morphology of the convective surface flow. For instance, in the large

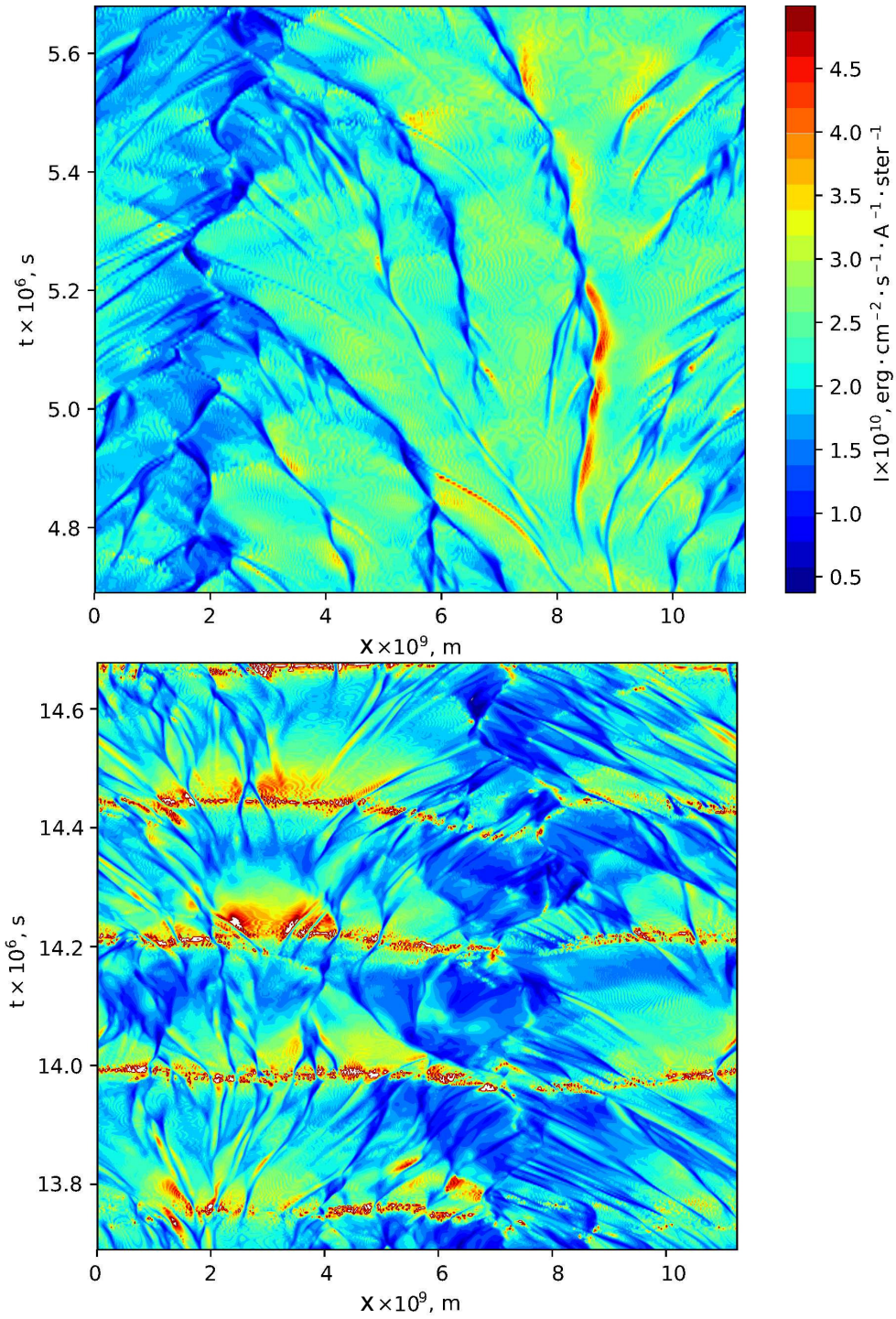


Figure 21: Spatio-temporal evolution of the emergent intensity directed in vertical direction ($\mu = 1$). The upper panel shows a time interval when pulsations have not set in (model gt56g20n01), the bottom panel a time interval with fully developed pulsations (model gt56g20n04). Time, spatial, and colour scales are identical for both panels.

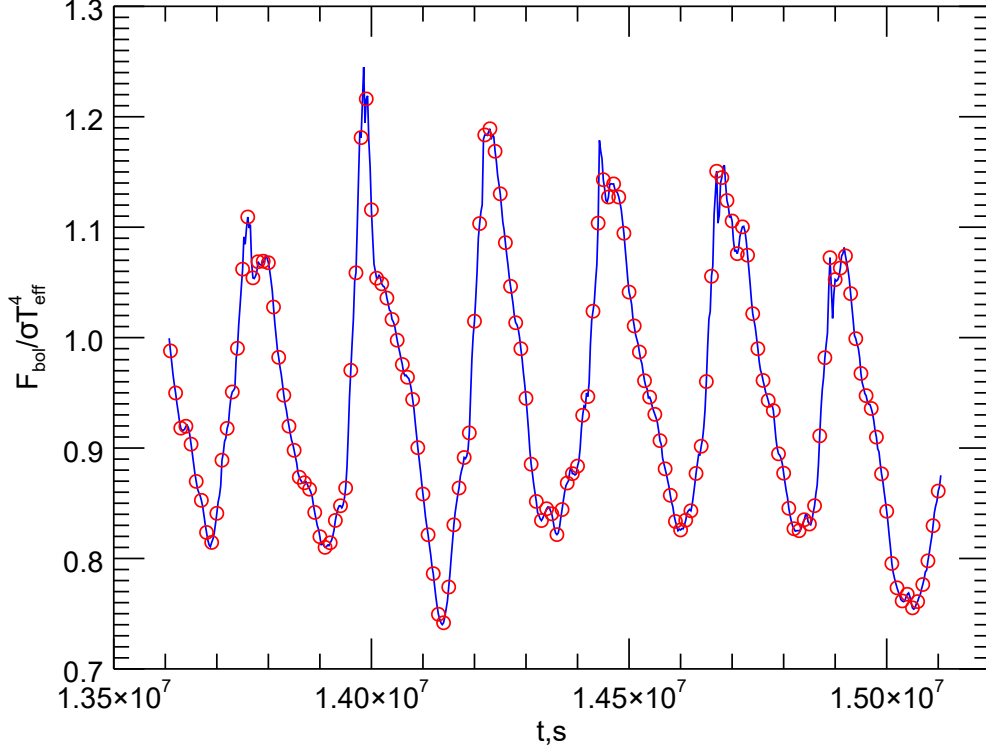


Figure 22: Model light curve in terms of the emergent bolometric flux. Red circles mark the instances in time for which a spectral synthesis was performed.

down-flow maximum brightness is reached slightly earlier than in the neighbouring regions. This illustrates the impact of horizontal inhomogeneities on the pulsations.

Preferentially during phases of maximum brightness, which almost coincide with the maximum compression, convective down-flows are generated. This is a sign of the action of the convective instability. The efficiency of convection depends on the gravitational acceleration g_0 , and the growth timescale of the convective instability τ_{conv} is proportional $\tau_{\text{conv}} \sim 1/\omega_{\text{BV}} \sim \sqrt{1/g_0}$, where ω_{BV} is the Brunt–Väisälä frequency. The time evolution of the acceleration a of a pseudo-Lagrangian mass element following the mean vertical mass motion close to the photosphere is shown in Fig. 23. The model itself is based on an Eulerian description of the flow field from which one can transform to a pseudo-Lagrangian reference frame. During the reversal of the direction of motion at the phase of maximum compression, a photospheric pseudo-Lagrangian mass element experiences an acceleration of $\approx (1.0 \dots 2.5)g_0$. In total it experiences an effective acceleration of $g_{\text{eff}} = a + g_0 \approx (2.0 \dots 3.5)g_0$, which amplifies the convective instability and also leads to high convective velocities. One can see in Fig. 23 that the turbulent pressure p_t adds a significant contribution to the total pressure gradient, which is equal to the effective gravity: $-\nabla(p_{\text{gas}} + p_t)/\rho = a + g_0$.

A 1D mean model, which is the result of horizontal averaging of the full 2D model at fixed geomet-

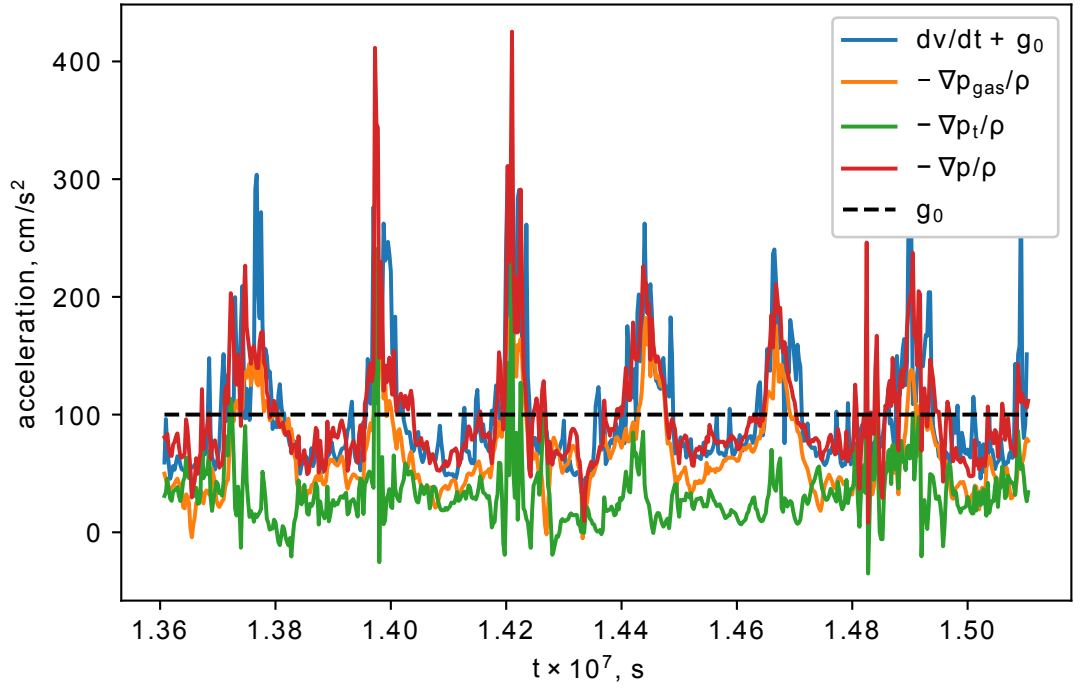


Figure 23: The total acceleration $dv/dt + g_0$ experienced by a (Lagrangian) mass element close to optical depth unity as a function of time, where g_0 is the constant gravitational acceleration. Coloured lines show the contributions to the pressure gradient by the gas pressure p_{gas} , and turbulent pressure p_t , as well as the resulting sum $p = p_{\text{gas}} + p_t$ balanced by the total acceleration.

rical height, was used to analyze the pulsational velocity and radiation flux. The radial velocity curve of a layer with the Rosseland optical depth $\tau_R = 2/3$ shown in Fig. 24 was calculated by cubic spline interpolation of the vertical velocity component of the mean 1D model. The amplitude of the radial velocity is $V \approx 20 \text{ km s}^{-1}$, which is quite typical for a Cepheid (Groenewegen, 2013). The non-zero mean vertical velocity of the optical surface is the consequence of the presence of convective fluctuations, large amplitudes of pulsations and a non-linearity of opacities as a function of the temperature. A word on sign conventions: in the CO⁵BOLD simulations the vertical axis is directed toward the observer so that a positive vertical velocity corresponds to a blueshift. However, normally the spectroscopic convention for the radial velocity is used in this work, where a blueshift corresponds to a negative velocity.

A light curve in terms of the bolometric flux is shown in Fig. 22. Red circles mark instances in time for which a spectral synthesis was performed with Linfor3D⁵ (Gallagher et al., 2016). The light curve covers a time interval with fully developed pulsations covering six periods. For each 2D snapshot, Linfor3D solves the radiative transfer equation along three inclined angles for two azimuthal angles, which are lying in the xz -plane, and along the vertical direction. To accelerate

⁵<http://www.aip.de/Members/msteffen/linfor3d/>.

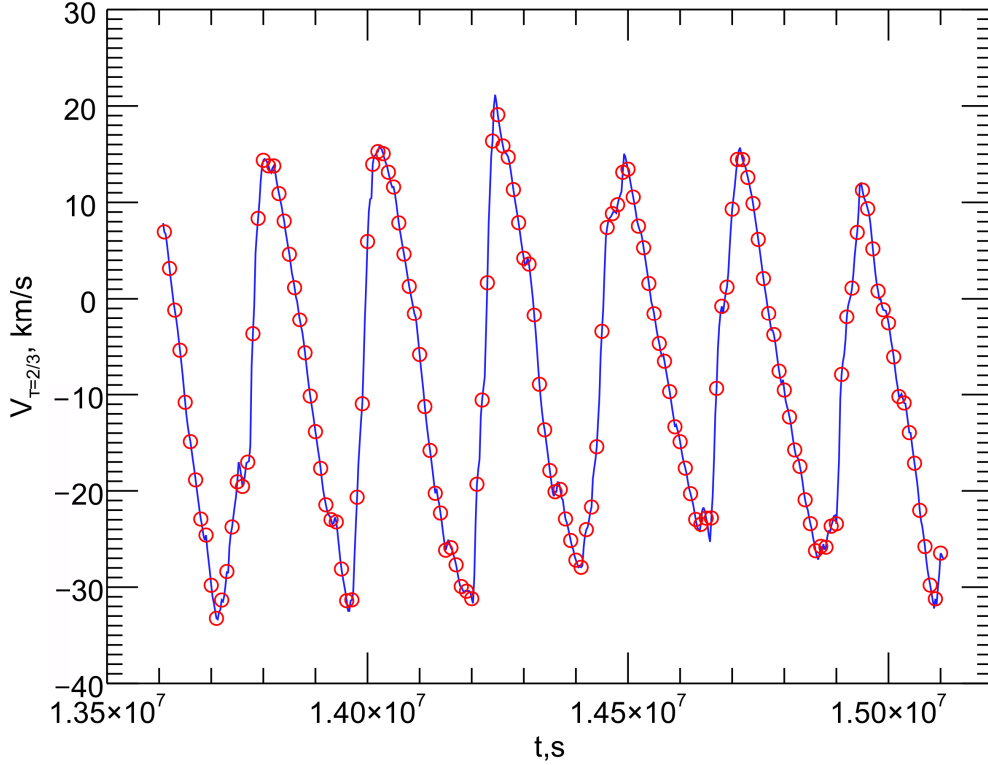


Figure 24: Vertical (radial) velocity of a layer at fixed Rosseland optical depth $\tau_R = 2/3$. Here, a positive velocity corresponds to a blueshift.

the spectral synthesis one can sub-sample the model structure along the x -axis. Tests taking each and every third grid point along the x -axis were performed for a line Fe I $\lambda 6003 \text{ \AA}$. Equivalent widths for these cases come out very similar: $W_{\Delta n_x=1} = 109.8 \text{ m\AA}$ and $W_{\Delta n_x=3} = 111.2 \text{ m\AA}$. Due to the similarity, the computationally less demanding sub-sampled case is used in this paper.

3.1.1 Convective noise

Observed light and radial velocity curves of Cepheids are typically smooth, and show a high degree of similarity from cycle to cycle. The model light curve in Fig. 22 and the radial velocity curve in Fig. 24 do not at all exhibit these properties. Amplitude and shape of the curves change significantly during the pulsations. This is the result of convection, which adds statistical fluctuations to the velocity and thermal structure of the model. The fluctuations in the pressure gradients shown in Fig. 23 are a clear illustration of this “convective noise”. The convective noise appears so prominent in our light and velocity curves since our model represents only a small part of the surface of a Cepheid. The fluctuations would decrease if we increased the spatial extent of the model, or could take recourse to many realizations of the stellar surface with independent convective but coherent pulsational properties. However, both options would demand prohibitively expensive additional simulations. In the following we try to mitigate the effects of the fairly low resulting signal-to-noise

ratio by adequate procedures when extracting simulation properties. As a side, we note that the cycle-to-cycle variations in Cepheids recently reported by Anderson (2016) might be an imprint of the residual convective noise after averaging over the full stellar disk. However, it is difficult to extrapolate the convective noise properties of our calculated model to a long-period Cepheid. According to the period-mean gravity relation (Gough et al., 1965), it requires approximately a factor of ten lower gravitational acceleration for a 35-day pulsation period, which changes the convective timescale, velocities, characteristic sizes, and lifetimes of convective cells.

3.1.2 Effects of the Cartesian geometry and grey radiative transfer

Our Cepheid model has Cartesian geometry while the structure of a real Cepheid is more accurately represented by a spherical geometry. We want to estimate the impact of the Cartesian geometry here.

In Cepheids the radius changes due to the pulsations are of the order of $\approx 10\%$, which corresponds to a change in the stellar volume of $(\frac{\Delta V}{V})_s = 3 \frac{\Delta R}{R} = 0.3$, where the subscript s indicates a spherical geometry. For the planar (subscript p) geometry adopted here, the change is $(\frac{\Delta V}{V})_p = \frac{\Delta R}{R} = 0.1$. For adiabatic pulsations, there is a corresponding difference of the temperature change $\Delta \frac{\Delta T}{T} = \left[(\frac{\Delta V}{V})_s - (\frac{\Delta V}{V})_p \right] \cdot (\gamma_{\text{ad}} - 1) = 0.2 \cdot (\gamma_{\text{ad}} - 1)$, where γ_{ad} is the adiabatic exponent, which is equal to $5/3$ for an ideal monatomic gas. One would arrive at the same conclusion if one considered an atmosphere with a fixed thickness during the pulsations. Hence, the different geometry leads to a temperature difference of $\approx 13\%$. This is significant, and eventually means noticeable changes in the conditions for line formation. However, as we will see in a moment, the temperature does not follow adiabatic changes but is rather controlled by radiation. Radiative properties differ less between the geometries since the thickness of the atmosphere is still rather small in a Cepheid – significantly less than its radius change during the pulsational cycle.

One can argue that using grey radiative transfer in the model is far from realistic and may lead to different qualitative changes of the thermal structure during the pulsations in comparison to the case of frequency-dependent (non-grey) radiative transfer. Especially the characteristic timescale of radiative relaxation, which is defined as the time for reaching radiative equilibrium conditions in the atmosphere, depends on the opacity treatment. To derive characteristic timescales we follow Ludwig et al. (2002). With the assumption that the geometrical size of a thermal disturbance is equal to the local pressure scale height, the radiative relaxation timescale in Eddington approximation can be written as:

$$t_{\text{rad}} = \frac{c_p}{16\sigma\chi T^3} \left(1 + \frac{3}{4\pi^2} \tau_{\text{dis}}^2 \right), \quad (123)$$

where c_p denotes the specific heat at constant pressure, σ Stefan-Boltzmann's constant, χ the Rosseland opacity, and $\tau_{\text{dis}} = \chi \rho H_p$ the optical size of the assumed temperature disturbance.

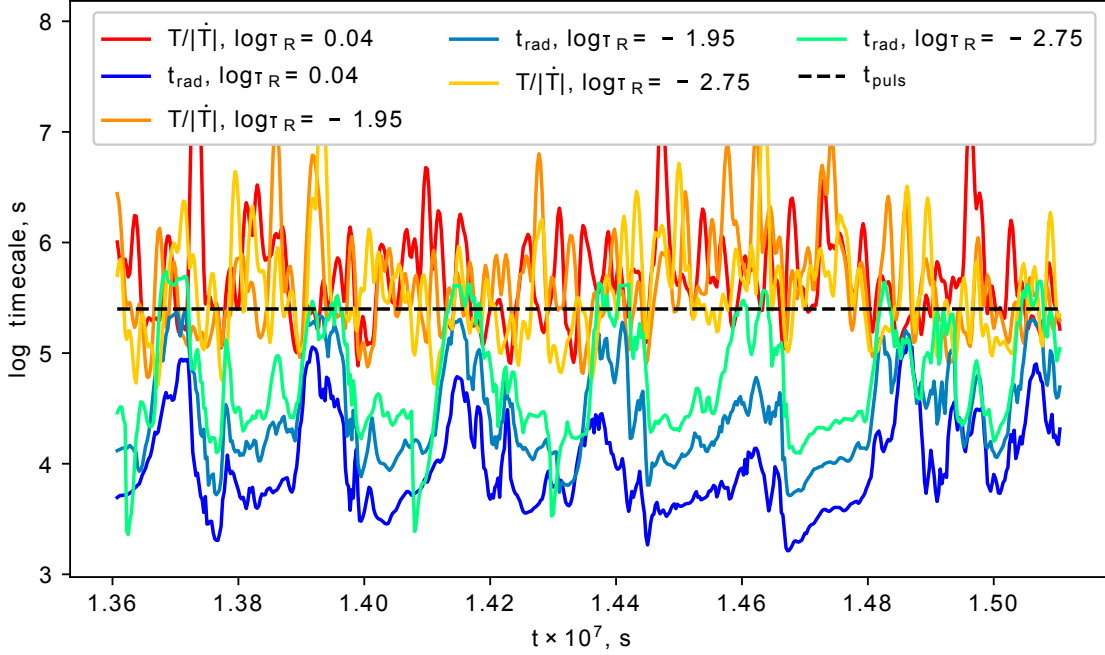


Figure 25: Comparison of the characteristic radiative relaxation time and the actual timescales on which temperature changes happen for three Lagrangian mass elements in the atmosphere. The elements are located in the line formation region at time-averaged optical depths $\log \tau_R = 0.04, -1.95, -2.75$.

The actual characteristic time of change of the temperature t_T of a mass element in the atmosphere model can be calculated as

$$t_T = \frac{T}{|dT/dt|}, \quad (124)$$

where dT/dt is a rate of the temperature change. This timescale depends on local fluctuations of the temperature due to the presence of disturbances generated by convection or pulsations. The pulsational period t_{puls} characterizes the global change of the thermal structure during the pulsations.

Figure 25 shows the timescales as a function of time for three Lagrangian mass elements in the atmosphere, which are lying in the line formation region with time-averaged optical depths $\log \tau_R = 0.04, -1.95, -2.75$. The properties of the mass elements were calculated from the 1D mean model. The radiative relaxation timescale is shorter than both the pulsational period and the characteristic time of the temperature change in the line formation regions, except in phases of maximum compression, during which for the highest parts of formation regions the timescale is comparable with the period of pulsations. One can see that the characteristic time of change of the temperature does not depend much on the optical depth for the line formation region and it has the same order as the pulsational period. The radiative timescales have been evaluated under simplifying assumptions, and should therefore be taken as order of magnitude estimates only. Our choice of the disturbance size is rough. One might argue that the size of horizontal

disturbances generated by convection is a more appropriate length scale, and typically amounts to a few pressure scale heights. Even with $10H_p$, t_{rad} does not change much since the optical depth is already quite low (in the optically thin limit the radiative timescale is independent of the size of the disturbance). We conclude that radiation is able to keep the temperature structure close to radiative equilibrium – consistent with actual modelling results for the line formation region. For non-grey radiative transfer, the radiative timescale is shorter (see e.g. Ludwig et al., 2002). The stronger coupling between radiation and matter in the non-grey case would maintain radiative equilibrium conditions even more effectively. However, since the grey radiative transfer is already capable of doing so, the main difference to the non-grey case would be the lack of line blanketing and back warming, which is rather modest. One also expects in the non-grey case smaller temperature fluctuations in the photosphere, and the mean temperature gradient might be steeper. We conclude that our 2D Cartesian model provides fairly realistic estimates of the thermal conditions in the line formation region.

3.1.3 Relating velocity and luminosity amplitudes

Kjeldsen and Bedding (1995) derived a universal relation between the luminosity $(\delta L/L)_{\text{bol}}$ and velocity v_{osc} amplitudes of oscillations for many classes of oscillating stars using linear theory and observational data:

$$(\delta L/L)_{\text{bol}} \sim \frac{v_{\text{osc}}}{T_{\text{eff}}}. \quad (125)$$

The relation was calibrated using β and δ Cephei, δ Scuti, and RR Lyrae stars. For a given T_{eff} and v_{osc} , one can predict the luminosity amplitude $(\delta L/L)_{\text{pred}}$ and compare it with the observed luminosity amplitude. For the 2D Cepheid model, the predicted luminosity amplitude $(\delta L/L)_{\text{pred}} \approx 0.375$ for the $v_{\text{osc}} \approx 20 \text{ km s}^{-1}$ and $T_{\text{eff}} = 5600 \text{ K}$. The "observed" luminosity amplitude of the model is ≈ 0.35 . Both of them are in good agreement with the result of Kjeldsen and Bedding (1995) within the 1σ scatter.

3.2 Spectroscopic properties

Spectral properties are directly accessible to observation, and we want to characterize our model in terms of its spectroscopic characteristics. Microturbulence is an important "side parameter" in a standard spectroscopic analysis. Gillet et al. (1999) derived the microturbulence velocity curve of δ Cep using 1D non-linear non-adiabatic pulsating models. Perhaps not surprisingly, the microturbulent velocity turns out to change with pulsational phase. Here we attempt a first pilot study of the microturbulence derived from a multi-dimensional Cepheid model.

3.2.1 Microturbulence

Our estimate of the microturbulent velocity is based on the method described in Steffen et al. (2013). The procedure is as follows: For a spectral line, a spectral synthesis is performed using the 2D thermal structure with different velocity fields: (i) using the original 2D velocity field ν_{2D} , and (ii) replacing the 2D hydrodynamic velocity field with an isotropic, depth independent microturbulent velocity ξ_{mic} as in a case of classical 1D spectral synthesis. The microturbulent velocity for the considered spectral line at each instance in time is defined by the requirement $EW(\nu_{2D}) = EW(\xi_{mic})$. In practice, we calculated $EW(\xi_{mic})$ for a small grid of ξ_{mic} and interpolated in this grid to the desired $EW(\nu_{2D})$. This method allows us to determine a microturbulent velocity for each individual line. It is clear that it differs from the classical procedure where one considers a set of weak and strong lines. However, besides having the virtue of being able to assign a microturbulence to a single line, the procedure applied here is perhaps the cleanest possible way to derive a microturbulence if one wants to actually associate the microturbulence with a velocity field providing the non-thermal line broadening.

A set of fictitious neutral and singly ionized iron lines with fixed wavelength $\lambda = 5500 \text{ \AA}$ but different line strengths and excitation potentials was used to conduct a systematic survey of the microturbulent velocity as a function of time. The excitation energies for Fe I lines were $E_i = 1, 3, 5 \text{ eV}$; for Fe II they were $E_i = 1, 3, 5, 10 \text{ eV}$. Oscillator strengths were chosen for each excitation energy E_i so as to cover a range of equivalent widths from 10 m\AA to 130 m\AA in steps of 20 m\AA for the initial instance in time at step (i).

Based on the 2D model, equivalent widths (EWs) for a set of Fe I and Fe II lines as a function of time in step (i) are shown in Figs. 26 and 27. Both groups of these lines, Fe I and Fe II, show a modulation of the equivalent width with pulsational phase for both strong and weak lines. The amplitude of the EW variation is bigger for Fe I than for Fe II, for the same initial line strengths. Lines of the Fe I and Fe II with bigger line strength have higher amplitude of the variation of EWs. The overall behaviour can be directly understood from the different temperature sensitivities of the lines in the two different ionization stages. Besides a roughly periodic variation of the equivalent widths, there is a stochastic component stemming from the convective noise in the model.

For step (ii), the spectral synthesis was calculated using a depth-independent isotropic Gaussian microturbulent velocity in the range $\xi_{mic} = 0.5 - 6.0 \text{ km s}^{-1}$ to cover the range usually found in studies of Cepheids (Andrievsky et al., 2002c; Luck et al., 1998). A plot with the result of the spectral synthesis of the Fe I $\lambda 5500 \text{ \AA}$ with $\xi_{mic} = 3 \text{ km s}^{-1}$ is shown in Fig. 28. The increase of the microturbulent velocity leads to an increase of the EW. Strong lines are very sensitive to variations of the microturbulence.

The calculation of ξ_{mic} by the requirement $EW(\nu_{2D}) = EW(\xi_{mic})$ was done with a third order spline interpolation. The microturbulence as a function of time for Fe I and Fe II lines is shown in Figs. 29

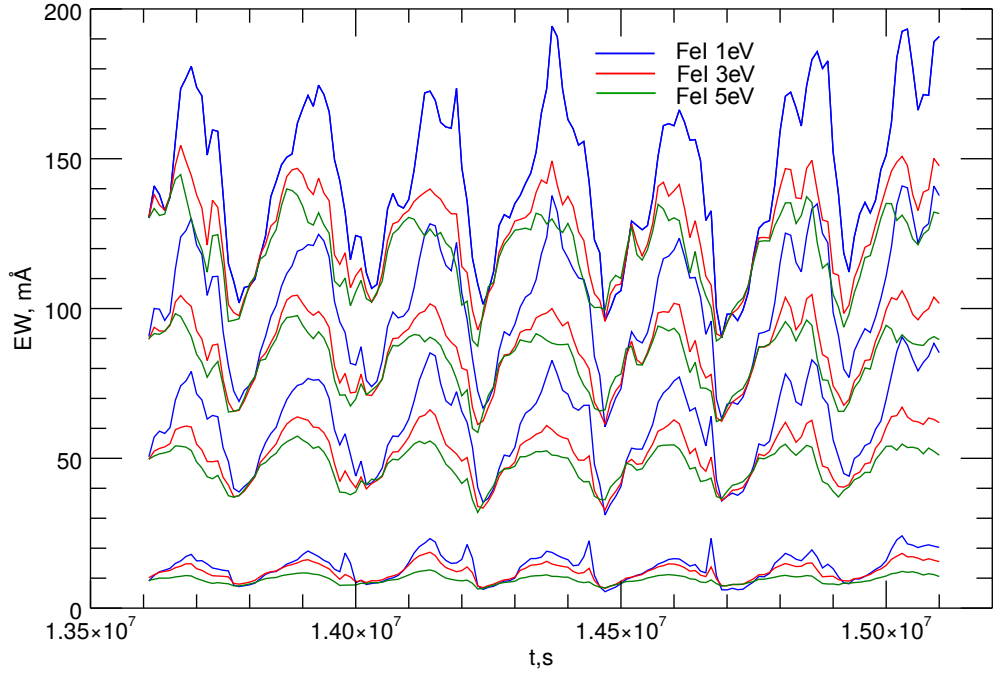


Figure 26: Equivalent widths obtained from the 2D model as a function of time for lines of Fe I $\lambda 5500 \text{ \AA}$ with excitation energies of $E_i = 1, 3, 5 \text{ eV}$ (coloured solid lines). Different oscillator strengths were used for each excitation energy to cover a range of equivalent widths from 10 mÅ to 130 mÅ at starting time, as apparent by the four groups of three lines each.

and 30. We note that the calculated synthetic spectra have infinite resolution and signal-to-noise, which allows us to assign a microturbulence even to the weakest lines of our sample. The microturbulence exhibits a clear modulation with the pulsational phase with an amplitude of $\approx 0.5 \dots 1.0 \text{ km s}^{-1}$ and a certain degree of randomness due to convection. Around photometric phase 0.9 before maximum light the microturbulent velocity curve exhibits distinct peaks. These peaks coincide with the moment when the model is near its minimum radius. This is qualitatively in agreement with the temporal behaviour of turbulent velocities as measured by Borra and Deschatelets (2017) using an autocorrelation technique. One has to keep in mind that their turbulent velocities include contributions from rotation as well as macro- and microturbulence. The absolute value of the microturbulent velocity is $1.0 \dots 4.0 \text{ km s}^{-1}$, which is less than observed in short period Cepheids $\approx 1.5 \dots 5.0 \text{ km s}^{-1}$ (Andrievsky et al., 2001). The microturbulence slightly decreases with increasing excitation potential, and it averaged over all lines varies with pulsational cycle between 1.5 and 2.7 km s^{-1} .

There are several reasons why our model may fall somewhat short of the observed values: (a) our procedure to derive the microturbulence does not exactly mimic the observational procedure;

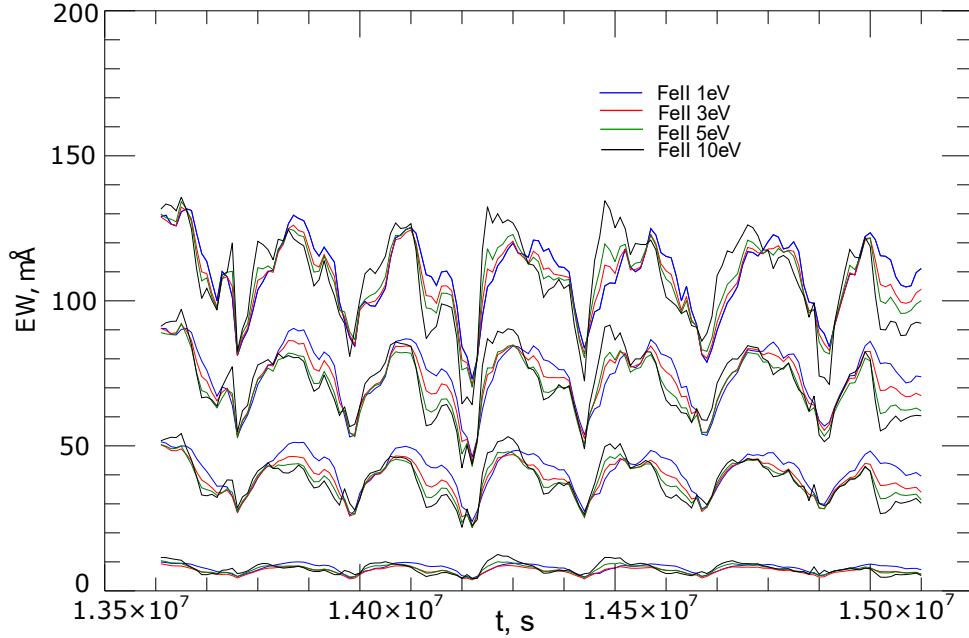


Figure 27: As Fig. 26 but for lines of Fe II $\lambda 5500 \text{ \AA}$ with $E_i = 1, 3, 5, 10 \text{ eV}$.

(b) our selection of lines differs noticeably from the set of lines used in the observations; (c) our model harbours indeed a low microturbulence. In particular, limited spatial resolution leads to a systematically low ξ_{mic} (Steffen et al., 2013). Nevertheless, we are content that at least on the whole the microturbulence in the 2D model follows the evidence from observations.

3.2.2 Spikes in the EW(t) curves

Both results of the spectral synthesis coming from step (i) with the full 2D model and step (ii) with the microturbulent velocity show that the EWs depend on the pulsational phase. The amplitude of the variation of the EW is larger for stronger lines. Occasionally, the EWs from steps (i) and (ii) show sharp spikes. This behaviour is obviously not related to the 2D velocity field, because the spikes still appear in step (ii) where the velocity field is replaced by a constant microturbulent velocity. The change of the thermal structure plays the key role here, which is illustrated in Fig. 31. At time $t = 1.466 \cdot 10^7 \text{ s}$, the equivalent width of the Fe I lines in Fig. 26 has a sharp maximum because the temperature gradient is steeper than at previous and subsequent times in the line formation region with Rosseland optical depth $\tau_R = 10^{-2} \dots 1$. The spikes of the equivalent width of the Fe I lines show up during phases of maximum compression. The EWs of the Fe II lines show additional spikes due to the deep location of the line formation regions. The impact of convection on the Fe II line formation regions is more than for similar regions of Fe I lines. Lines forming very deep might also reach into the region of the badly resolved sub-photospheric temperature jump. Unfortunately, in this important region, where convection starts, the numerical resolution is not

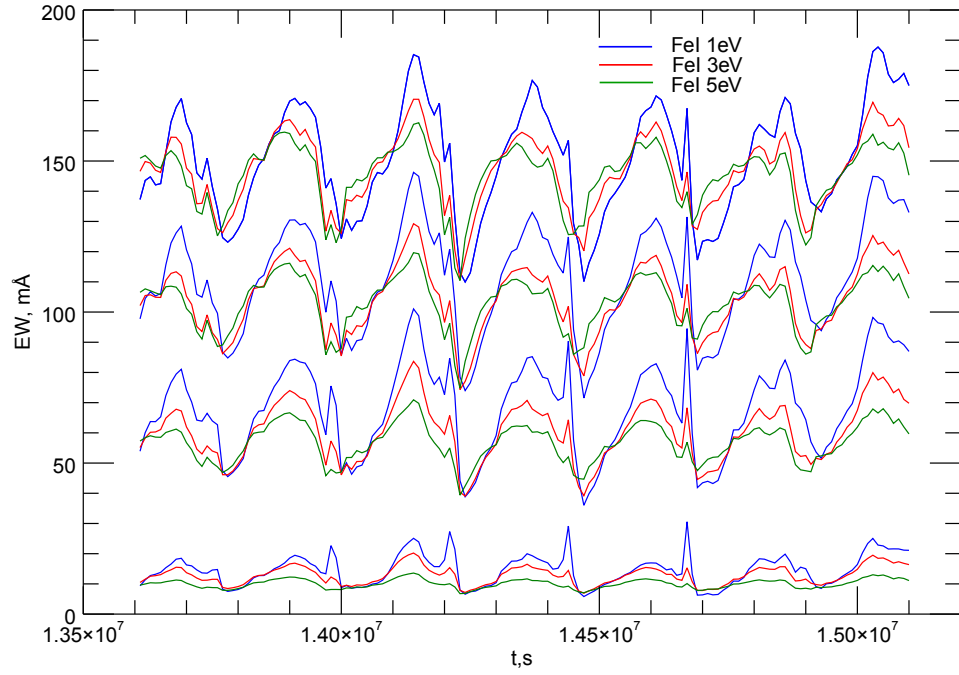


Figure 28: Equivalent widths as a function of time for lines of Fe I $\lambda 5500 \text{ \AA}$ with excitation energy $E_i = 1, 3, 5 \text{ eV}$. The EWs are calculated by replacing the 2D hydrodynamic velocity field by an isotropic, depth-independent Gaussian microturbulent velocity of $\xi_{\text{mic}} = 3 \text{ km s}^{-1}$.

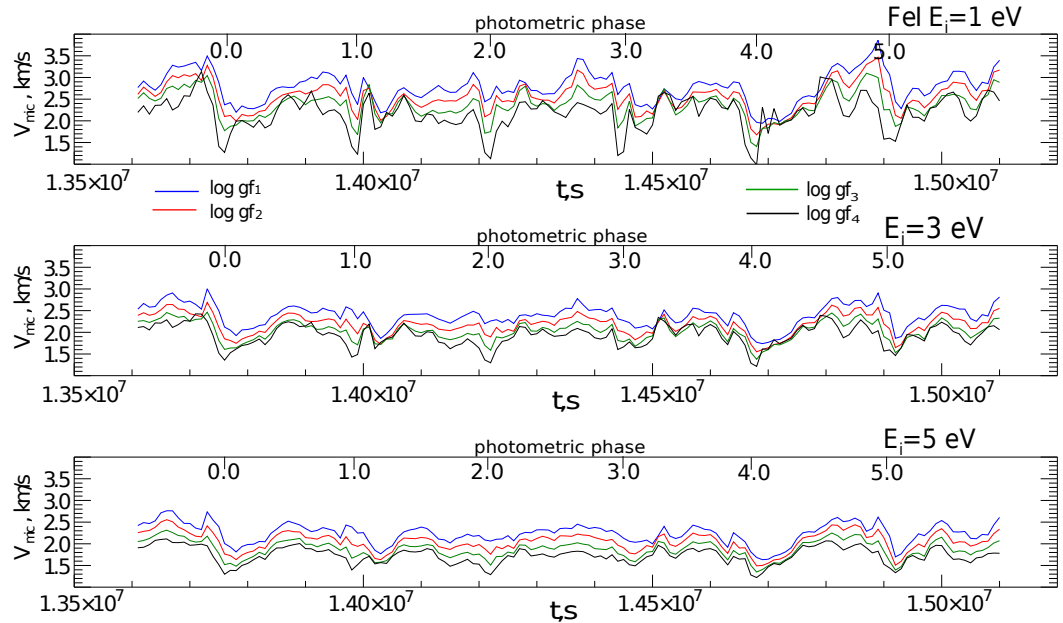


Figure 29: Microturbulent velocity V_{mic} as a function of time for lines of Fe I $\lambda 5500 \text{ \AA}$ with $E_i = 1, 3, 5 \text{ eV}$. $\log gf_1$ (strongest line) $> \log gf_2 > \log gf_3 > \log gf_4$ (weakest line).

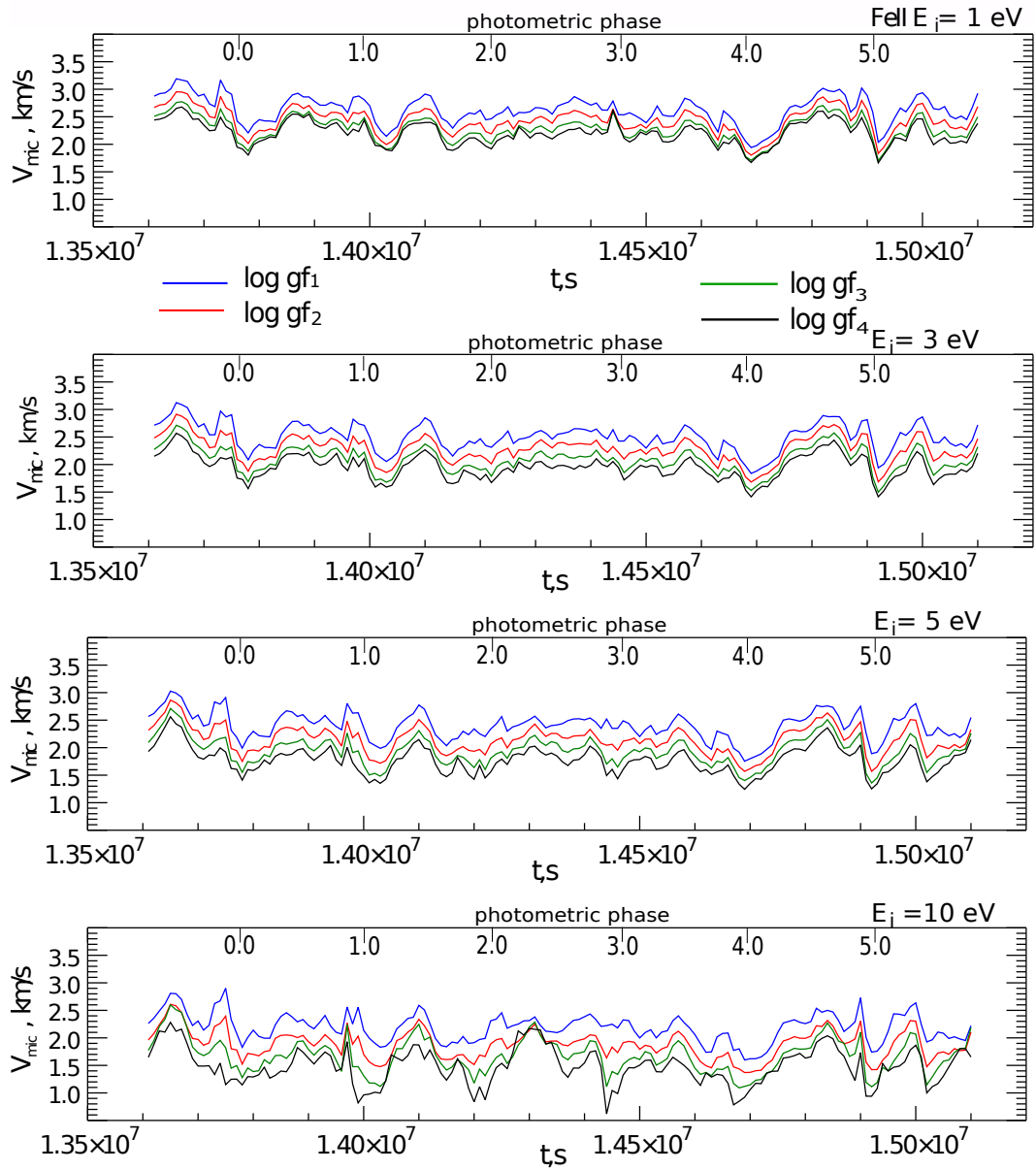


Figure 30: Like Fig. 29 but for line of Fe II $\lambda 5500 \text{ \AA}$ with $E_i = 1, 3, 5, 10 \text{ eV}$.

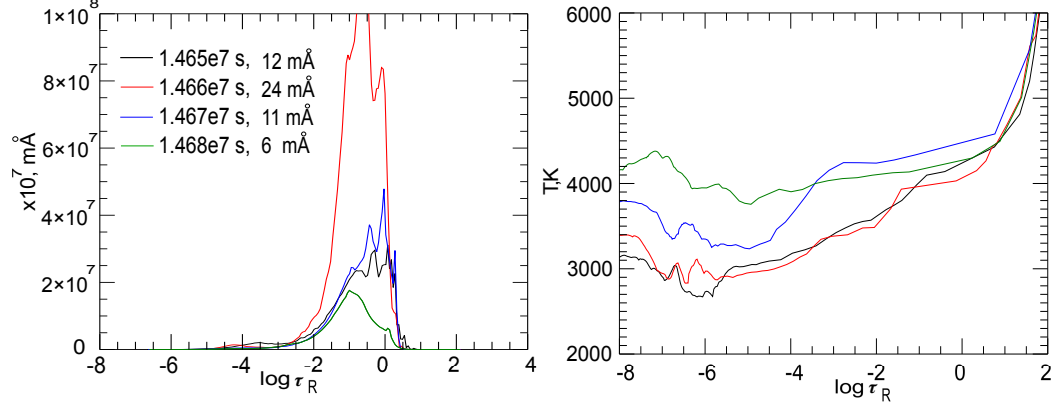


Figure 31: Time dependence of the non-normalized line equivalent width contribution functions of the weakest Fe I $\lambda 5500 \text{ \AA}$ $E_i = 1 \text{ eV}$ line (left panel) and the temperature profiles (right panel). The contribution functions and the temperature profiles for each instance in time are depicted in corresponding colours.

quite sufficient.

3.2.3 Line asymmetry

Sabbey et al. (1995) devised a method to measure the asymmetry of lines. They found that for classical Cepheids the observed line asymmetry is a function of the pulsational phase and correlates with the position of the line core. The asymmetry of a spectral line profile was determined from the difference and sum of the areas of the red and blue profile halves: $(S_{\text{red}} - S_{\text{blue}})/S_{\text{tot}}$. Two different methods were used to determine the line core position:

1. fitting a Gaussian to the whole line profile,
2. fitting a parabola to the line core below 70 % of the continuum level.

The results of the spectral syntheses show a complex multicomponent structure of the line profiles. However, we found that 30 % is a reasonable part of the line to limit systematic effects related to the complex line profile on the determination of the position of the line core. Fe I $E_i = 1 \text{ eV}$ and Fe II $E_i = 1 \text{ eV}$ line profiles for the strongest case as a function of the photometric phase are shown in Fig. 32. The photometric phase zero coincides with maximum light of the light curve. Synthetic line profiles for most phases have a multicomponent structure.

Following Sabbey et al. (1995), the line asymmetry was considered as a function of the dynamical phase ϕ_d (see Fig. 33). The dynamical phase zero coincides with the moment of the velocity reversal from contraction to expansion in the photosphere. The amplitude of the line asymmetry variation is $\approx 0.2 \dots 0.3$, which on average is larger than that found in observational data. Sabbey et al. measured the amplitude of variations of the line asymmetry to $\approx 0.1 \dots 0.3$. Nevertheless, the time dependence of the line asymmetry has the same behaviour for the model and observations

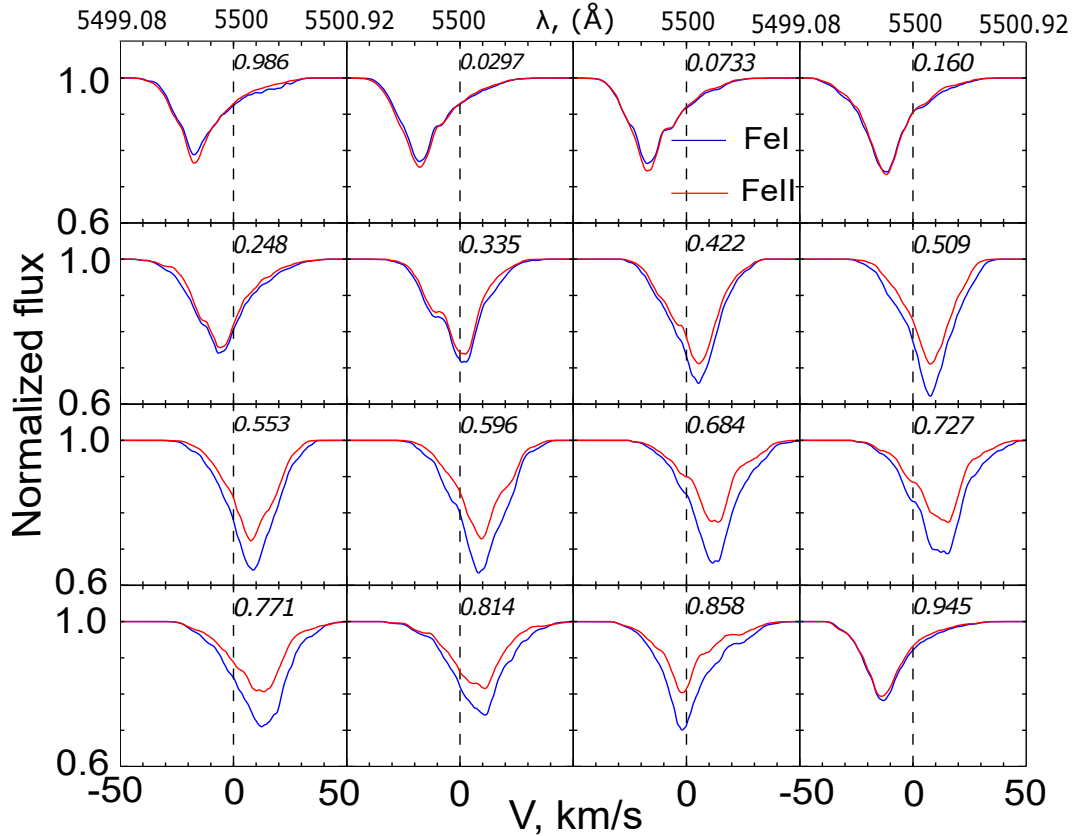


Figure 32: Fe I $E_i = 1$ eV and Fe II $E_i = 1$ eV line profiles for the strongest case as a function of photometric phase. Photometric phase ϕ_p zero coincides with maximum light.

(Sabbey et al., 1995). The 2D model provides only very limited spatial statistics. We expect that the higher degree of smoothing when averaging over the full stellar disc is reducing line asymmetries and variations in line core position, largely removing the part that is stemming from convection-related inhomogeneities. However, there is clear indication that weak lines show systematically larger variations of the line asymmetry independent of the method used to measure the line core position.

3.2.4 Line-depth ratio and the effective temperature

The ratio of depths of the spectral lines with high- and low-excitation potentials is a very sensitive temperature indicator (Gray, 1994; Gray and Johanson, 1991). This powerful method for estimating the effective temperature was applied by Kovtyukh et al. (2006) and Gray and Brown (2001) to giant stars, and by Kovtyukh and Gorlova (2000) and Kovtyukh (2007) to supergiants. The calibration of Kovtyukh and Gorlova (2000) was used by Andrievsky et al. (2005), Luck and Andrievsky (2004), and Kovtyukh et al. (2005) to determine the effective temperatures of Cepheids over a range of periods from three to ten days.

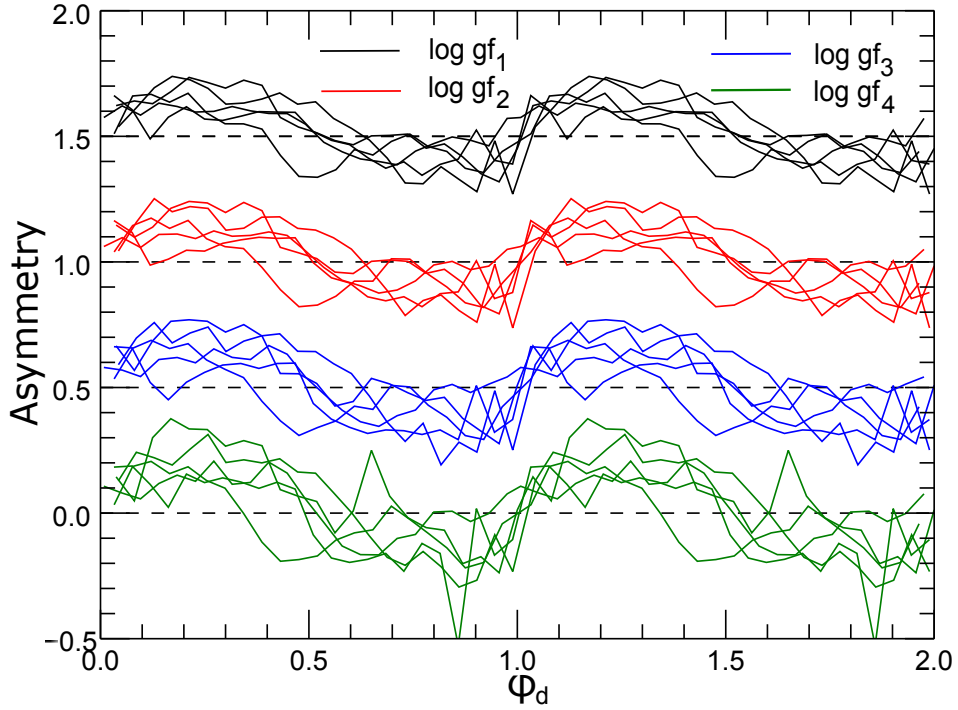


Figure 33: Line asymmetries of the Fe I $\lambda 5500 \text{ \AA}$ with $E_i = 3 \text{ eV}$ as a function of the dynamical phase ϕ_d . Line strength changes in order of oscillator strength with $\log gf_1 > \log gf_2 > \log gf_3 > \log gf_4$. Dynamical phase zero coincides with the velocity reversal from contraction to expansion in the photosphere. The line asymmetry curves are shifted by 0.5 dex relative to each other for clarity.

Kovtyukh (2007) obtained around 130 different line pair relations for estimating the effective temperatures of supergiants as a function of line depth ratio. As one example, we investigated the often used pair Fe I $\lambda 6085.27 \text{ \AA}$ and Si I $\lambda 6155.14 \text{ \AA}$. The effective temperature as a function of the Fe I $\lambda 6085.27 \text{ \AA}$ to Si I $\lambda 6155.14 \text{ \AA}$ line depth ratio $I_{\text{FeI}}/I_{\text{SiI}}$ in the 2D model is shown in Fig. 34 for two different solar-scaled abundances of Fe and Si. To calculate the photometric phase ϕ_p the radial velocity curve was fitted by a harmonic function $A \cdot \sin(\omega t + \phi_0)$.

The slope of the function $T_{\text{eff}}(I_{\text{FeI}}/I_{\text{SiI}})$ is somewhat steeper than in the case of supergiants (Kovtyukh (2007)). It is possible that for Cepheids with periods shorter than three days, dynamical effects in the atmosphere are stronger. Again, cycle-to-cycle variations due to the convective noise are clearly discernible. Interestingly, maximum T_{eff} is compatible with range of values for the line depth ratio, making the overall relation not unique, and a small line depth ratio can hint towards a low or high T_{eff} . However, such an ambiguity can be easily resolved if the phase of observation is roughly known. All in all we can confirm that the method of line depth ratios works for our 2D model. However, we see more fine-structure than a simple unique relation. Moreover, the calibration for supergiants does not fit perfectly the data of our short period Cepheid model.

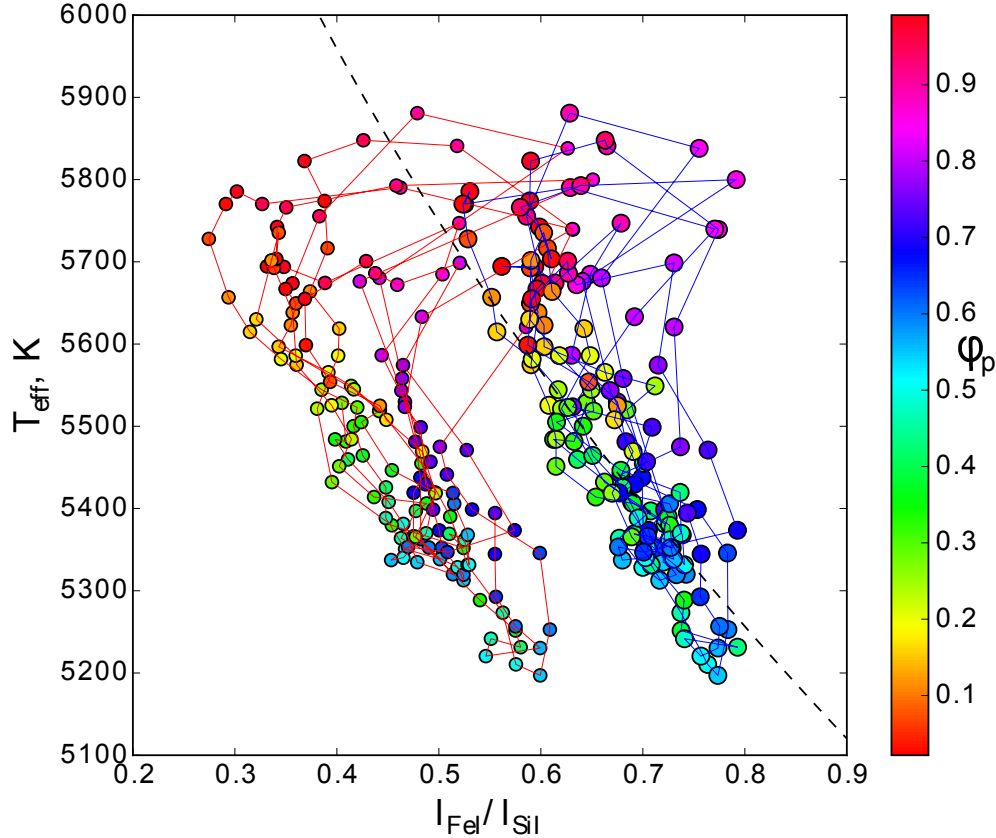


Figure 34: Effective temperature as function of the Fe I $\lambda 6085.27 \text{ \AA}$ and Si I $\lambda 6155.14 \text{ \AA}$ line depth ratio for two different abundances. Big circles connected by a blue line mark a case with +0.4 dex abundance increase for Si and Fe; small circles connected by a red line mark a case with -0.4 dex. The colour of the circles indicates the photometric phase ϕ_p . The dashed curve depicts the calibration of Kovtyukh (2007) for supergiants.

3.3 Interpretation of the "K-term"

As was emphasized by Sabbey et al. (1995), different methods of measuring the Doppler shift of absorption lines yield systematically different results. For perfectly symmetric line profiles, measuring the line-core position by using a parabolic fit to the core region (i), a Gaussian fit to the whole profile (ii), or the centroid velocity (iii), given by the first moment of the spectral line profile, yields identical results. The advantage of the third method is its independence of rotation and turbulent line broadening (Burki et al., 1982; Nardetto et al., 2006). However, the absorption line profiles of Cepheids are asymmetric. The three methods can thus lead to different results, but fortunately – as it turns out – the qualitative picture does not depend on the specific choice. The line profiles of Fe I $1 E_i = 1 \text{ eV}$ are shown for two extreme cases of the minimum and maximum of the spectroscopic radial velocity and measured Doppler shifts with these methods in the Fig. 35. For the blue shifted asymmetric line, the third method gives the smallest Doppler shift. The difference to a Gaussian fit is $\approx 5 \text{ km s}^{-1}$. For the red shifted case, the line profile is less asymmetric and all methods give almost the same Doppler velocity. From this experiment we

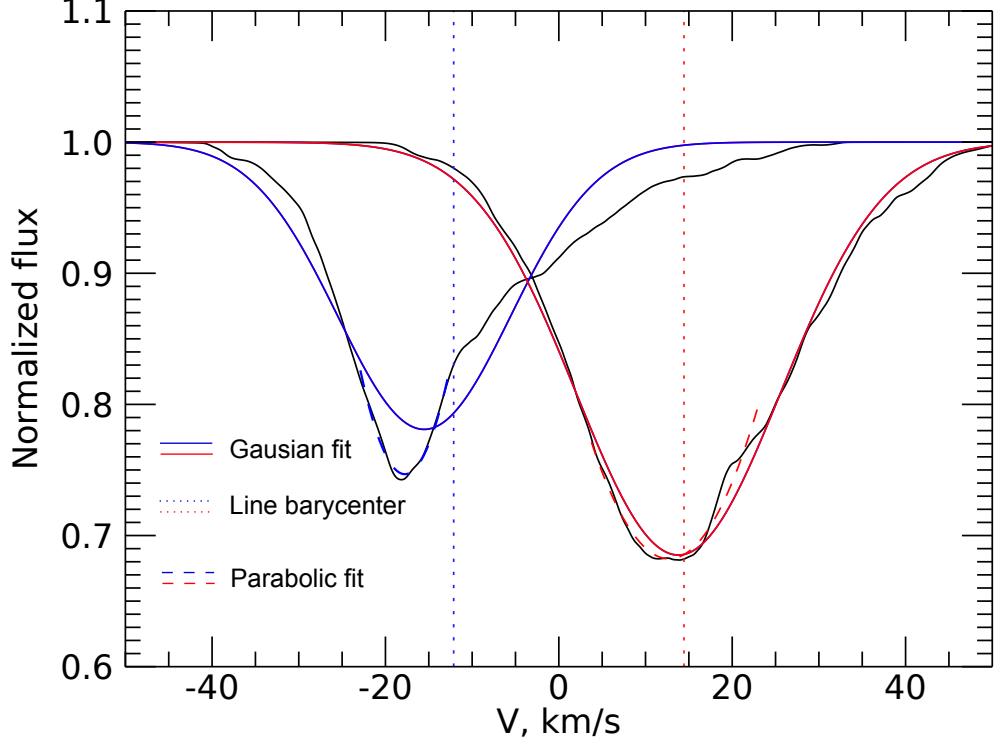


Figure 35: The line profiles of Fe I $1 E_i = 1$ eV for two extreme cases (black) of the minimum (blue) and maximum (red) of the spectroscopic radial velocity and measured Doppler shifts of the the line-core position by using a parabolic fit to the core region, by using a Gaussian fit to the whole profile and the centroid velocity.

expect that the moment method gives smaller blue-shifts, which is confirmed later (see Fig. 39). We remark that we neglect the gravitational redshift in our discussion, which is $\lesssim 100 \text{ m s}^{-1}$ for Cepheids.

In the following the spectroscopic radial velocity is based on measurement of the Doppler shift of the absorption line using both these methods.

The radial velocity does not show noticeable differences of the amplitude and phase shift for different excitation potentials and oscillator strengths (see Fig. 36). In contrast, the mean radial velocity $\langle v \rangle_t$ shown in Figs. 37, 38, and 39, which is the result of an averaging over six full cycles, exhibits dependencies on excitation potential and line strength. Additionally, the path conservation integral is not equal to zero, which is a basic assumptions in the Baade-Wesselink method (Gautschi, 1987):

$$\int_0^1 V_{\text{rad}}(\phi) d\phi = 0, \quad (126)$$

where the integral is calculated over a complete pulsation cycle. Path conservation is used to derive the centre-of-mass velocity V_γ (or γ -velocity) of a pulsating star from the above integral of the radial velocity via the condition $\int_0^1 (V_{\text{rad}} - V_\gamma) d\phi = 0$.

Observational evidence for the presence of a residual systematic velocity has existed for around 70 years (Parenago and Kukarkin, 1947; Sabbey et al., 1995; Stibbs, 1956; Wielen, 1974). The kinematic behaviour of Cepheids (Pont et al., 1994; Wilson et al., 1991) shows a "K-term", which is a residual line-of-sight velocity of the order -2 km s^{-1} (toward us) between the measured (spectroscopically) centre-of-mass velocity and the Galactic rotational velocity derived from the kinematics of stellar populations. Sabbey et al. (1995) presumed that this residual velocity is related to the varying depth of the photospheric line-forming region with pulsational phase. Based on very high quality the High Accuracy Radial velocity Planet Searcher (HARPS) observations and careful methodology, Nardetto et al. (2009) showed that the γ -velocities are linearly correlated with the line asymmetry A $V_\gamma = a_0 A + b_0$ and intrinsic properties of Cepheids. The residual γ -velocity (or K-term) averaged over eight stars was measured to $b_0 = 1.0 \pm 0.2 \text{ km s}^{-1}$.

The K-term can be affected by both pulsations and convection. To better understand the contributions of the two processes, 2D model snapshots were taken for an initial phase of the simulation run when pulsations had not set in yet. Spectral syntheses of Fe I ($E_i = 1, 3, 5 \text{ eV}$) and Fe II ($E_i = 1, 3, 5, 10 \text{ eV}$) lines as in a case of pulsations were calculated for 100 2D snapshots between $(4.5-5.8) \times 10^6 \text{ s}$. The Doppler shift of the lines was measured using parabolic fits limited to residual fluxes of 30 % above the line core, and Gaussian fits of the entire line profiles. The time-averaged radial velocities $\langle v \rangle_t$ based on the three methods are shown in top panels of the Figs. 37, 38, and 39 when pulsations have not set in. As was mentioned before, the method of fitting does not change the qualitative picture and in top panels Figs. 37, 38, and 39 show a similar dependence of the mean radial velocity on excitation potential, line strength, and ionization degree as on in bottom panels. Fe II lines with high excitation potential are forming in deeper layers of the atmosphere than in the case of the Fe I. This indicates that the effect of convection is stronger than the effect of pulsations.

Comparing the mean velocities before and after the pulsations have set in using both Gaussian and parabolic fits and the first moment of the spectral line profile (as shown in Figs. 38, 37, and 39) led us to conclude that convection is the main contributor to the residual velocity. The contribution of pulsations is not essential, and only provides a spreading with line properties leaving the averages largely intact. Therefore, we interpret the γ -velocity as the Cepheid version of the convective blueshift present in all late-type stars with convective outer envelopes. The derived values of the residual γ -velocity varies between 1.0 and 0.5 km s^{-1} dependent on method. They are close to the observed K-term for Cepheids (Nardetto et al., 2009). The dependence of the centroid velocity on the line asymmetry in the first moment method leads to a smaller residual velocity of 0.5 km s^{-1} (see Fig. 35). A parabolic fit to the core region gives $\approx 1 \text{ km s}^{-1}$ of the residual γ -velocity. The method is closer to the cross-correlation method applied for radial velocity measurements with the standard G2 mask with the HARPS spectrograph, because the widths of the "lines" of the mask is 3 km s^{-1} . This is much narrower than the width of lines in a Cepheid, and effectively leads to a determination of the line position given by the line core. The period of the 2D model is 2.8 days whereas typically Cepheids have longer periods and lower surface gravities. Spectroscopic

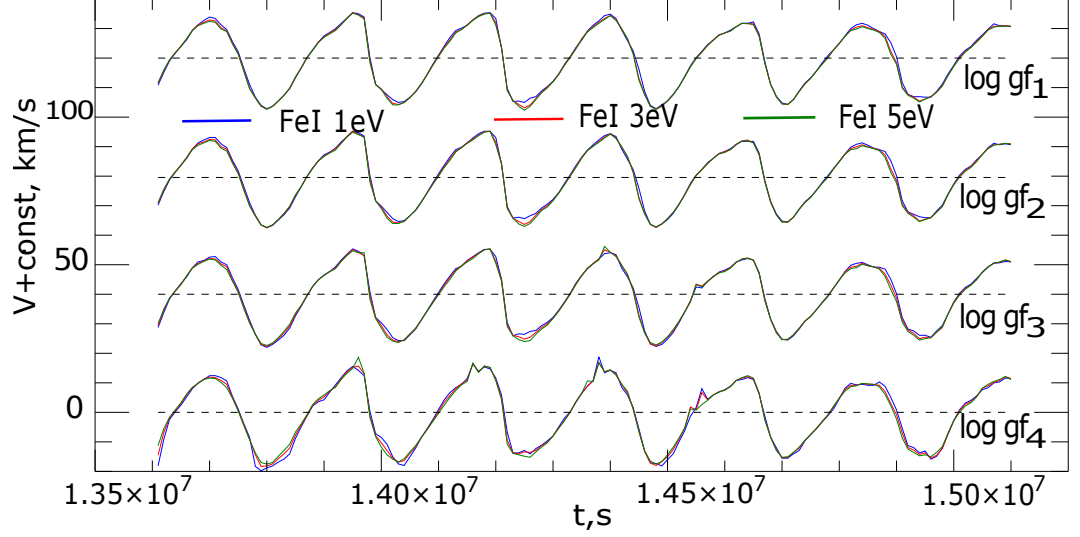


Figure 36: Radial velocities as a function of time obtained by measuring the Doppler shift of Fe I $\lambda 5500 \text{ \AA}$ $E_i = 1 \text{ eV}$ (blue), 3 eV (red), 5 eV (green) line cores using parabolic fits. Four different line strengths are shown whose EWs are ordered according to their oscillator strength $\log gf_1 > \log gf_2 > \log gf_3 > \log gf_4$. The velocity curves are shifted by 40 km/s relative to each other for clarity.

observations of Nardetto et al. (2006) indicate that for longer periods and lower $\log g$ the more vigorous convective motions produce larger residual γ -velocities.

3.4 Projection factor obtained from the 2D model

The projection factor p (also p-factor) is a key quantity in the Baade-Wesselink method for determining the distances of Cepheids. The method relates the spectroscopically measured radial velocities of a Cepheid to interferometrically measured angular-diameters (Kervella et al., 2004; Sasselov and Karovska, 1994), or classically to their brightness, by using a calibrated surface-brightness-colour relation (Barnes and Evans, 1976; Fouque and Gieren, 1997; Gieren et al., 1989; Storm et al., 2011). The method assumes the radius is defined at a specific location in the stellar atmosphere, for example, at an optical depth $\tau = 2/3$. The change of the radius is $\Delta R = \int v_{\text{puls}} dt$, where the pulsation velocity v_{puls} is the velocity of optical layers corresponding to the optical depth $\tau = 2/3$. The projection factor p converts the spectroscopic radial velocity to a pulsational velocity: $v_{\text{puls}} = p \cdot v_{\text{rad}}$. Spectroscopic radial velocities include effects related to two kinds of integration over the stellar surface layers: horizontally, the effects of limb-darkening, and vertically, the effects of velocity gradients in the line-forming region.

The impact of limb-darkening and atmospheric expansion on the p-factor was first studied by Eddington (1926) and Carroll (1928). Parsons (1972), using a model atmosphere with uniform expansion, numerically determined the p-factor to be between 1.31 and 1.34, depending on the width of a line. Many attempts were made to estimate and calibrate the p-factor from high-

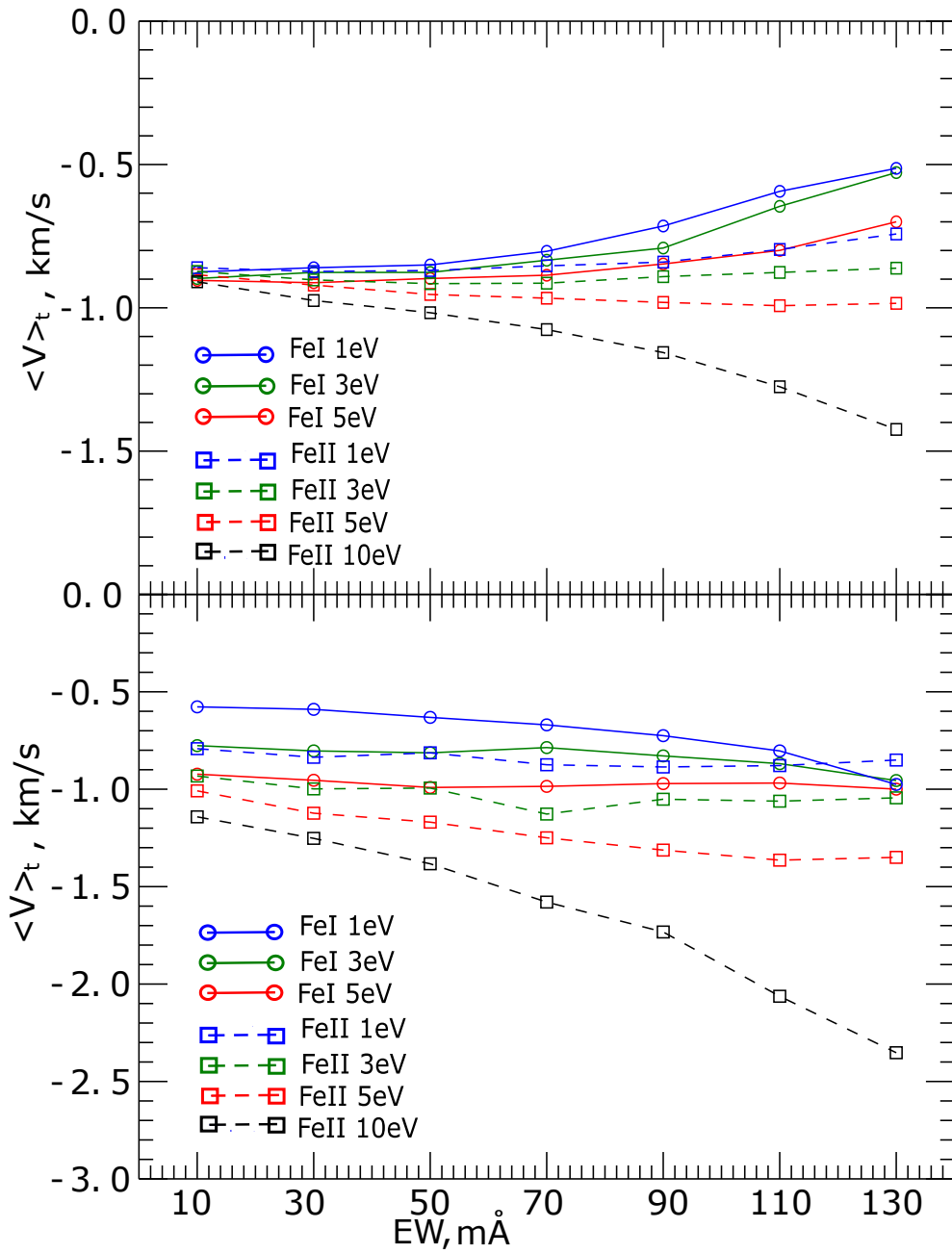


Figure 37: Bottom panel: Time-averaged radial velocities $\langle v \rangle_t$ of Fe I and Fe II lines as a function of their EW. The measurement of the Doppler shift is based on parabolic fits of the line core deeper than 70% of the total line depth. Top panel: Time-averaged radial velocities from line core fitting when pulsations have not set in.

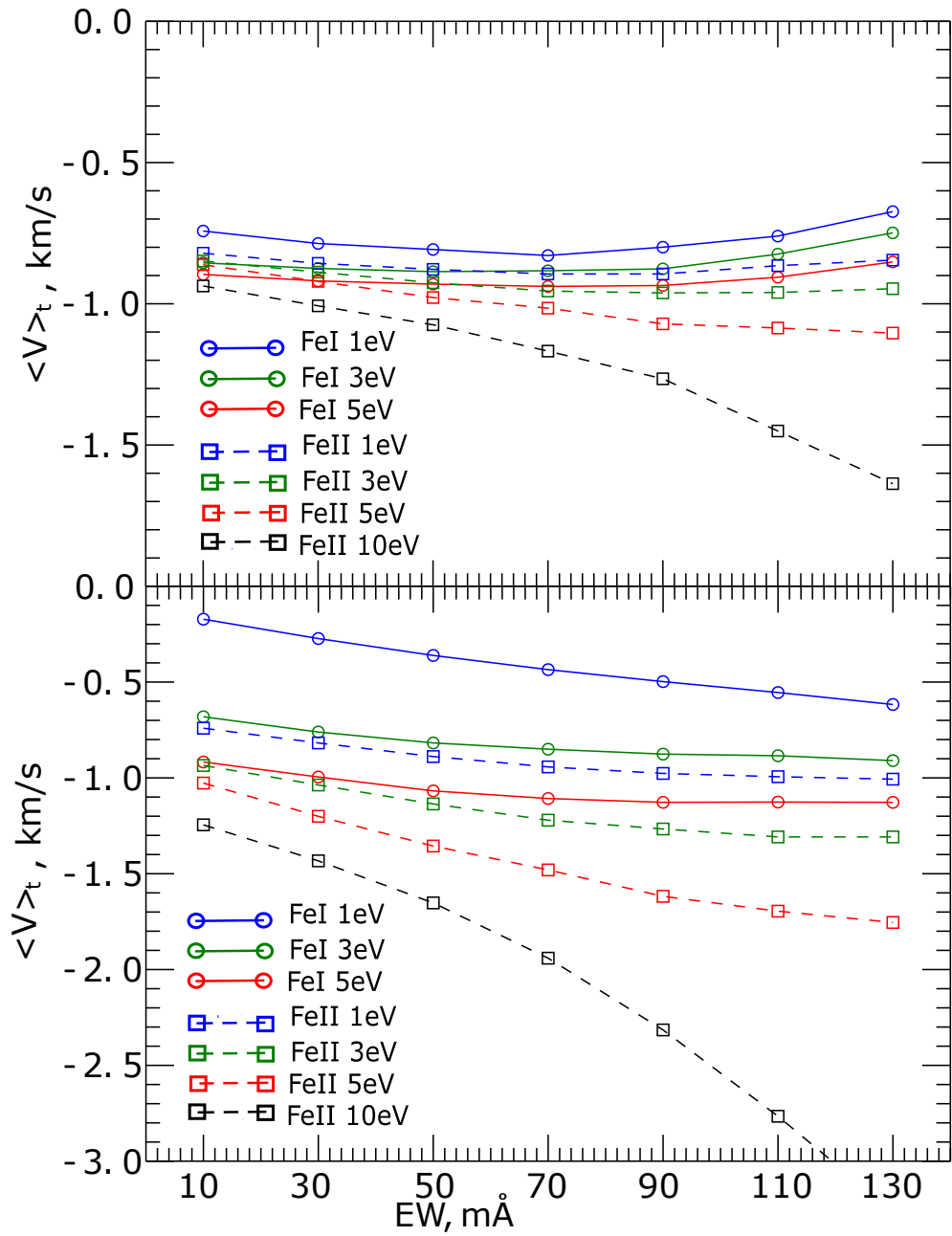


Figure 38: Bottom panel: Like Fig. 37, but measuring the Doppler shift by a Gaussian fit of the whole line profile. Top panel: Time-averaged radial velocities from Gaussian fitting when pulsations have not set in.

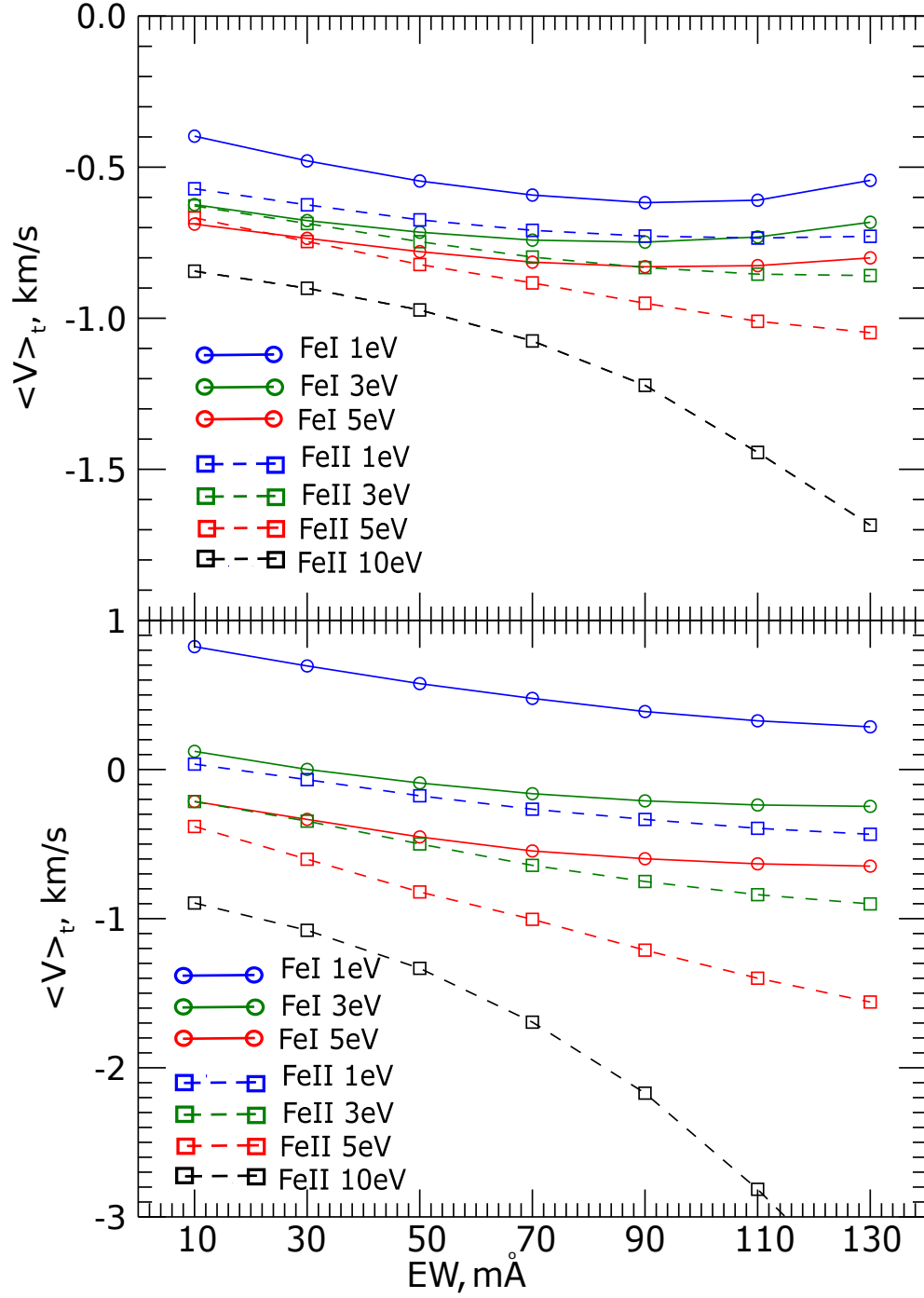


Figure 39: Bottom panel: Time-averaged radial velocities $\langle v \rangle_t$ of Fe I and Fe II lines as a function of their EW. The measurement of the Doppler shift is based on the barycenter of the spectral line. Top panel: Time-averaged barycenter radial velocities when pulsations have not set in.

resolution spectroscopic observations (Breitfelder et al., 2015, 2016; Nardetto et al., 2004, 2007, 2009, 2013, 2017; Neilson et al., 2012). Nardetto et al. (2007) identified three effects affecting the projection factor: the geometrical effect, the velocity gradient within the atmosphere, and the relative motion of a layer of given optical depth with respect to a corresponding fixed Lagrangian mass element.

Our Cepheid model provides information about the pulsating velocity $v_{\text{puls}}(\tau_R = 2/3)$. The photospheric radius $R_{\text{ph}}(\tau_R = 2/3)$ was calculated with a cubic spline interpolation using data of the mean 1D model. The pulsating velocity is $v_{\text{puls}} = dR_{\text{ph}}/dt$, which was calculated for each instance in time over six full periods. The projection factor is the slope of the curve $v_{\text{puls}} = p \cdot v_{\text{rad}} + v_o$, which is shown in Fig. 40 for the line Fe I $E_i = 1 \text{ eV}$ and three different line strengths. We implemented the fitting to deal with the substantial amount of convective noise present in the model data. Depending on line strength the p-factor varies between 1.23 and 1.27, which agrees with estimates from the literature (Nardetto et al., 2009). Additionally, within the given noise level, Fig. 40 shows the absence of a hysteresis-like behaviour between the pulsational and radial velocities as was found when investigating the relation between effective temperature and line depth ratio (Fig. 34).

The fitting parameter v_o is related to the K-term. The presence of residual γ -velocity shifts the curve $v_{\text{puls}} = p \cdot v_{\text{rad}} + v_o$ to negative radial velocities along the horizontal axis so that $K = -v_o/p$. The derived K-term from the linear fits as a function of line strength is shown in Fig. 41.

From the physical point of view, the pulsational velocity is related to the motion of mass elements in the atmosphere during the pulsations. One can estimate the pulsational velocity using the velocities of mass elements close to the photosphere, and thereby calculate the projection factor. The variation of the geometric vertical coordinate of a layer in the photosphere with $\tau_R = 2/3$ and a Lagrangian mass element is shown in Fig. 42. The pulsational velocity of these layers is shown in Fig. 43. The pseudo-Lagrangian velocity of the mass element is almost equal to the velocity of the optical depth surface $\tau_R = 2/3$ in the photosphere. That means that in our model we find the same projection factor for the pseudo-Lagrangian velocity, or the velocity of a layer of given optical depth (in the photosphere).

3.5 Summary

A pilot study of spectroscopic properties of a multi-dimensional Cepheid model was conducted. We arrive at the following conclusions:

1. The 2D model shows self-excited pulsations due to the κ -mechanism with a 2.8-day period. It reproduces the observed relation between the brightness and radial velocity amplitudes of pulsating stars (Kjeldsen and Bedding, 1995).

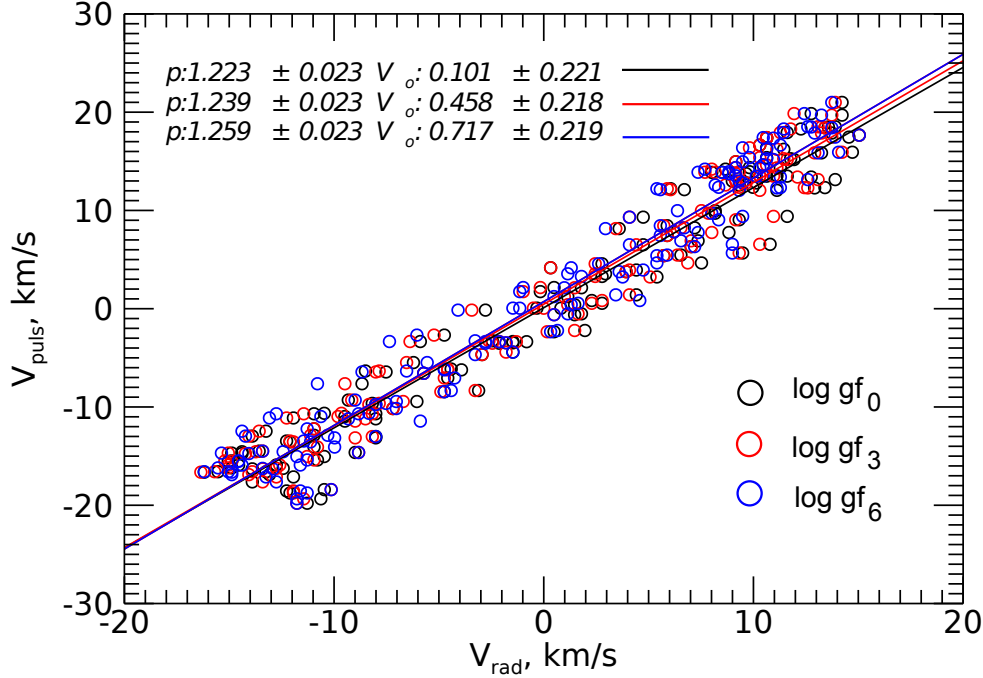


Figure 40: Pulsational velocity as a function of the radial velocity, estimated by Gaussian fits of the whole Fe I $E_i = 1$ eV line profiles. Colours show different line strengths: the strongest line is depicted in black, the weakest in blue. The slope of the linear regression is the p -factor.

2. We find a net mean shift of the spectrum of the model Cepheid by $-0.5 \dots -1 \text{ km s}^{-1}$ which is a significant fraction of the observed residual line-of-sight velocity seen in the Cepheid population.
3. We interpret this shift as the convective blueshift familiar from non-pulsating late-type stars. It is possible that multi-dimensional models with lower surface gravity (more similar to typical Cepheids) give higher convective and, eventually, higher residual velocities bringing the models closer to observations. This needs to be investigated further.
4. The microturbulent velocity, derived for individual iron lines, shows a modulation with pulsational phase and depends on the line properties. When averaged over all lines, it varies between 1.5 and 2.7 km s^{-1} over the pulsational cycle. This is somewhat lower than the velocity obtained in classical analyses with 1D hydrostatic atmosphere models (Andrievsky et al., 2001). Reasons for this shortcoming may be the limited spatial resolution of the model, or the different methodology used in the determination of the microturbulent velocity. However, around photometric phase 0.9 before maximum light, the microturbulent velocity curve exhibits distinct peaks. This is qualitatively in agreement with the temporal behaviour of turbulent velocities in Cepheids as measured by Borra and Deschatelets (2017) using an autocorrelation technique.
5. Line asymmetries show a behaviour that is qualitatively similar to observations. However,

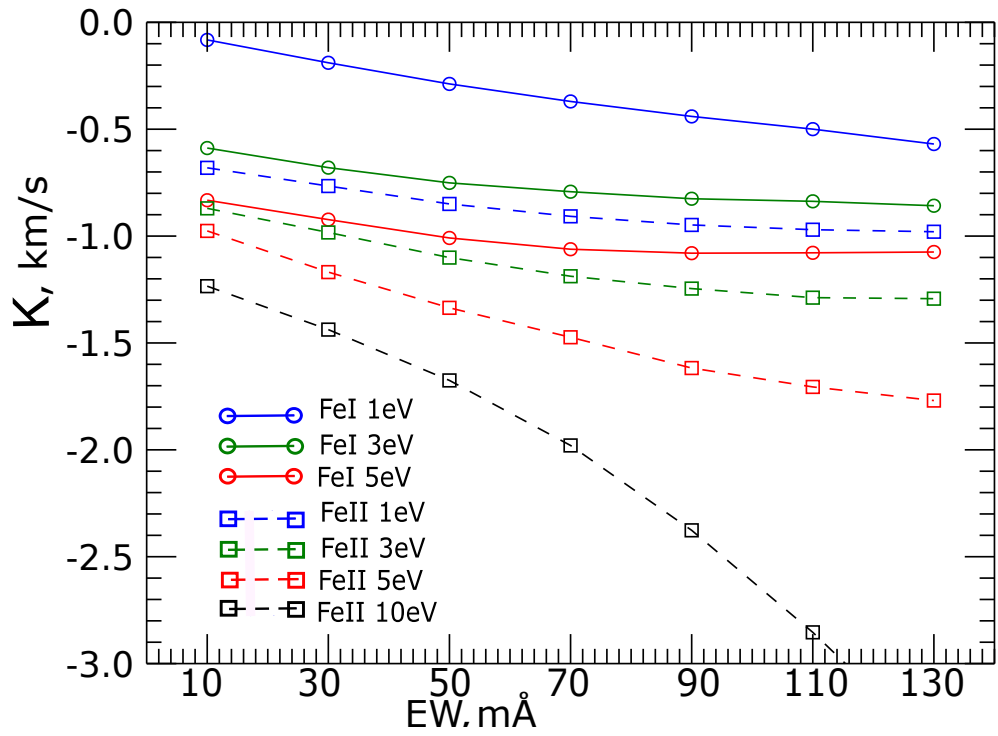


Figure 41: Residual velocity or K-term derived by linear fits of the curve $v_{\text{puls}} = p \cdot v_{\text{rad}} + v_0$ and $K = -v_0/p$ for different line strengths and excitation potentials. The spectroscopic radial velocity is measured by Gaussian fitting.

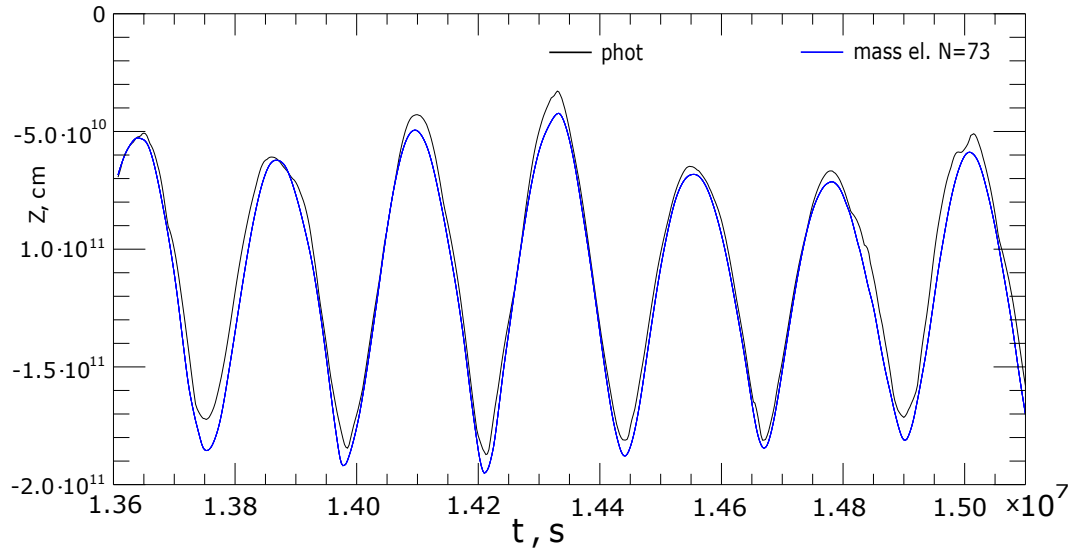


Figure 42: Vertical geometric coordinate of a layer in the photosphere with $\tau_R = 2/3$, and the corresponding pseudo-Lagrangian mass element as a function of time.

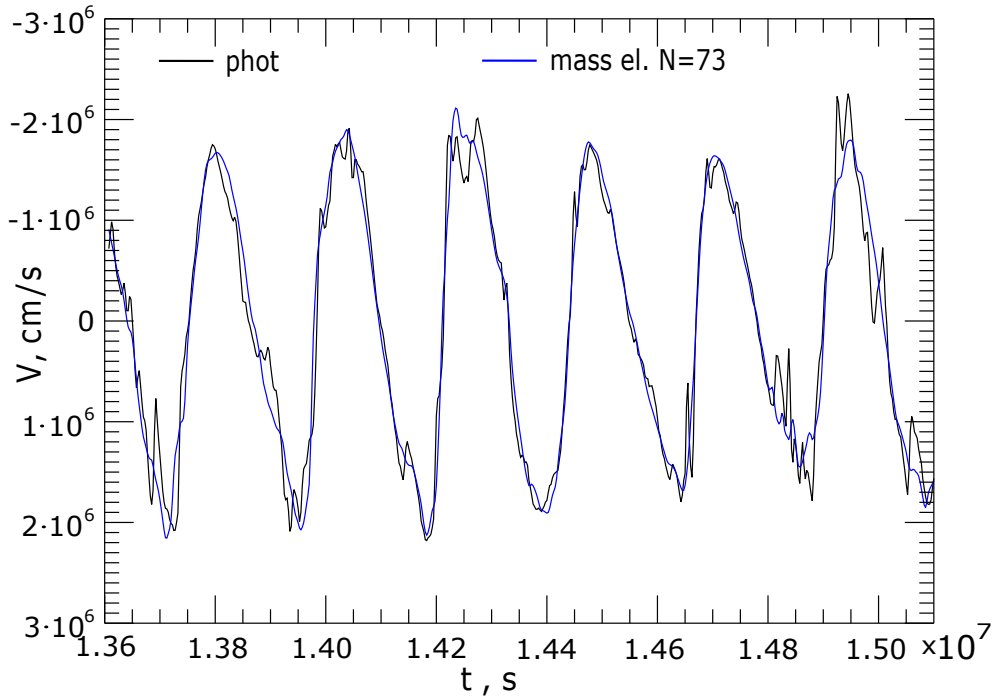


Figure 43: Pulsational velocities of a layer in the photosphere with $\tau_R = 2/3$, and of the corresponding pseudo-Lagrangian mass element as a function of time.

limited statistics makes it difficult to perform more quantitative comparisons.

6. The projection factor derived from the 2D model lies between 1.23 and 1.27, and agrees with observations (Nardetto et al., 2009).

Taken together I find a reasonable correspondence between the model and observed properties of Cepheid variables. This is far from self-evident considering the computational problems one faces when trying to simulate a Cepheid envelope exhibiting self-excited pulsations together with violent atmospheric dynamics. The 2D geometry together with detailed spectral syntheses sets our model apart from most previous modelling works. It allowed to study the impact of convective inhomogeneities, which turned out to be important for some spectroscopic properties – here in particular for the K-term – and, as I will present in next chapter, for the determination of elemental abundances.

4 SPECTROSCOPIC INVESTIGATION OF A 2D CEPHEID MODEL II.

Based on Vasilyev et al. (2017b).

This chapter is a continuation of the spectroscopic investigation of the 2D Cepheid model introduced in the previous Chapter 3. The results presented here are based on my second first author paper (Vasilyev et al., 2017b), which was recently accepted for publication in *Astronomy & Astrophysics*.

Here, I consider the results of spectral syntheses taking the two-dimensional Cepheid model for providing artificial observational data. Then, I apply the standard approach to determine stellar parameters using calculated 1D plane-parallel hydrostatic model atmospheres. The advantage of the 2D model is that stellar parameters are exactly known. Thus, one can check the standard approach for biases on parameters, including dependencies on the pulsational phase. Since I only have one multi-dimensional model at hand, my findings are restricted to the class of short-periodic Cepheids.

Bellow I describe how the chapter is organized. The calculated grid of 1D models is presented in Section 4.1. In Section 4.2 I describe the line list and compare it with line lists actually applied in the measurement of Galactic metallicity gradients. Features of spectral line profiles from the 2D model are discussed in Section 4.3. Results for the determination of stellar parameters for four-, three- and two-parametric case are presented in Section 4.5. Finally, I summarize the results in Section 4.6.

4.1 The grid of 1D LHD models

A grid of 1D plane-parallel hydrostatic models was calculated using a Lagrangian hydrodynamics code (here after LHD), which solves the set of 1D radiation-hydrodynamics equations in the Lagrangian frame. Convective fluxes and velocities were calculated according to MLT. In the present work, the mixing-length parameter α was fixed to 1.5 for all 1D models. The actual value of the mixing-length parameter has a minor effect on the photospheric temperature structure of the 1D models since the convective zone does not reach into the optically thin regions of the giant stars considered here.

The radiative flux of 1D LHD models was calculated using gray opacities. The radiative transfer equation was solved adopting the Feautrier scheme (Feautrier, 1964). Opacities, the equation of state, and the chemical composition were taken as for the 2D model. The effective temperatures of 1D models were varied between 4900 K and 6000 K in steps of $\Delta T = 100$ K. They cover the effective temperature range that is encountered during the temporal evolution of the 2D model. The upper boundary of 1D models of the grid was set to below $\log \tau_{\text{R}} < -6$ to contain the line-formation

regions of the given line list, which is described in the next sections.

The surface gravity $\log g$ of 1D LHD models was taken in the range 0.7 to 3.5 in steps of $\Delta \log g = 0.2$ to cover the effective gravity range – including acceleration effects – found in the 2D model. The equivalent width (EW) of a spectral line depends on the physical conditions in the line formation region of the stellar atmosphere. The pressure is one of the key quantities that influence the EW. This quantity, in turn, is controlled by the surface gravity \vec{g} . In stellar atmospheres that are in hydrostatic equilibrium, the pressure gradient, ∇p , is balanced by the gravity force:

$$\frac{\vec{\nabla} p}{\rho} = \vec{g}, \quad (127)$$

where ρ is the density. In the 2D model, the dynamics adds to the purely gravitational acceleration, which results in a total acceleration that has to be balanced by the pressure gradient. The effective gravitational acceleration is the sum of the effects of gravity and kinematic acceleration, $\frac{d\vec{v}}{dt}$:

$$\frac{\vec{\nabla} p}{\rho} = \vec{g} - \frac{d\vec{v}}{dt} = \vec{g}_{\text{eff}}. \quad (128)$$

In the 2D model, the gas and turbulent pressures $\vec{\nabla} p = \vec{\nabla} p_{\text{gas}} + \vec{\nabla} p_t$ contribute to the total pressure. Since it is primarily caused by convection, the turbulent pressure p_t is significant at the bottom of the photosphere. However, the gas pressure gradient still provides the dominant contribution to the total pressure gradient even deep in the photosphere (see Fig. 23 in Chapter 3) and line-formation regions. Finally, the effective gravity of the 2D model was derived with the total pressure gradient. We did not include turbulent pressure in the 1D models so that $\nabla p = \nabla p_{\text{gas}}$. Even if we had tried to do so in the framework of MLT, it would have had little effect since the convective zone is restricted to layers below the photosphere.

If we consider a Lagrangian mass shell following the mean vertical mass motion in the line formation region, we find that it is subject to substantial acceleration during the pulsations. When the direction of motion at the phase of maximum compression is reversed, it experiences an acceleration of $\approx (1.0 \dots 2.5) \vec{g}$. In total, this corresponds to an effective gravitational acceleration of $\vec{g}_{\text{eff}} \approx (2.0 \dots 3.5) \vec{g}$, which in 1D models would have to be balanced by the pressure gradient according to Eq. (128). For now, we recall that the line formation in a dynamical atmosphere occurs under a variable effective gravity. While kinematic effects have a rather obvious impact, spectroscopically determined surface gravities can also be affected for other reasons. For instance, according to Steffen (1985) and Korn et al. (2003), the surface gravity of Procyon as deduced from the ionization balance is inconsistent with an independent estimate obtained with astrometric methods.

For Cepheids, a mean gravity can be estimated without a spectroscopic analysis. Gough et al.

(1965) theoretically derived the "period-gravity" relation,

$$P \sim g^{-1}, \quad (129)$$

where P is the pulsational period. The empirically calibrated "period-gravity" relation of Tsvetkov (1988) can be used to estimate the mean gravity, and this can be taken as a first approximation to derive stellar parameters. According to Andrievsky et al. (2002b) (their Fig. 1), however, pulsations produce a scatter of 0.8 around the mean value.

The full grid of 1D LHD models in the $T_{\text{eff}}\text{-log } g$ plane is shown in Fig. 44. With different temperature and gravity grid models, we intend to represent the states of the dynamical 2D atmosphere encountered in the different pulsational phases. It is clear that hydrostatic equilibrium is never exactly reached in the 2D model. The timescale to attain hydrostatic equilibrium is on the order of the sound-crossing time, which is on the same order as the pulsational period. We might expect conditions with low effective gravity around the phase of maximum expansion. At this point, the timescale of the convective instability becomes longer than the pulsational period because of a low effective gravity, which in turn decreases the efficiency with which the turbulence is generated. The thermal structure is less perturbed by dynamical effects than in the phase of maximum compression. For et al. (2011) found that photometric phases around ≈ 0.35 (photometric phase zero corresponds to maximum light) are optimal for chemical abundance analyses of RR Lyrae stars with hydrostatic model atmospheres. Recalling the differences between RR Lyrae and Cepheid variables (RR Lyr stars have higher effective temperatures, higher velocity amplitudes, shorter periods of pulsation, and exhibit stronger atmospheric shocks), we expect similarities and address this point below.

4.2 The list of artificial iron lines

For an accurate spectroscopic analysis, the line list and wavelength interval have to be carefully selected. Classically, the line list for the metallicity determination contains isolated, unblended iron lines of different ionization stages and excitation energies that cover a wide range of EWs. The line strength depends on the physical conditions in the stellar atmosphere. Thus, depending on the star, we have to include or exclude different spectral lines in the analysis.

To keep our analysis general and to obtain a systematic overview, we did not use a particular list of Fe I and Fe II lines. Instead, our line list consisted of 49 fictitious neutral and singly-ionized iron lines with a fixed wavelength of $\lambda = 5000 \text{ \AA}$. Excitation energies of the Fe I and Fe II lines were taken to be $E_i^{\text{Fe I}} = 1, 3, 5 \text{ eV}$ and $E_i^{\text{Fe II}} = 1, 3, 5, 10 \text{ eV}$, respectively. The oscillator strengths were set to cover a wide range of EWs from 5 m\AA to 200 m\AA .

Figure 45 shows the line parameters in the excitation potential – oscillator strength plane. We also plot a list of real Fe I and Fe II lines, which was used by Lemasle et al. (2007, 2008), Pedicelli

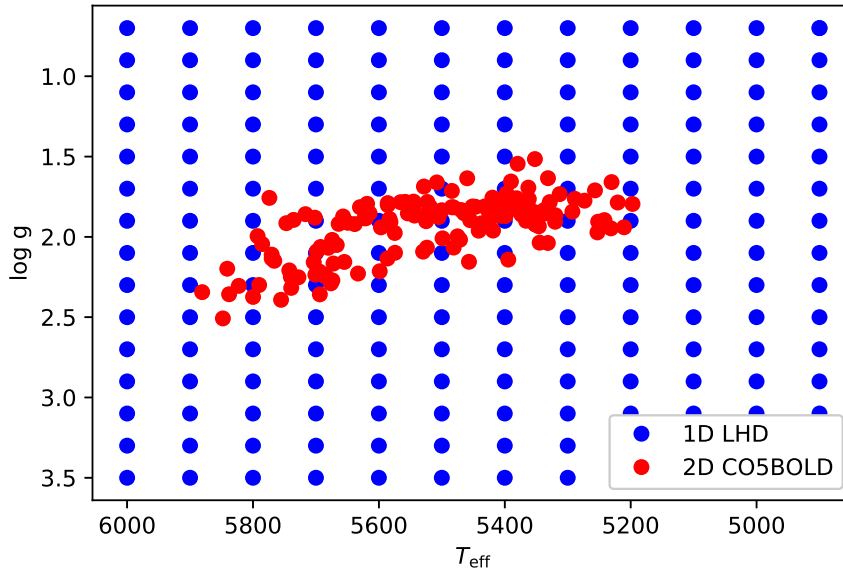


Figure 44: Grid of 1D hydrostatic LHD models (blue circles) in the $T_{\text{eff}}\text{-log } g$ plane, and effective temperatures and gravities of the two-dimensional model (red circles) for 150 instances in time, covering six full periods of pulsation.

et al. (2010), and Genovali et al. (2013, 2014), to investigate the chemical composition of Galactic Cepheids and measure the Cepheid metallicity gradient in different parts of the Galactic disk. The group of Fe II 10 eV lines is unrealistic with respect to lines used in observational analyses because of large oscillator strengths and excitation potential. Owing to the high-excitation energy, these lines form in deep regions of the atmosphere. As a consequence, they are strongly influenced by convection. Especially during the maximum compression phase, the convection is amplified through the high effective gravity (see Paper I). In order to be closer to the list of real lines, and because of the strong sensitivity of the Fe II 10 eV lines to dynamical effects, we did not consider these lines when we determined the stellar parameters of the dynamical model. On the other hand, because of the infinite signal-to-noise ratio of our theoretical spectra, we did not exclude the weakest lines with excitation potentials of 1, 3, and 5 eV in the analysis. The spectral synthesis was performed with Linfor3D⁶ (Gallagher et al., 2017) for the dynamical and 1D LHD models assuming local thermodynamic equilibrium.

Before we describe our method for determining the stellar parameters and present our results, we first discuss the features of the line profiles of the dynamical model.

⁶<http://www.aip.de/Members/msteffen/linfor3d/>

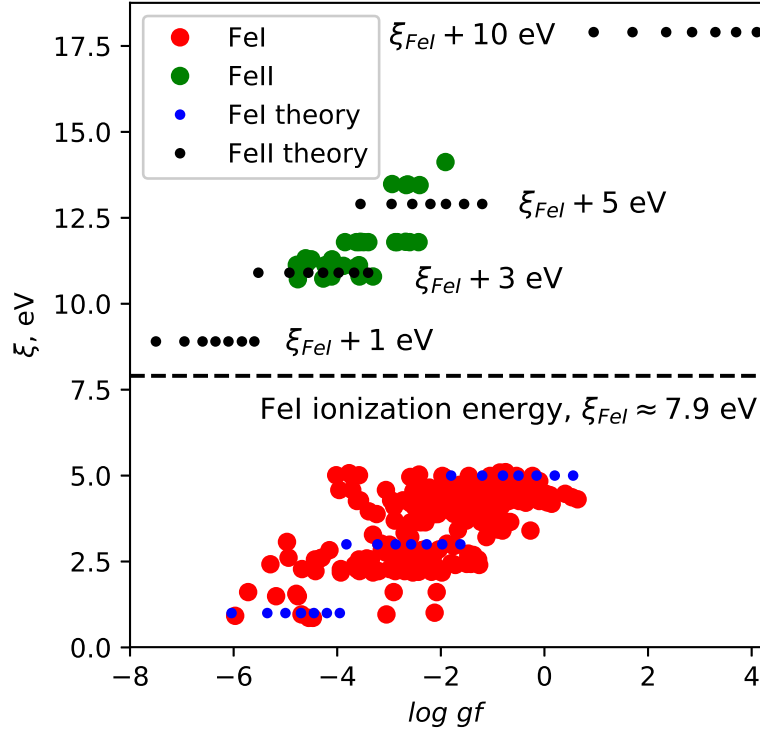


Figure 45: Real (large circles) and our theoretical (small circles) Fe I and Fe II lines in the excitation energy–oscillator strength plane.

4.3 Spectral line profiles of the dynamical 2D model

The homogeneous expansion or contraction of the atmosphere of a spherical pulsating star transforms a symmetric Gaussian absorption line into a characteristically asymmetric shifted line profile, as was shown early on by Shapley and Nicholson (1919). The asymmetry and shift depend on the radial velocity of the line formation region (Nardetto et al., 2006). However, the expansion or contraction of the atmosphere of a pulsating star is not perfectly homogeneous. This can, for instance, be observed in Balmer line profiles of RR Lyrae stars (Preston, 2011) or is predicted by global 3D radiation-hydrodynamics models of AGB stars (Freytag et al., 2017), and it is also demonstrated by our results in Chapter 3. While in observations the line profile is observed averaged over the whole stellar disk, the spectral synthesis for our 2D model provides information on the variation in the spectral line profile in a spatially resolved fashion.

Figure 46 shows the spatial variation along the horizontal position in the modeled 2D box of the normalized line profile of the strongest Fe II 3 eV line in terms of intensity in vertical direction (inclination cosine $\mu = 1$). The particular instance in time corresponds to a photometric phase of 0.56, illustrating a situation during the contracting phase of the 2D model. Absorption as well as emission features are discernible. The line profiles vary widely in terms of radial velocities

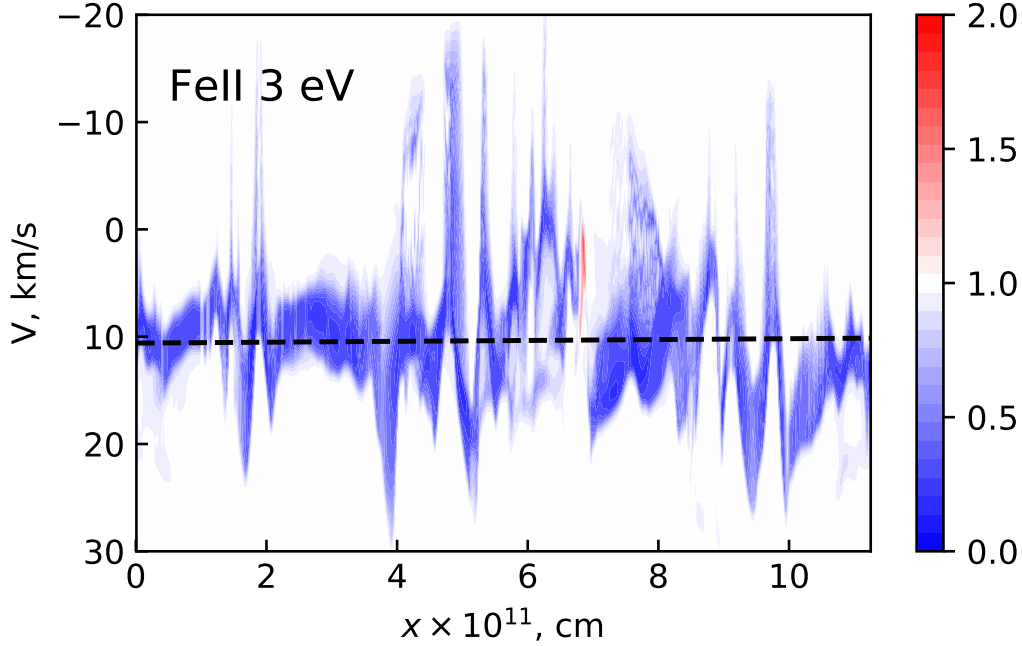


Figure 46: Two-dimensional map of normalized line profiles of the strongest Fe II 3 eV line in terms of normalized intensity for a photometric phase of $\phi_{\text{ph}} = 0.56$. The horizontal axis shows the horizontal spatial position within the modeled box. The vertical axis represents the wavelength expressed as Doppler velocity. Emission and absorption are indicated by red and blue lines, respectively. The continuum level is one, and it is shown in white. The mean Doppler velocity is depicted by the dashed line. The standard deviation of the Doppler shift velocities is 6.1 km s^{-1} .

and asymmetry, sometimes showing a multi-component structure. The mean radial velocity is roughly 10 km s^{-1} for the given example, with significant spatial variations caused by convective inhomogeneities.

Around a horizontal position $x \approx 7.5 \times 10^{11} \text{ cm}$, emission lines are present. Figure 47 shows vertical 1D thermal $T(\tau_{\text{R}})$ and radial velocity profiles around the location of emission. We note that we use the spectroscopic sign convention for the radial velocity, where a negative velocity corresponds to a motion toward the observer and vice versa. The Fe II 3 eV line formation region is located at $\log \tau_{\text{R}} \approx -3 \dots 0.7$. Emission line profiles occur because of an inverse gradient of the temperature at optical depths $\log \tau_{\text{R}} < -1.5$. The photospheric temperature of the thermal profile is $\approx 4000 \text{ K}$. Local disturbances of the thermal profile by convection can produce cold regions. However, as was shown in Paper I, the variation in effective temperature of the mean 2D model, which is the result of the horizontal averaging of the full 2D model at fixed geometrical height, varies in a range between 5300 and 5900 K.

The inverse temperature gradient and jump of the radial velocity at $\log \tau_{\text{R}} \approx -2$ in Fig. 47 correspond to an accretion front, where almost free-falling low-density material collides with a quasi-hydrostatically stratified deeper layer. The velocity difference between pre- and post-shock

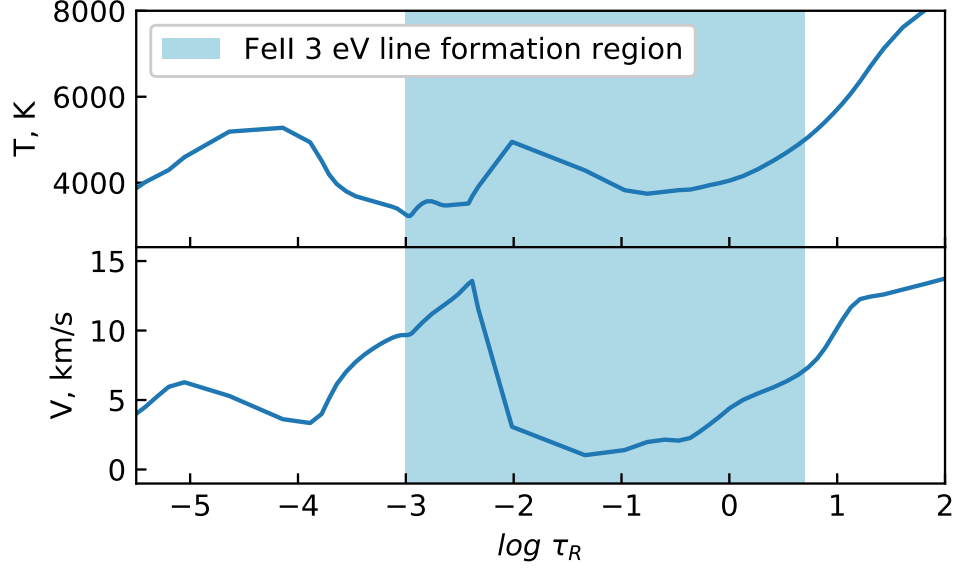


Figure 47: Vertical thermal and radial velocity profiles of the section of the 2D model in which the emission line profile of the strongest Fe II 3 eV line occurs. The line formation region is indicated by the light blue area.

regions is $\approx 10 \text{ km s}^{-1}$, which is substantial. As was described in Paper I, we applied an artificial drag force at a number of grid layers close to the top, reducing the velocities by a certain fraction per time interval. The drag force, which dampens waves, leads to a heating of the top of the modeled box. This is visible at the temperature profile in the regions where $\log \tau_R < -3.5$. To minimize the effect of the upper boundary, we considered lines that form at $\log \tau_R > -4$.

4.4 Methodology of the parameter fitting

One of the traditional ways to determine stellar parameters and elemental abundances is based on minimizing the difference between observed and synthesized line profiles by varying the model parameters of a precomputed grid. However, in our analysis, we did not compare line profiles because, as we showed in the previous section, the line profiles of the 2D model are asymmetric, Doppler-shifted, and have a multi-component structure. The line asymmetry depends on the pulsational phase, whereas 1D LHD line profiles are perfectly symmetric and unshifted and thus can only poorly represent the 2D profiles. For these reasons, we only matched the EW of the lines. In the 1D spectral synthesis, the microturbulent velocity ξ_t was varied in the range 0.0 km s^{-1} to 7.0 km s^{-1} in steps of 0.5 km s^{-1} to cover a typical observational range (Andrievsky et al., 2002a). The same microturbulent velocity ξ_t was adopted for all lines from the line list. The result of the spectral synthesis is an array of EWs $W_i = f_i(T_{\text{eff}}, \log g, \xi_t)$, where the index i is a line number running from 1 to 42 for our set of artificial iron lines.

Observationally, the metallicity of an observed star is an unknown parameter. We mimicked this

by including the iron abundance (metallicity), $\log A$, as an additional parameter together with T_{eff} , $\log g$, and ξ_t . The EW of a spectral line depends on the product of the abundance A and oscillator strength gf , on a logarithmic scale $\log A + \log gf$. For a fixed $\log gf$, the abundance $\log A$ was changed between $-0.6 \dots 0.0$ dex and $0.0 \dots 0.6$ dex in steps of 0.1 dex. Corresponding EWs were calculated using a cubic spline interpolation in $\log W$ - $\log gf$ space.

The EWs calculated with the grid of 1D LHD models were finally used to best match the EWs from the spectral synthesis of the dynamical model. We introduced a χ^2 function to characterize the mean relative difference between the EWs of the 2D and 1D models, which is in general a function of the 4D vector $\vec{p} = \{T_{\text{eff}}, \log g, \xi_t, \log A\}$

$$\chi^2(\vec{p}) = \frac{1}{N} \sum_j \left[\frac{W_j^{2D} - W_j^{1D}(\vec{p})}{f \cdot \sigma_{w,j}} \right]^2, \quad (130)$$

where the sum goes over all iron lines of our line list, N the total number of lines, and f is an arbitrary scaling factor for the assumed uncertainty $\sigma_{w,j} = W_j^{2D}$. It should be understood that the uncertainty stated above is not a statistical uncertainty, since our synthetic lines are not subject to noise. Taking the uncertainty as proportional to the line strength itself was a convenient and reasonable way to express the deviations in line strengths. We used a scaling factor $f = 1$, which in the following allows a straightforward interpretation of a χ^2 value: the square-root of a given χ^2 is the relative RMS deviation between 2D model and 1D model line strengths.

The best-fit combination of the parameters is found at the minimum of the χ^2 function. We performed an exhaustive search of the minimum over our grid of 1D models and took the model with minimum deviation as a first approximation. To improve the location of the minimum, we interpolated between grid points. We tested three different interpolation methods to further locate the minimum in the 4D parameter space:

1. Radial basis functions (RBF) with a norm

$$\frac{1}{\sqrt{(\vec{p}/\Delta\vec{p})^2 + 1}} = \left[\sum_{i=1}^4 \left(\frac{p_i}{\Delta p_i} \right)^2 + 1 \right]^{-1/2}, \quad (131)$$

where $\Delta\vec{p} = \{\Delta T_{\text{eff}}, \Delta \log g, \xi_t, \Delta \log A\}$ is the smoothing scale. The choice of the scale is based on the spacings in our grid of 1D models, which are $\Delta T_{\text{eff}} = 100$ K, $\Delta \log g = 0.2$ dex, $\xi_t = 0.5$ km s⁻¹, and $\Delta \log A = 0.1$ dex.

2. A fit of a quadratic form to reconstruct the shape of the function around the minimum.
3. A sequence of 1D cubic piecewise interpolations.

Before we applied the methods for the analysis of EWs of the 2D model, they were tested on EWs of one custom computed 1D model with $T_{\text{eff}} = 5550$ K, $\log g = 2.0$ dex, $\xi_t = 1.75$ km s⁻¹, and $\log A = -0.05$ dex, which is located between points of the grid.

4.4.1 Test with radial basis functions

The minimum point and its 80 nearest-neighbor points were taken to describe the χ^2 function with RBFs:

$$\chi^2(\vec{p}) = \sum_{j=1}^{81} \frac{\omega_j}{\sqrt{\sum_{i=1}^4 \left(\frac{p_i - p_{ij}}{\Delta p_i} \right)^2 + 1}}, \quad (132)$$

where the weights ω_j are results of the solution of the linear system of equations:

$$\sum_{j=1}^{81} p_{ij} \omega_j = \chi^2(\vec{p}_i), \quad (133)$$

with p_{ij} being the distance between the vectors \vec{p}_i and \vec{p}_j in the parameter space. The reconstructed parameters for the test case are $T_{\text{eff}} = 5557$ K, $\log g = 2.03$ dex, $\xi_t = 1.77$ km s⁻¹, and $\log A = -0.035$ dex.

4.4.2 Test with radial basis functions

The minimum point and its 80 points nearest neighbors were taken to describe the χ^2 function with RBFs:

$$\chi^2(\vec{p}) = \sum_{j=1}^{81} \frac{\omega_j}{\sqrt{\sum_{i=1}^4 \left(\frac{p_i - p_{ij}}{\Delta p_i} \right)^2 + 1}}, \quad (134)$$

where weights ω_j are results of the solution of the linear system of equations:

$$\sum_{j=1}^{81} p_{ij} \omega_j = \chi^2(\vec{p}_i), \quad (135)$$

with p_{ij} being the distance between the vectors \vec{p}_i and \vec{p}_j in the parameter space. Reconstructed parameters for the test case are $T_{\text{eff}} = 5557.83$ K, $\log g = 2.03$ dex, $\xi_t = 1.77$ km s⁻¹ and $\log A = -0.035$ dex.

4.4.3 Test with a quadratic form

the second interpolation method is based on the reconstruction of the underlying χ^2 function by a quadratic form. Again, 80 grid points from the hypercube around the minimum on the grid were considered to fit the quadratic form

$$f(\vec{p}) = \vec{p}^T \cdot A \cdot \vec{p} + B \cdot \vec{p} + c, \quad (136)$$

where A is a symmetric 4×4 matrix, and $B = \{b_1, b_2, b_3, b_4\}$ and c are coefficients. The matrix A has ten independent coefficients. The total amount of unknown parameters to fit is 15. After

finding the coefficients, multidimensional minimization algorithms can be used to determine the minimum of the function. The result of the best fit is $T_{\text{eff}} = 5551 \text{ K}$, $\log g = 2.01 \text{ dex}$, $\xi_t = 1.72 \text{ km s}^{-1}$, and $\log A = -0.002 \text{ dex}$ for the test case.

4.4.4 Test with a sequence of cubic interpolations

The third method is based on using 1D cubic interpolations, splitting the multidimensional interpolation in a sequence of 1D interpolations. The 4D interpolation demands 64 separate 1D interpolation steps. The reconstructed parameters for the test case are $T_{\text{eff}} = 5551 \text{ K}$, $\log g = 2.00 \text{ dex}$, $\xi_t = 1.75 \text{ km s}^{-1}$, and $\log A = -0.045 \text{ dex}$.

Methods 2 and 3 are higher-order methods that work better for regular data and when interpolation values outside the input range are needed. The tests show that the data values are regular enough to make the higher-order methods work better than the lower-order method 1. The third method provided the closest match to the input parameters. Thus, we used the cubic interpolation method.

4.5 Results and discussion

The parameters of the 2D model using the grid of 1D LHD models were recovered for two different regimes of the temporal evolution of the 2D model:

1. EWs for 99 instances in time were computed from the initial time evolution of the 2D model, when convection was the main dynamical driver and pulsations had not set in.
2. EWs for 150 instances were computed when pulsations had set in. They covered six full pulsational periods.

The idea here is that by comparison of the two phases, we might be able to separate effects of convection and pulsation.

4.5.1 The four-parametric case

This is our most general determination of the Cepheid parameters without using additional constraints for fixing parameters. All information deriving from the spectroscopic properties is summarized here by the EWs of the considered lines. Each instance in time (“snapshot”) during the evolution of the 2D model is considered independently. This allows us to achieve an understanding of systematic effects and the quality of the stellar parameter determination as a function of the pulsation phase. The results of the four-parameter fitting when pulsations have set in are shown in the left panel of Fig. 48. There are significant biases between the 2D model

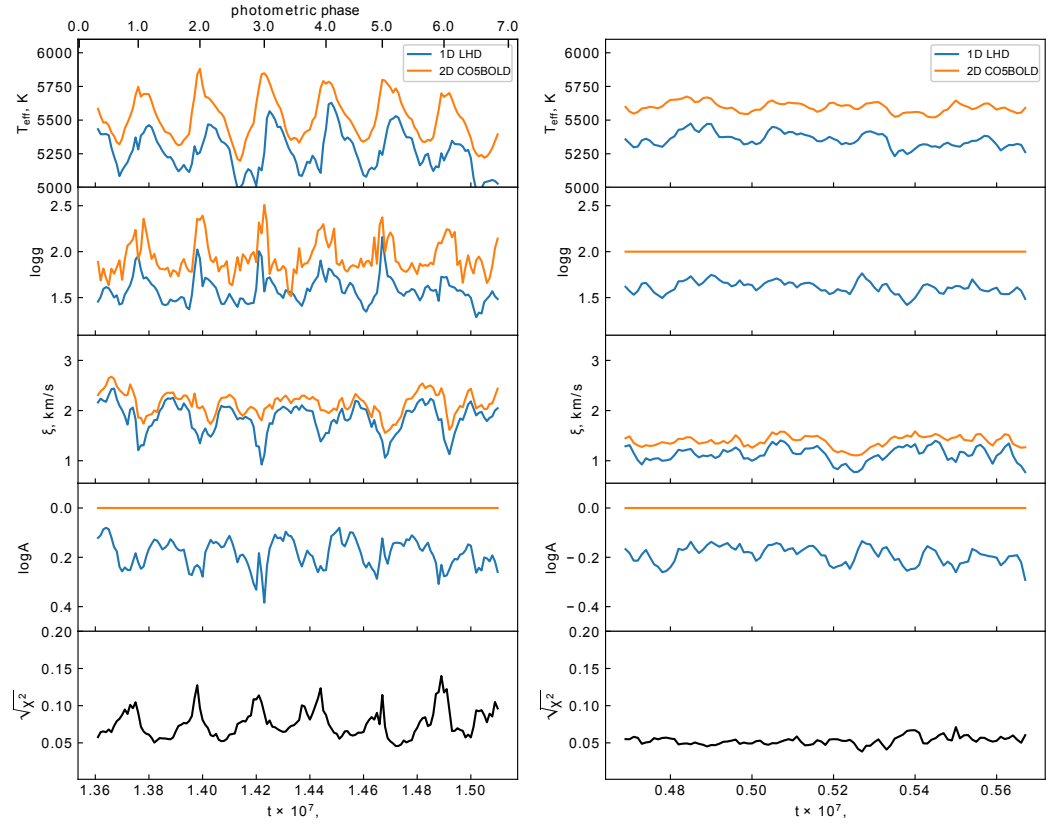


Figure 48: The result of the four-parametric fitting for the pulsating (left panel) and non-pulsating (right panel) regimes. The parameters of the 2D model are shown by orange lines for both regimes. The reconstructed parameters with the 1D LHD grid are shown by blue lines. The relative RMS deviation $\sqrt{\xi^2}$ in line strengths between the 2D and 1D models is shown by a black line.

parameters and the result of the fitting using 1D hydrostatic plane-parallel models. The mean bias in the determination of the effective temperature is $T_{\text{eff}}^{2D} - T_{\text{eff}}^{1D} \approx 250$ K, depending on the pulsation phase. During phases of the maximum compression, it is higher than 400-600 K, whereas it varies in a range from 100 K to 200 K for photometric phases $\phi_{\text{ph}} \approx 0.3 \dots 0.65$, which correspond to the maximum expansion and early contraction stages. Gravity and metallicity exhibit mean biases between 2D and 1D values of roughly 0.35 and 0.2, respectively. The reconstructed microturbulent velocity is slightly lower (by $\approx 0.1 \text{ km s}^{-1}$) than the 2D result, and shows a clear modulation with pulsational phase. We recall that the microturbulent velocity measured in the 2D case is not a result of the standard spectroscopic measurement of ξ_t (see details in Paper I), and neither is our fitting result based on least squares. In view of what to expect during an observational analysis, the bias of the microturbulence should therefore be taken as only indicative.

As stated before, the square root of the χ^2 function in Fig. 48 characterizes the mean relative difference between EWs of the 2D and 1D LHD model. Depending on the photometric phase, this quantity varies from 5 % to 20 %. For the most extreme cases at maximum compression, the difference is the largest.

It might be argued that pulsations mainly disturb the thermal structure of the 2D model, and physical conditions in the line-formation region differ from the hydrostatic case. To check this hypothesis, the fitting was made for the case when pulsations have not set in. The result of the fitting is shown in the right panel of Fig. 48. For this regime, the relative difference in EWs is only 4-7 %, but the mean biases of the stellar parameters are very similar as in the time interval when pulsations have set in. We conclude that the pulsations contribute additional perturbations during the phase of maximum compression, but the main disturber of the thermal structure is convection (see also Paper I for further discussion).

Biases in the determination of stellar parameters for the cases when pulsations have and have not set in are caused by significant differences in the EWs of the 2D model and 1D LHD models. As we remarked above, this is caused by the different thermal structures of these models in the line-formation region. Thermal structures of the mean 2D model, which are the result of horizontally averaging over Rosseland optical depth, and 1D models are shown in Fig. 49. The 1D models were chosen from the grid according to the results of the fitting for the non-pulsating regime, taking the effective temperature to be $T_{\text{eff}} = 5300, 5400$ K, and gravity $\log g = 1.5, 1.7$ dex. Additionally, we plot the 1D LHD model with 2D nominal surface gravity and effective temperature. To simplify the discussion, we only consider the non-pulsating stage of the temporal evolution of the 2D model.

The temporal variation of the horizontally averaged structure of the 2D model is indicated by the light blue region. The photospheric temperature of the 2D model changes as a result of convection. Convective overshoot and downflows produce the bump in the thermal structure at $\log \tau_{\text{R}} = 0$. Convective regions of the 1D LHD models are located below the photosphere, and MLT cannot reproduce this particular thermal profile. We have calculated thermal profiles with different

mixing length parameters, but there are no qualitative improvements. The 1D LHD model with the same effective temperature $T_{\text{eff}} = 5600$ K and gravity $\log g = 2.0$ as the 2D model has approximately the same temperature profile in a range of optical depths from $\log \tau_{\text{R}} = -3$ to $\log \tau_{\text{R}} = -1$. The 2D model has a lower temperature for ≈ 250 K at $\log \tau_{\text{R}} \approx 0$ than the 1D LHD model, however. The fitting reconstructs the photospheric temperature. Because it has the same photospheric temperature, the 1D model has a cooler temperature profile in the line formation regions than the 2D model.

For the EW W of a weak line, the following expression holds (Gray, 1992):

$$W_{\lambda} \sim \int \frac{l(\lambda)}{\kappa(\lambda)} d\lambda, \quad (137)$$

where l and κ are the line and continuous absorption coefficients, respectively. For the range of the effective temperature of the 2D model between 5200 K and 5800 K, the negative hydrogen ion H^- is the dominant source of continuous opacity, and it is very sensitive to temperature. Iron is mostly ionized in this temperature range. Thus, neutral iron is a minority species, and its EWs increase with a decrease in effective temperature because the H^- opacity drops (Eq. 137). However, the behavior of singly-ionized iron EWs as a function of temperature is opposite to that of neutral iron. For any snapshot of the non-pulsating sequence, we can calculate EWs of the 1D LHD model taking the effective temperature, surface gravity, microturbulent velocity, and metallicity of the 2D model. Our calculation shows a mean relative difference of 13 % between the 2D and 1D model EWs because the photospheric regions of $\log \tau_{\text{R}} \sim 0$ in the 2D model are cooler than in the 1D LHD model. Specifically, (i) the 1D LHD model EWs of Fe I lines $W_{\text{Fe I}}^{1\text{D}}$ are lower than $W_{\text{Fe I}}^{2\text{D}}$, $W_{\text{Fe I}}^{1\text{D}} < W_{\text{Fe I}}^{2\text{D}}$, and (ii) the EWs of the Fe II lines in the 1D model are larger than the 2D model EWs, $W_{\text{Fe II}}^{1\text{D}} > W_{\text{Fe II}}^{2\text{D}}$.

From a physical point of view, EWs of Fe I lines are most sensitive to changes of the effective temperature, and rather insensitive to changes of the gravity. However, EWs of Fe II lines have the opposite behavior: they are sensitive to changes of the gravity, and less sensitive to changes of the temperature. So, in a first qualitative fitting step, one has to decrease the effective temperature and surface gravity of the 1D LHD model to transform (i) and (ii) toward similar differences in relative EWs $(W^{2\text{D}} - W^{1\text{D}})/W^{2\text{D}}$ for all ionization stages. The procedure increases EWs of the 1D LHD model with respect to $W^{2\text{D}}$. As a result, one has to decrease the metallicity to reduce the difference $(W^{2\text{D}} - W^{1\text{D}})$ in a second step. It leads to a lower metallicity in the fit for the pulsating as well as non-pulsating phases.

4.5.2 The three-parametric case

In an observational analysis, the dimensionality of the parameter space is typically reduced using additional information. Gray and Johanson (1991) developed a method for determining the effective temperature using the line depth ratios of pairs of weak lines of the same chemical

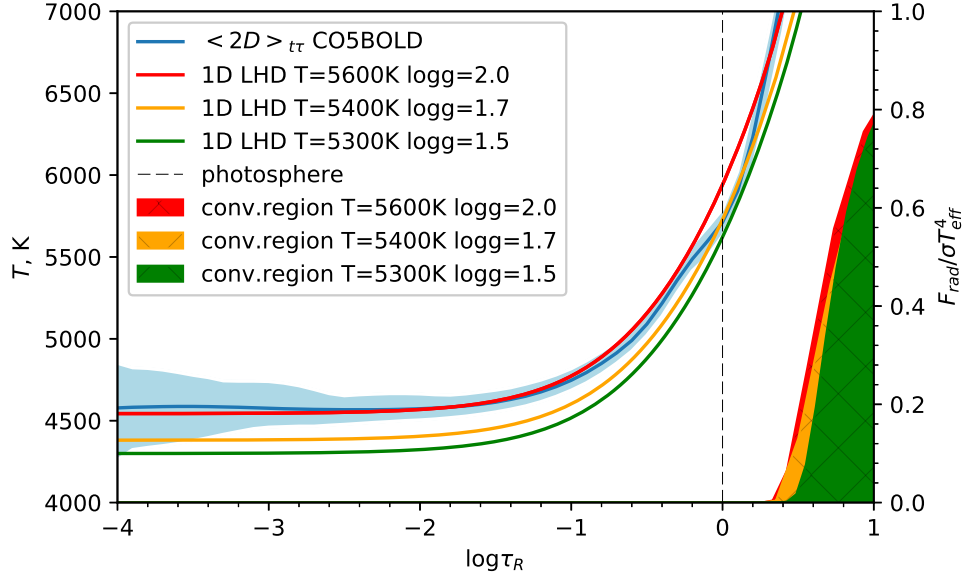


Figure 49: Comparison of thermal structures of the horizontally (on surfaces of constant optical depth) averaged 2D model 1D models for the case when pulsations have not set in. The mean 2D thermal structure varies during 99 instances in time within the light-blue region. The temporally averaged 2D profile is shown in blue color.

element with two different excitation potentials for G and K dwarfs. These ratios are sensitive to the temperature variation and independent of metallicity effects for weak lines (Gray, 1994). Kovtyukh and Gorlova (2000) extended this method to derive precise temperatures of classical Cepheids and yellow supergiants with 10-15 K internal uncertainty using a calibration of the line depth ratio versus effective temperature for 32 line pairs. Andrievsky et al. (2002b); Lemasle et al. (2007); Luck et al. (2011) used this calibration or the updated version (Kovtyukh, 2007) to derive the effective temperatures of Galactic Cepheids.

The surface gravity can be estimated through the condition of the ionization balance, but for this, the correct effective temperature is required because the EW is quite sensitive to temperature changes. Now we assume the effective temperature to be known, and set to the value of the 2D model for each particular instance in time. The effective temperature being fixed, we estimate the three remaining parameters. One-dimensional EWs were interpolated in the $\log g$ - ξ_t - $\log A$ space for the fixed effective temperature. The results of the three-parametric fitting for the non-pulsating and pulsating stages of the temporal evolution are shown in the right and left panels of Fig. 50, respectively. The gravity estimate in the three-parameter fitting is based on the ionization balance, which is hidden in the comparison of EWs of Fe I and Fe II lines. In the range of effective temperatures of the 2D model, most of the iron is in the singly-ionized state. Weak lines of Fe I are insensitive to pressure changes and, thus, to variations of the effective gravity. Conversely, singly-ionized iron is pressure sensitive because of the opacity change in the negative hydrogen

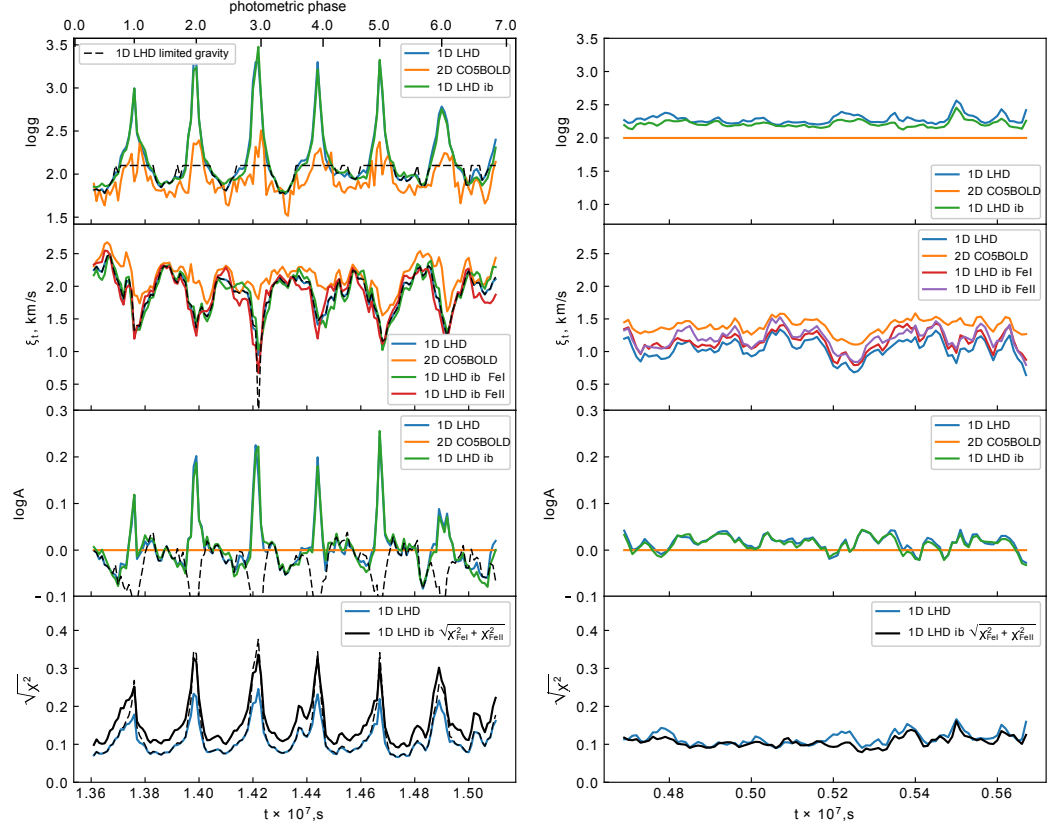


Figure 50: The result of the three-parametric fitting for the pulsating (left panel) and non-pulsating (right panel) regimes. The parameters of the 2D model are shown by orange lines for both regimes. The reconstructed parameters with the direct three-parametric fitting using the 1D LHD grid are shown by blue lines. Results using the ionization balance are shown by green, brown and solid black lines. For the pulsating regime the result of the experiment with a gravity limit for the maximum compression phase is shown by the dashed black line. The relative RMS deviation $\sqrt{\chi^2}$ in line strengths between the 2D and 1D models is shown by the solid blue and black lines for the direct three-parametric fitting and fitting using the ionization balance condition, respectively.

ion, which is sensitive to the electron pressure, giving an overall dependence (Gray, 1992)

$$W_{\text{Fe II}} \sim g^{-\frac{1}{3}}. \quad (138)$$

In addition to the simultaneous fit in all three parameters, we also derived the gravity by enforcing ionization balance. For each instance in time, we considered a two-parameter fit $\{\xi_t, \log A\}$ of the Fe I and Fe II lines separately, where the gravity was varied on the grid between 0.7...3.5 dex. The estimation of the surface gravity using the ionization balance condition was based on deriving the same abundance for Fe I and Fe II. Figure 50 shows that the results of the fit using the ionization balance condition and the direct fit of all three parameters are in good agreement.

In comparison to the four-parameter case, the reconstructed microturbulent velocity is very

similar and consequently shows the same bias of $\approx -0.1 \text{ km s}^{-1}$. The average microturbulent velocity estimated from the ionization balance coincides with the result of the full three-parameter fit for the pulsating and non-pulsating regimes. The metallicities derived for the non-pulsating regime closely correspond to the input value of the 2D model. The convection effect leads to a small variation in $\log A$ with time. It ranges between -0.03 and 0.04 dex.

For the regime when pulsations have set in, there is a deviation 0.25 dex in metallicity for the photometric phase with the maximum compression. Just after the maximum compression phase, there is a time interval exhibiting the smallest offset in metallicity stretching in the photometric phase between $\phi_{\text{ph}} \approx 0.3 \dots 0.65$. From a physical point of view, this photometric phase coincides with the times of maximum expansion and subsequent start of compression. During this period, the atmosphere is in a levitating state, and convection and its disturbances of the thermal structure are not as strong as during maximum compression. The atmosphere is roughly in hydrostatic equilibrium, and the 1D models reasonably reproduce the mean thermal structure of the line formation region of the 2D model. This is shown in Fig. 51 for the photometric phases 0.25 and 0.6. It leads to a correct reconstruction of the metallicity with a 10 % relative difference between $W^{1\text{D}}$ and $W^{2\text{D}}$.

For the phase of maximum compression, the thermal structures of 1D and mean 2D model in line formation regions differ appreciably despite the fact that they have the same effective temperatures. At optical depths $\log \tau_{\text{R}} \approx -1.3$, the mean 2D structure is 400 K cooler than the fitted 1D structure. The 2D structure has a rather low resolution of the optical depth scale around $\tau_{\text{R}} \sim 1$ and exhibits steep temperature gradients. For the 2D model, the horizontal averaging on surfaces of constant optical depth yields lower temperatures for the photospheric regions. However, experiments with increased resolution of the optical depth scale using interpolation and subsequent horizontal averaging did not yield a qualitative change of the mean 2D structure. This suggests that the horizontal inhomogeneities produced by convection and the horizontal averaging leads to the lower photospheric temperatures in comparison to 1D. In addition, the large changes in opacities on the coarse numerical grid and the steep temperature gradients might contribute as well. This has to be tested in future simulations with higher numerical resolution.

As we described above, the Fe I lines are insensitive to the surface gravity. A high effective gravity of the 2D model leads to a decrease in Fe II EWs $W_{\text{Fe II}}^{2\text{D}}$ according to Eq. (138). For the spectral synthesis with 1D LHD models of fixed effective temperature, the surface gravity has to be increased in a first qualitative fitting step to obtain the relative difference $(W_{\text{Fe II}}^{2\text{D}} - W_{\text{Fe II}}^{1\text{D}}) / W_{\text{Fe II}}^{2\text{D}}$ similar to Fe I. Owing to different thermal structures of the line formation regions, 1D EWs are smaller than the corresponding values of the 2D model. As a second step, the iron abundance therefore has to be increased to minimize the differences in EW. This leads to a positive bias for the metallicity during the phase of maximum compression and to high values of the reconstructed gravity.

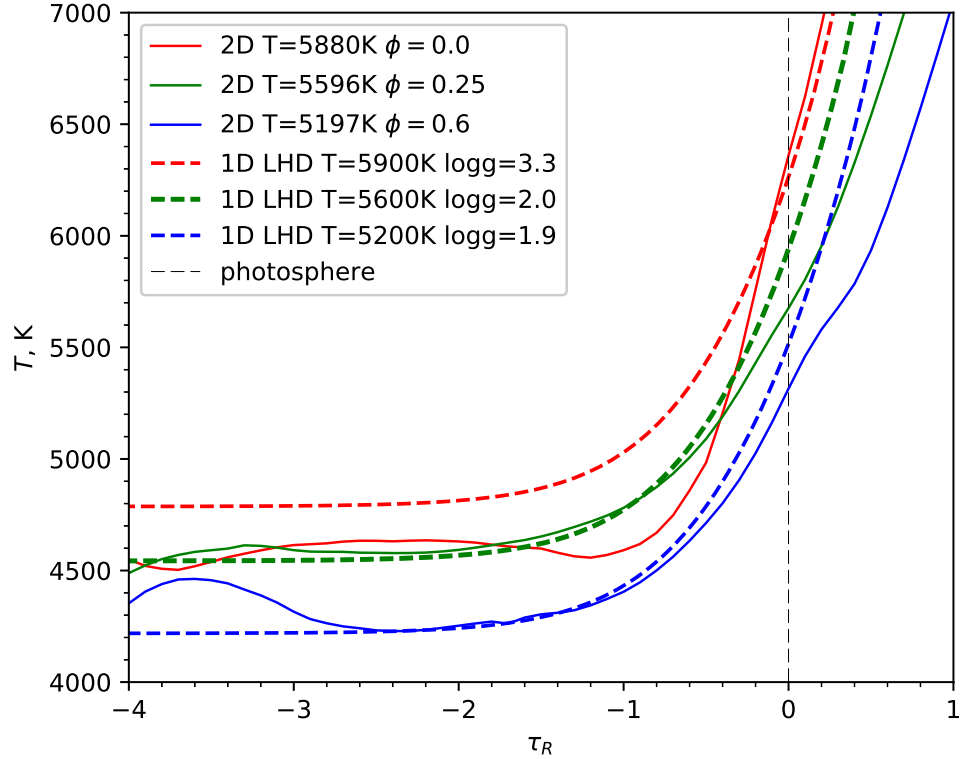


Figure 51: Comparison of thermal structures of LHD models with the mean temperature profiles (average over optical depth surfaces) of the two-dimensional model for several photometric phases. τ_R is the Rosseland optical depth.

To understand the effect of the gravity on the metallicity bias during the phase of maximum compression, we performed an additional test. For this phase, the gravity was limited to $\log g = 2.1$ or less. The results of the fitting are shown for the case when pulsations have set in in the left panel of Fig. 50. For a better fitting of the 2D EWs, the metallicity or microturbulent velocity can be changed. However, EWs of weak lines are insensitive to the change in microturbulent velocity. Thus, to reduce the difference ($W^{2D} - W^{1D}$), the metallicity has to be decreased.

4.5.3 The two-parametric case

We now assume that the effective temperature and the effective gravitational acceleration are known from independent considerations. We take the effective temperature and gravity of the 2D model and interpolate EWs calculated with the grid of 1D models in ξ_t - $\log A$ space. In this two-parameter case, χ^2 is a function of the microturbulent velocity and metallicity alone.

Again, we performed the two-parameter fit for the pulsating and non-pulsating stages of the temporal evolution of the 2D model. The results are shown in the left and right panels of Fig. 52. The effective gravity of the 2D model for the pulsating case is lower than the values of the three-

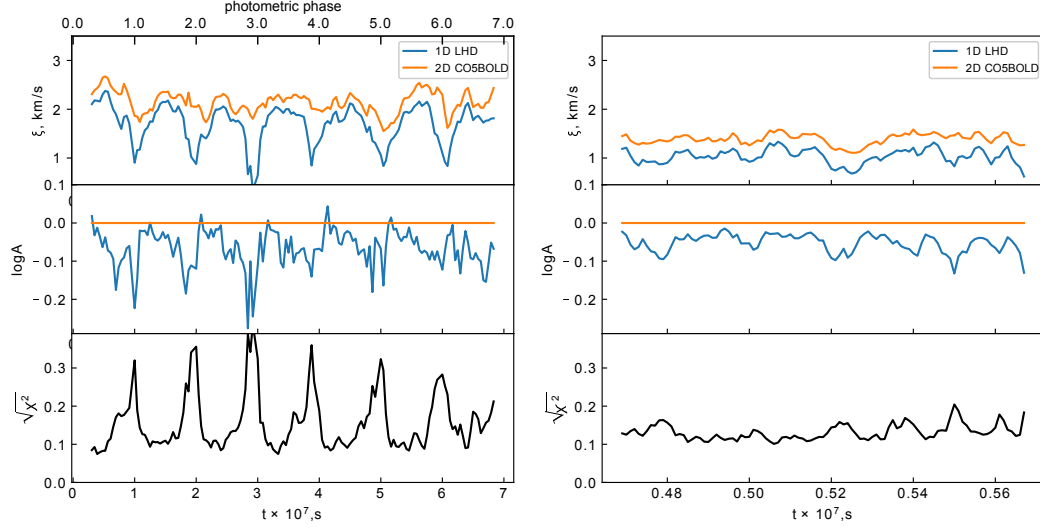


Figure 52: The result of the two-parametric fitting for the pulsating (left panel) and non-pulsating (right panel) regimes. The parameters of the 2D model are shown by orange lines for both regimes. The reconstructed parameters with the 1D LHD grid are shown by blue lines. The relative RMS deviation $\sqrt{\chi^2}$ in line strengths between the 2D and 1D models is shown by black line.

parameter fitting. As we showed in the previous subsection, the lower gravity leads to a negative bias of the metallicity for most phases, except for the phase of the maximum expansion and start of the contraction. For this phase, the result of the fitting shows a perfect reconstruction of the metallicity because the atmosphere is close to hydrostatic conditions, and the 1D model can reproduce the thermal structure (see Fig. 49). When pulsations have not set in, the reconstructed mean metallicity is $\log A^{1D} = -0.05$ dex, which is lower than the result of the three-parameter fit because the gravity is fixed to $\log g = 2$. According to Eq. (138), this leads on average to higher EWs in 1D, and hence to a slight decrease of the metallicity.

Owing to the smaller number of free parameters in the two-parameter case, the $\sqrt{\chi^2}$ value increases to a level of $\approx 10\%$, except for the phases of maximum compression. When the analysis of the spectra is performed by taking some random photometric phase, a negative metallicity bias of ≈ 0.06 dex is obtained on average.

4.5.4 Connection between abundance and equivalent width fitting

We minimized a χ^2 function of up to four parameters, which is the sum of relative differences of the individual line EWs between the 2D model and 1D models. Here we wish to provide arguments as to why the fitting in EW does not give a qualitatively different result when the fitting of line-by-line abundances is considered. With fixed effective temperature and gravity, we reconstructed the thermal structure of the line formation regions. The minimization of the mean difference of W^{2D} and W^{1D} EWs is equal to the minimization of the mean abundance differences $A^{2D} - A^{1D}$. This

can be shown analytically for weak lines. For the two-parameter case, when χ^2 is a function of the microturbulent velocity and abundance, we obtain

$$\chi^2(A, \xi_t) = \frac{1}{N} \sum_i^N \left[\frac{W_i^{2D} - W_i^{1D}(A, \xi_t)}{f \cdot \sigma_{W,i}} \right]^2, \quad (139)$$

where N is the number of lines. To first order, the difference in EWs of the line i between the 2D 1D model can be represented by the Taylor expansion

$$W_i^{2D} - W_i^{1D} \approx \frac{\partial W_i}{\partial \xi_t} \cdot (\xi_{t,i}^{2D} - \xi_{t,i}^{1D}) + \frac{\partial W_i}{\partial A} \cdot (A_i^{2D} - A_i^{1D}) + \dots \quad (140)$$

The uncertainty $\sigma_{W,i}$ in the EW is related with uncertainties in the abundance $\sigma_{A,i}$ and microturbulent velocity σ_{ξ_t}

$$\sigma_{W,i} = \sqrt{\left[\frac{\partial W}{\partial \xi_t} \right]^2 \sigma_{\xi_t}^2 + \left[\frac{\partial W}{\partial A} \right]^2 \sigma_{A,i}^2}. \quad (141)$$

Weak lines are insensitive to change in ξ_t . Inserting the condition $\frac{\partial W}{\partial \xi_t} = 0$ into Eqs. (141) and (140), we can modify Eq. (139)

$$\chi^2 \approx \frac{1}{N} \sum_i^N \left[\frac{A_i^{2D} - A_i^{1D}}{f \cdot \sigma_{A,i}} \right]^2, \quad (142)$$

which shows that the minimization of the difference of EWs is equal to minimizing the difference in abundance between the 1D grid and 2D model.

4.5.5 Comparison of equivalent widths

Using the curve of growths, we can transform the difference in EWs $W^{2D} - W^{1D}$ into an abundance correction for each individual line. The individual abundance corrections as a function of the line strength and photometric phase are shown in Fig. 53 for the three-parameter case. As expected, the smallest abundance corrections correspond to photometric phases $\phi_{ph} \approx 0.3 \dots 0.65$. Generally, Fe I lines have larger abundance corrections than Fe II lines. Additionally, within the same ionization stage, the abundance corrections become smaller with increasing excitation potential.

4.6 Summary

We have determined the stellar parameters (effective temperature, gravity, microturbulent velocity, and metallicity), of a 2D dynamical Cepheid model that was calculated with the CO5BOLD code and has been presented in Chapter 3. We took EWs based on the 2D model as observational data and calculated a grid of the 1D plane-parallel hydrostatic model atmospheres for two regimes of the temporal evolution of the 2D model. We performed the analysis for three different cases:

1. A four-parameter case, where χ^2 is a function of T_{eff} , $\log g$, ξ_t , and A . All reconstructed

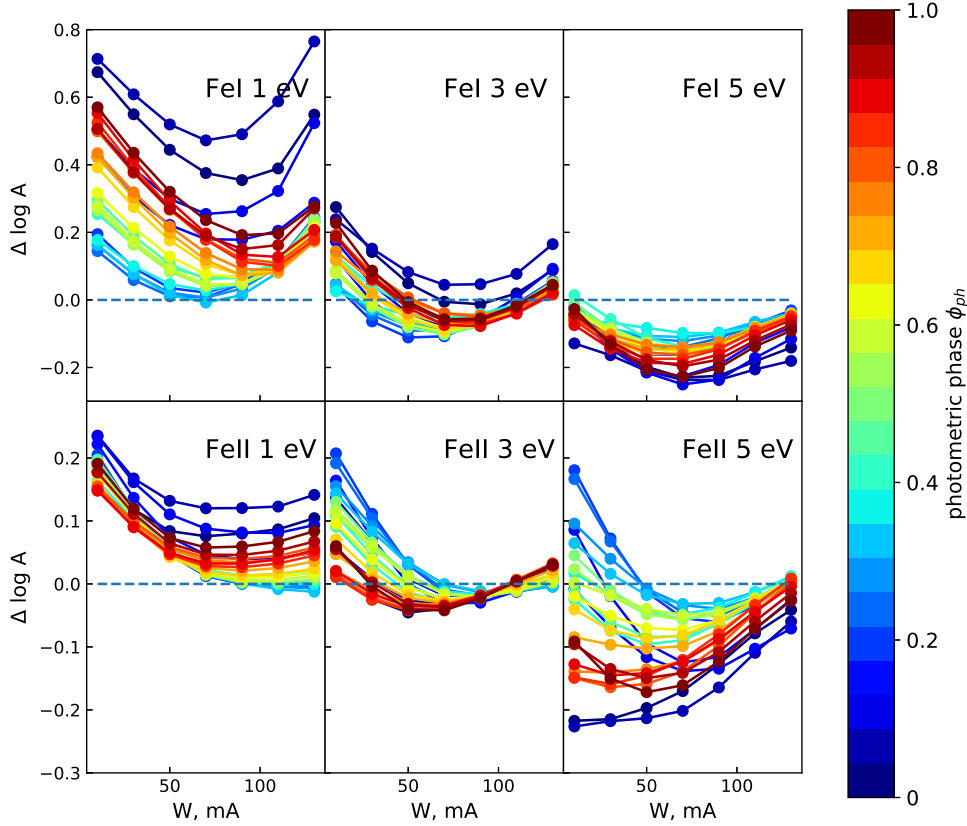


Figure 53: The abundance corrections for individual lines for the best fitting 1D models as a function of line strength and photometric phase.

parameters are biased toward lower values than in the 2D model snapshots, and they are on average largely independent of the pulsations. The bias in the metallicity determination is ≈ -0.2 dex.

2. A three-parameter case, where the T_{eff} is fixed to the 2D value. χ^2 is a function of $\log g$, ξ_t , and $\log A$. Stellar parameters are determined with (i) direct three-parameter fitting, and (ii) using the condition of ionization balance. The gravity estimate is higher than the effective 2D gravity for the pulsating and non-pulsating regimes. For the non-pulsating regime, the metallicity reconstruction agrees for all instances in time, whereas when pulsations have set in, only the photometric phases $\phi_{\text{ph}} \approx 0.3 \dots 0.65$ show a slightly biased metallicity estimate.
3. A two-parameter case, where χ^2 is a function of ξ_t and $\log A$. The metallicity estimate behaves qualitatively similar to case (2).

One-dimensional hydrostatic plane-parallel stellar model atmospheres employing different MLT formulations generally cannot reproduce the mean thermal structure of the 2D model for the whole range of optical depths. In particular, the temperature at optical depth unity of the 1D mod-

els is typically higher than for the mean 2D model. To avoid systematic biases in the determination of stellar parameters of Cepheids with standard model atmospheres, we recommend analyzing spectra taken during photometric phases $\phi_{\text{ph}} \approx 0.3 \dots 0.65$.

5 CONCLUSIONS

5.1 Summary

The work presented in this thesis is concerning the one-dimensional modeling of pulsating stellar atmospheres, mainly atmospheres of classical Cepheids, and the spectroscopic investigation of a two-dimensional hydrodynamic Cepheid model. I describe how I constructed one-dimensional pulsating stellar model atmospheres with a code named LHD (for Lagrangian HydroDynamics), as well as report results obtained by applying the code to the analysis of spectra of the classical Cepheid KQ Scorpii. I have contributed the results to a project concerning the study of metallicity gradients in the Galaxy based on the analysis of Cepheids. The project is led by Dr. Laura Inno and Dr. Maria Bergemann, and a paper containing also my contribution is in preparation. The results related to the spectroscopic investigation of the two-dimensional Cepheid model have been published (Vasilyev et al., 2017a) and recently accepted for publication (Vasilyev et al., 2017b) in the *Astronomy and Astrophysics Journal*.

In Chapter 2 I discuss the problem of how one constructs one-dimensional pulsating Cepheid atmospheres. I formulate the basic equations which describe the dynamics of the atmosphere and govern the change of the energy due to effects of the dynamics, as well as transport by radiation and convection. I discuss boundary conditions and the excitation of pulsations by two different approaches: oscillations enforced by a piston placed at the bottom of the model atmosphere and free oscillations excited by setting an initial perturbations. Concerning the convective energy transport I go in some detail into Mixing Length Theory and Stellingwerf's non-local time-dependent theory of convection. This includes an investigation of the stability of the numerical scheme that I implemented into the LHD code for Stellingwerf's convection model. I apply the code by calculating a model of the Cepheid KQ Sco, and perform a spectral synthesis of iron lines in order to understand the behavior of the microturbulent velocity in the particular Cepheid. I show that pulsations do not produce the velocity gradient within the line formation regions necessary to explain the the observed level of microturbulence.

In Chapters 3 and 4 I perform a first investigation of spectroscopic properties of a two-dimensional time-dependent Cepheid model focusing on an investigation of the validity of the quasi-static approximation in the context of pulsating stars. This quasi-static approach has theoretically not been validated before. Taking the 2D model, I perform extensive spectral syntheses for a set of artificial iron lines in local thermodynamic equilibrium to systematically study effects of line strength, ionization stage, and excitation potential.

In Chapters 3 I summarize results with estimation of the microturbulent velocity, line asymmetry, projection factor, and Doppler shifts. The microturbulent velocity, averaged over all lines, depends on the pulsational phase and varies between 1.5 and 2.7 km s^{-1} . The derived projection factor lies

between 1.23 and 1.27, which agrees with observational results. I have found, that the residual line-of-sight velocity of Galactic Cepheids that is of the order -1 km s^{-1} , known for over last eighty years in the literature as the K-term, is the result of the convective blueshift.

In Chapter 4 I describe the spectroscopic determination of the effective temperature T_{eff} , surface gravity $\log g$, microturbulent velocity ξ_t , and iron abundance $\log A$ with a pre-calculated grid of 1D hydrostatic plane-parallel models taking the equivalent widths calculated with the 2D model as (synthetic) observations. It allows me to investigate systematic effects and biases of derived parameters as a function of the pulsational phase. I show that the hydrostatic 1D model atmospheres can provide unbiased estimates of stellar parameters and abundances of Cepheid variables for particular phases of their pulsations.

Shortly summarizing my dissertation I can conclude, that the main result of the work is a change of perspective in the context of spectroscopic investigations of Cepheids toward a greater importance of convection than assumed previously.

5.2 Future plans

The one-dimensional (1D) dynamical atmospheres I calculated in plane-parallel approximation. In order to construct more realistic models one should modify the LHD code to account for the more appropriate spherical-symmetric geometry of the problem. The energy and dynamical equation as well as the radiation and convective transport equations need to be modified. Additionally, the question of the stability of the new numerical scheme has to be investigated. Since calculations of 1D models are not as time-consuming process as they are in the case of multi-dimensional stellar model atmospheres, one could calculate 1D models for a wide range of parameters, i.e., temperatures, surface gravities, metallicities, amplitudes of the radial velocity, and periods of pulsation in order to investigate spectroscopic and pulsational properties. An interesting possibility would also be the construction of 1D pulsating stellar atmosphere models for variables of shorter period – having here RR Lyrae stars in mind – which would allow one to investigate effects of shock formation and propagation on the line formation. One potential application would be the derivation of the helium abundance in RR Lyrae stars which is particularly interesting since they are old, metal-poor Population II stars.

Concerning multidimensional models of pulsating stellar atmospheres, the present investigation was based on a single dynamical model of a Cepheid restricted to two spatial dimensions. A comprehensive theoretical investigation of the line formation in the atmospheres of Cepheid variables would require additional models, in particular of lower surface gravity corresponding to longer pulsational periods. The inclusion of effects of sphericity, and an investigation of departures from local thermodynamic equilibrium are desirable future improvement on the side of dynamical multi-dimensional modeling. One problem, which I would like to start to investigate with the

existing 2D model, is the question of departures from local thermodynamic equilibrium for various pulsational phases.

6 SUPPLEMENTARY MATERIAL

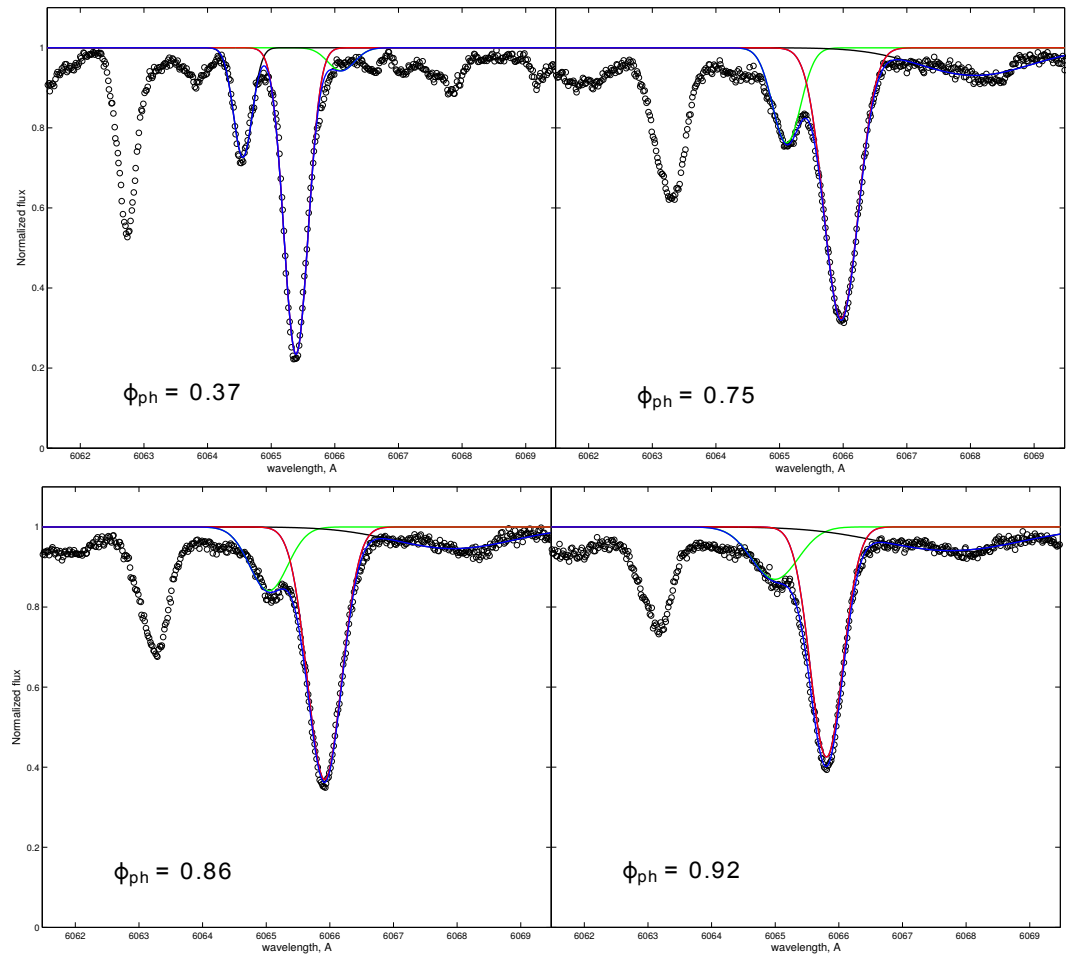


Figure 54: Gaussian fit of the Fe I 6065 Å line and blends in order to derive the equivalent width of Fe I line.

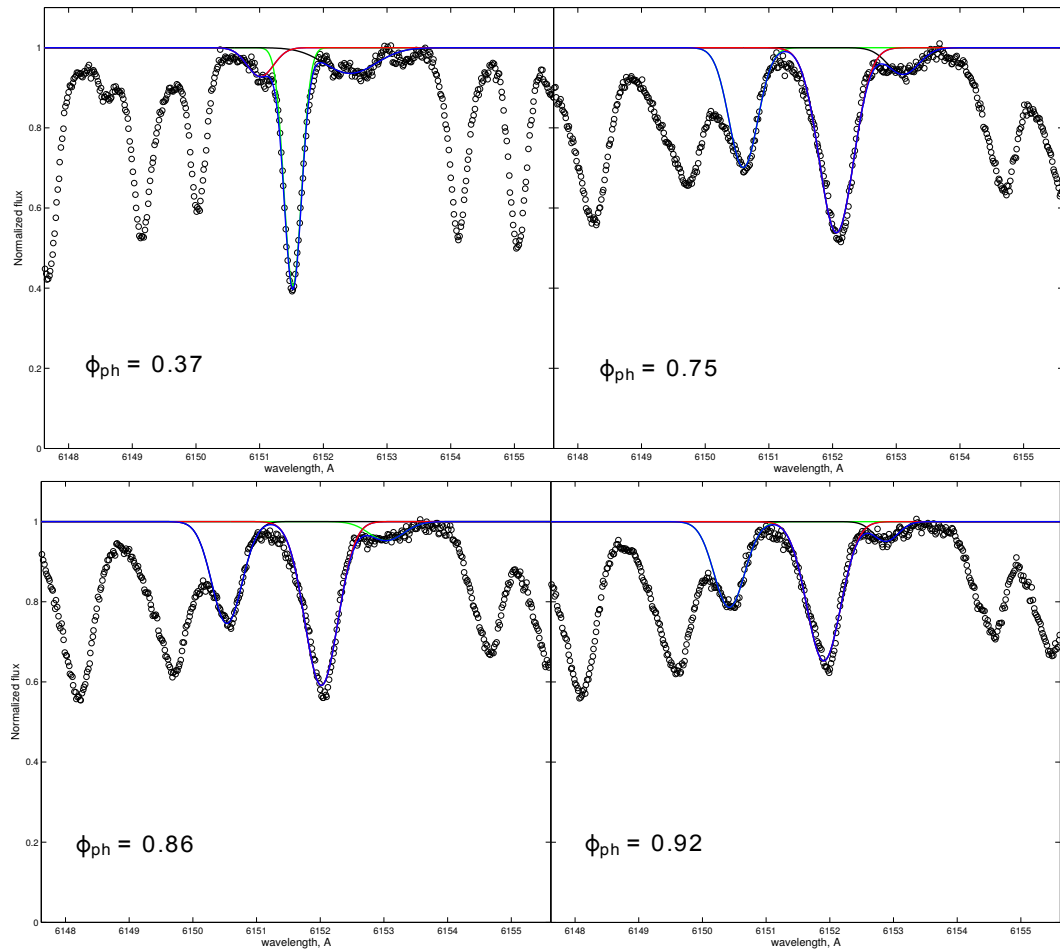


Figure 55: Gaussian fit of the Fe I 6151 Å line and blends in order to derive the equivalent width of Fe I line.

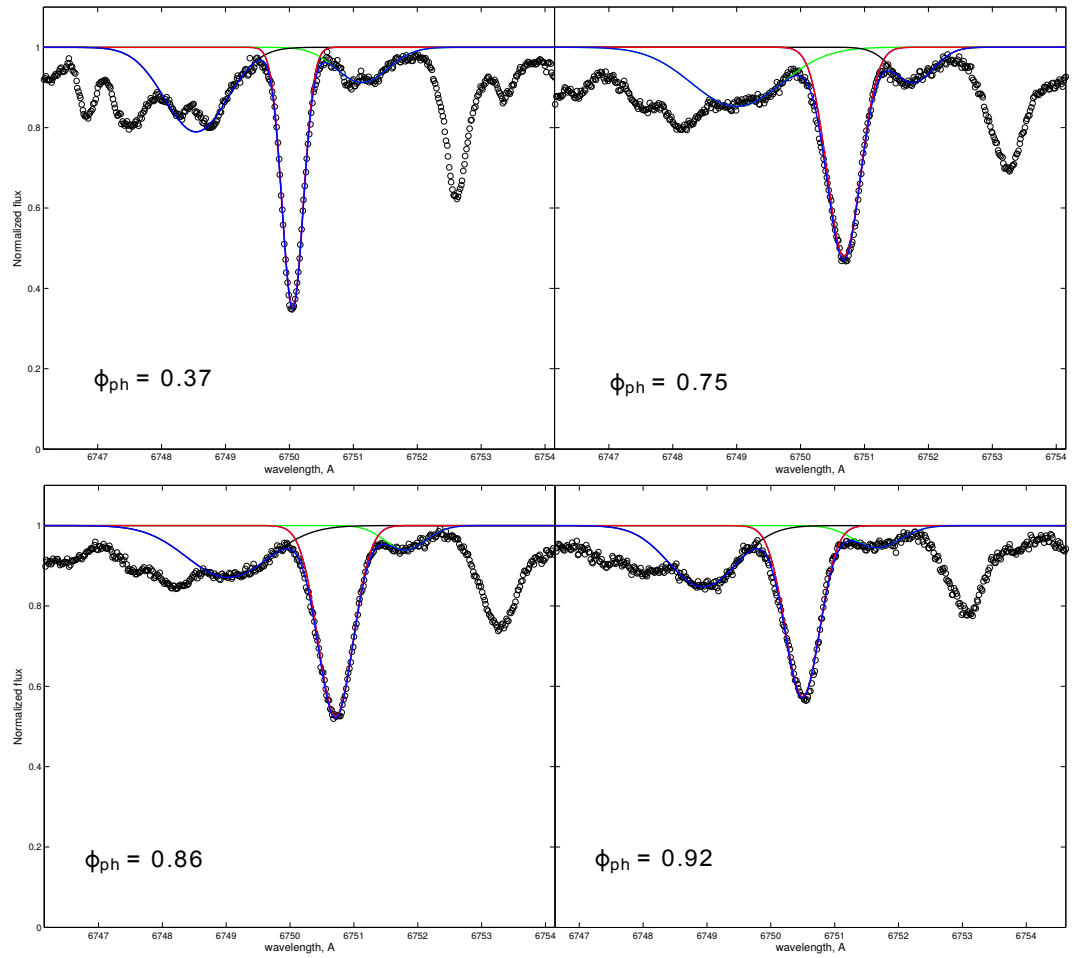


Figure 56: Gaussian fit of the Fe I 6750 Å line and blends in order to derive the equivalent width of Fe I line

7 LIST OF ABBREVIATIONS

CMB	Cosmic Microwave Background
BBN	Big Bang Nucleosynthesis
GCR	Galactic Cosmic Rays
ISM	interstellar medium
APOGEE	Apache Point Observatory Galactic Evolution Experiment
GALAH	Galactic Archaeology with HERMES
LTE	local thermodynamic equilibrium
LM	Luminosity-Mass
PA	Period-Age
PAC	Period-Age-Color
PL	Period-Luminosity
PLC	Period-Luminosity-Color
PLM	Period-Luminosity-Mass
LHD	Lagrangian HydroDynamics
MLT	Mixing Length Theory
UVES	Ultraviolet and Visual Echelle Spectrograph
VLT	Very Large Telescope
EW	Equivalent width

8 BIBLIOGRAPHY OF OWN PUBLICATIONS

The following publications have been used:

1. **Vasilyev, V.**, Ludwig, H.-G., Freytag, B., Lemasle, B., Marconi, M., "Spectroscopic properties of a two-dimensional time-dependent Cepheid model I. Description and validation of the model", 2017, *Astronomy and Astrophysics*, 606, A140
2. **Vasilyev, V.**, Ludwig, H.-G., Freytag, B., Lemasle, B., Marconi, M., "Spectroscopic properties of a two-dimensional time-dependent Cepheid model II. Determination of stellar parameters and abundances", 2017, accepted for publication in *Astronomy and Astrophysics*

The following publications have not been used in this thesis:

3. M. S. Pshirkov, **V. Vasilyev**, and K. A. Postnov, "Evidence of Fermi bubbles around M31", *MNRAS*, 459, pp. L76–L80, June 2016.
4. M. Pshirkov, K. Postnov, and **V. Vasilyev**, "Gamma-ray halo around the M31 galaxy as seen by the Fermi LAT", in 34th International Cosmic Ray Conference (ICRC2015), vol. 34 of International Cosmic Ray Conference, p. 867, July 2015.
5. P. S. Medvedev, S. N. Fabrika, **V. Vasilyev**, V. P. Goranskij, and E. A. Barsukova, "Superbroad component in emission lines of SS 433", *Astronomy Letters*, 39, pp. 826–843, Dec. 2013.

REFERENCES

- B. P. Abbott, R. Abbott, T. D. Abbott, F. Acernese, K. Ackley, C. Adams, T. Adams, P. Addesso, R. X. Adhikari, V. B. Adya, and et al. Multi-messenger Observations of a Binary Neutron Star Merger. *Astrophysical Journal, Letters*, 848:L12, October 2017. doi: 10.3847/2041-8213/aa91c9.
- C. Allende Prieto, S. R. Majewski, R. Schiavon, K. Cunha, P. Frinchaboy, J. Holtzman, K. Johnston, M. Shetrone, M. Skrutskie, V. Smith, and J. Wilson. APOGEE: The Apache Point Observatory Galactic Evolution Experiment. *Astronomische Nachrichten*, 329:1018, December 2008. doi: 10.1002/asna.200811080.
- R. I. Anderson. Discovery of Cycle-to-cycle Modulated Spectral Line Variability and Velocity Gradients in Long-period Cepheids. *Monthly Notices of the RAS*, 463:1707–1723, December 2016. doi: 10.1093/mnras/stw2093.
- R. I. Anderson, S. Ekström, C. Georgy, G. Meynet, N. Mowlavi, and L. Eyer. On the effect of rotation on populations of classical Cepheids. I. Predictions at solar metallicity. *Astronomy and Astrophysics*, 564:A100, April 2014. doi: 10.1051/0004-6361/201322988.
- R. I. Anderson, H. Saio, S. Ekström, C. Georgy, and G. Meynet. On the effect of rotation on populations of classical Cepheids. II. Pulsation analysis for metallicities 0.014, 0.006, and 0.002. *Astronomy and Astrophysics*, 591:A8, June 2016. doi: 10.1051/0004-6361/201528031.
- S. M. Andrievsky, V. V. Kovtyukh, R. E. Luck, J. R. D. Lepine, D. Bersier, W. J. Maciel, B. Barbuy, V. G. Klochkova, V. E. Panchuk, and R. U. Karpishek. VizieR Online Data Catalog: Galactic Cepheid abundances (Andrievsky+, 2002). *VizieR Online Data Catalog*, 338, November 2001.
- S. M. Andrievsky, D. Bersier, V. V. Kovtyukh, R. E. Luck, W. J. Maciel, J. R. D. Lépine, and Y. V. Beletsky. Using Cepheids to determine the galactic abundance gradient. II. Towards the galactic center. *Astronomy and Astrophysics*, 384:140–144, March 2002a. doi: 10.1051/0004-6361:20020016.
- S. M. Andrievsky, V. V. Kovtyukh, R. E. Luck, J. R. D. Lépine, D. Bersier, W. J. Maciel, B. Barbuy, V. G. Klochkova, V. E. Panchuk, and R. U. Karpishek. Using Cepheids to determine the galactic abundance gradient. I. The solar neighbourhood. *Astronomy and Astrophysics*, 381:32–50, January 2002b. doi: 10.1051/0004-6361:20011488.
- S. M. Andrievsky, V. V. Kovtyukh, R. E. Luck, J. R. D. Lepine, W. J. Maciel, and Y. V. Beletsky. VizieR Online Data Catalog: Galactic abundance gradient. III. (Andrievsky+, 2002). *VizieR Online Data Catalog*, 339, September 2002c.
- S. M. Andrievsky, R. E. Luck, P. Martin, and J. R. D. Lépine. The Galactic abundance gradient from Cepheids. V. Transition zone between 10 and 11 kpc. *Astronomy and Astrophysics*, 413:159–172, January 2004. doi: 10.1051/0004-6361:20031528.

-
- S. M. Andrievsky, R. E. Luck, and V. V. Kovtyukh. Phase-dependent Variation of the Fundamental Parameters of Cepheids. III. Periods between 3 and 6 Days. *Astronomical Journal*, 130:1880–1889, October 2005. doi: 10.1086/444541.
- S. M. Andrievsky, R. P. Martin, V. V. Kovtyukh, S. A. Korotin, and J. R. D. Lépine. Oxygen, α -element and iron abundance distributions in the inner part of the Galactic thin disc - II. *Monthly Notices of the RAS*, 461:4256–4259, October 2016. doi: 10.1093/mnras/stw1631.
- M. Asplund, N. Grevesse, A. J. Sauval, and P. Scott. The Chemical Composition of the Sun. *Annual Review of Astron and Astrophys*, 47:481–522, September 2009. doi: 10.1146/annurev.astro.46.060407.145222.
- W. Baade. Über eine Möglichkeit, die Pulsationstheorie der δ Cephei-Veränderlichen zu prüfen. *Astronomische Nachrichten*, 228:359, October 1926. doi: 10.1002/asna.19262282003.
- N. Baker and R. Kippenhahn. The Pulsations of Models of Delta Cephei Stars. II. *Astrophysical Journal*, 142:868, October 1965. doi: 10.1086/148359.
- T. G. Barnes and D. S. Evans. Stellar angular diameters and visual surface brightness - I. Late spectral types. *Monthly Notices of the RAS*, 174:489–502, March 1976. doi: 10.1093/mnras/174.3.489.
- W. Benz. An Introduction to Computational Methods in Hydrodynamics. In C. B. De Loore, editor, *Late Stages of Stellar Evolution. Computational Methods in Astrophysical Hydrodynamics*, volume 373 of *Lecture Notes in Physics*, Berlin Springer Verlag, page 258, 1991. doi: 10.1007/BFb0032282.
- E. Böhm-Vitense. Über die Wasserstoffkonvektionszone in Sternen verschiedener Effektivtemperaturen und Leuchtkräfte. Mit 5 Textabbildungen. *Zeitschrift fuer Astrophysik*, 46:108, 1958.
- G. Bono and R. F. Stellingwerf. Pulsation and stability of RR Lyrae stars. 1: Instability strip. *Astrophysical Journal, Supplement*, 93:233–269, July 1994. doi: 10.1086/192054.
- G. Bono, F. Caputo, S. Cassisi, R. Incerpi, and M. Marconi. Metal-rich RR Lyrae Variables. II. The Pulsational Scenario. *Astrophysical Journal*, 483:811–825, July 1997a. doi: 10.1086/304284.
- G. Bono, F. Caputo, V. Castellani, and M. Marconi. Nonlinear investigation of the pulsational properties of RR Lyrae variables. *Astronomy and Astrophysics, Supplement*, 121:327–342, February 1997b. doi: 10.1051/aas:1997289.
- G. Bono, F. Caputo, V. Castellani, and M. Marconi. Theoretical Models for Classical Cepheids. II. Period-Luminosity, Period-Color, and Period-Luminosity-Color Relations. *Astrophysical Journal*, 512:711–723, February 1999a. doi: 10.1086/306815.
- G. Bono, M. Marconi, and R. F. Stellingwerf. Classical Cepheid Pulsation Models. I. Physical Structure. *Astrophysical Journal, Supplement*, 122:167–205, May 1999b. doi: 10.1086/313207.

-
- G. Bono, F. Caputo, V. Castellani, M. Marconi, and J. Storm. Theoretical insights into the RR Lyrae K-band period-luminosity relation. *Monthly Notices of the RAS*, 326:1183–1190, September 2001. doi: 10.1046/j.1365-8711.2001.04655.x.
- G. Bono, M. Marconi, S. Cassisi, F. Caputo, W. Gieren, and G. Pietrzynski. Classical Cepheid Pulsation Models. X. The Period-Age Relation. *Astrophysical Journal*, 621:966–977, March 2005. doi: 10.1086/427744.
- G. Bono, F. Caputo, and V. Castellani. Stellar pulsation and evolution: a stepping-stone to match reality. *Mem. Societa Astronomica Italiana*, 77:207, 2006.
- G. Bono, F. Caputo, M. Marconi, and I. Musella. Insights into the Cepheid Distance Scale. *Astrophysical Journal*, 715:277–291, May 2010. doi: 10.1088/0004-637X/715/1/277.
- E. F. Borra and D. Deschatelets. Measurements of microturbulence of Cepheids using the autocorrelation function. *ArXiv e-prints*, July 2017.
- J. Breitter, P. Kervella, A. Mérand, A. Gallenne, L. Szabados, R. I. Anderson, M. Willson, and J.-B. Le Bouquin. Observational calibration of the projection factor of Cepheids. I. The type II Cepheid κ Pavonis. *Astronomy and Astrophysics*, 576:A64, April 2015. doi: 10.1051/0004-6361/201425171.
- J. Breitter, A. Mérand, P. Kervella, A. Gallenne, L. Szabados, R. I. Anderson, and J.-B. Le Bouquin. Observational calibration of the projection factor of Cepheids. II. Application to nine Cepheids with HST/FGS parallax measurements. *Astronomy and Astrophysics*, 587:A117, March 2016. doi: 10.1051/0004-6361/201527030.
- A. Bressan, P. Marigo, L. Girardi, B. Salasnich, C. Dal Cero, S. Rubele, and A. Nanni. PARSEC: stellar tracks and isochrones with the PAdova and TRieste Stellar Evolution Code. *Monthly Notices of the RAS*, 427:127–145, November 2012. doi: 10.1111/j.1365-2966.2012.21948.x.
- G. Burki, M. Mayor, and W. Benz. The peculiar classical Cepheid HR 7308. *Astronomy and Astrophysics*, 109:258–270, May 1982.
- E. Caffau and H.-G. Ludwig. The forbidden 1082 nm line of sulphur: the photospheric abundance of sulphur in the Sun and 3D effects. *Astronomy and Astrophysics*, 467:L11–L14, May 2007. doi: 10.1051/0004-6361:20077234.
- E. Caffau, E. Maiorca, P. Bonifacio, R. Faraggiana, M. Steffen, H.-G. Ludwig, I. Kamp, and M. Busso. The solar photospheric nitrogen abundance. Analysis of atomic transitions with 3D and 1D model atmospheres. *Astronomy and Astrophysics*, 498:877–884, May 2009. doi: 10.1051/0004-6361/200810859.
- E. Caffau, H.-G. Ludwig, M. Steffen, B. Freytag, and P. Bonifacio. Solar Chemical Abundances Determined with a CO5BOLD 3D Model Atmosphere. *Solar Physics*, 268:255–269, February 2011. doi: 10.1007/s11207-010-9541-4.

-
- J. A. Carroll. The form of an absorption line in the spectrum of a rotating or expanding star. *Monthly Notices of the RAS*, 88:548–555, May 1928. doi: 10.1093/mnras/88.7.548.
- R. F. Christy. Energy Transport in the Hydrogen Ionization Zone of Giant Stars. *Astrophysical Journal*, 136:887, November 1962. doi: 10.1086/147443.
- R. F. Christy. The Calculation of Stellar Pulsation. *Reviews of Modern Physics*, 36:555–571, April 1964. doi: 10.1103/RevModPhys.36.555.
- R. F. Christy. The Theory of Cepheid Variability. *Quarterly Journal of the RAS*, 9:13, March 1968.
- I. M. Coulson and J. A. R. Caldwell. Photometry and radial velocities of 27 southern galactic Cepheids. *South African Astronomical Observatory Circular*, 9, 1985.
- A. N. Cox, R. R. Brownlee, and D. D. Eilers. Time-Dependent Method for Computation of Radiation Diffusion and Hydro-Dynamics. *Astrophysical Journal*, 144:1024, June 1966. doi: 10.1086/148701.
- R. da Silva, B. Lemasle, G. Bono, K. Genovali, A. McWilliam, S. Cristallo, M. Bergemann, R. Buonanno, M. Fabrizio, I. Ferraro, P. François, G. Iannicola, L. Inno, C. D. Laney, R.-P. Kudritzki, N. Matsunaga, M. Nonino, F. Primas, N. Przybilla, M. Romaniello, F. Thévenin, and M. A. Urbaneja. Neutron-capture elements across the Galactic thin disk using Cepheids. *Astronomy and Astrophysics*, 586:A125, February 2016. doi: 10.1051/0004-6361/201527300.
- R. S. de Jong, S. Barden, O. Bellido-Tirado, J. Brynnel, C. Chiappini, É. Depagne, R. Haynes, D. Johl, D. P. Phillips, O. Schnurr, A. D. Schwobe, J. Walcher, S. M. Bauer, G. Cescutti, M.-R. L. Cioni, F. Dionies, H. Enke, D. M. Haynes, A. Kelz, F. S. Kitaura, G. Lamer, I. Minchev, V. Müller, S. E. Nuza, J.-C. Olaya, T. Piffl, E. Popow, A. Saviuk, M. Steinmetz, U. Ural, M. Valentini, R. Winkler, L. Wisotzki, W. R. Ansorge, M. Banerji, E. Gonzalez Solares, M. Irwin, R. C. Kennicutt, D. M. P. King, R. McMahon, S. Koposov, I. R. Parry, X. Sun, N. A. Walton, G. Finger, O. Iwert, M. Krumpe, J.-L. Lizon, V. Mainieri, J.-P. Amans, P. Bonifacio, M. Cohen, P. François, P. Jagourel, S. B. Mignot, F. Royer, P. Sartoretti, R. Bender, H.-J. Hess, F. Lang-Bardl, B. Muschielok, J. Schlichter, H. Böhringer, T. Boller, A. Bongiorno, M. Brusa, T. Dwelly, A. Merloni, K. Nandra, M. Salvato, J. H. Pragt, R. Navarro, G. Gerlofsma, R. Roelfsema, G. B. Dalton, K. F. Middleton, I. A. Tosh, C. Boeche, E. Caffau, N. Christlieb, E. K. Grebel, C. J. Hansen, A. Koch, H.-G. Ludwig, H. Mandel, A. Quirrenbach, L. Sbordone, W. Seifert, G. Thimm, A. Helmi, S. C. trager, T. Bensby, S. Feltzing, G. Ruchti, B. Edvardsson, A. Korn, K. Lind, W. Boland, M. Colless, G. Frost, J. Gilbert, P. Gillingham, J. Lawrence, N. Legg, W. Saunders, A. Sheinis, S. Driver, A. Robotham, R. Bacon, P. Caillier, J. Kosmalski, F. Laurent, and J. Richard. 4MOST: 4-metre Multi-Object Spectroscopic Telescope. In *Ground-based and Airborne Instrumentation for Astronomy V*, volume 9147 of *Proceedings of the SPIE*, page 91470M, July 2014. doi: 10.1117/12.2055826.
- V. Dobrovolskas, A. Kučinskas, M. Steffen, H.-G. Ludwig, D. Prakashavičius, J. Klevas, E. Caffau, and P. Bonifacio. Three-dimensional hydrodynamical CO⁵BOLD model atmospheres of red

-
- giant stars. III. Line formation in the atmospheres of giants located close to the base of the red giant branch. *Astronomy and Astrophysics*, 559:A102, November 2013. doi: 10.1051/0004-6361/201321036.
- M. R. Drout, A. L. Piro, B. J. Shappee, C. D. Kilpatrick, J. D. Simon, C. Contreras, D. A. Coulter, R. J. Foley, M. R. Siebert, N. Morrell, K. Boutsia, F. Di Mille, T. W.-S. Holoiën, D. Kasen, J. A. Kollmeier, B. F. Madore, A. J. Monson, A. Murguía-Berthier, Y.-C. Pan, J. X. Prochaska, E. Ramirez-Ruiz, A. Rest, C. Adams, K. Alatalo, E. Bañados, J. Baughman, T. C. Beers, R. A. Bernstein, T. Bitsakis, A. Campillay, T. T. Hansen, C. R. Higgs, A. P. Ji, G. Maravelias, J. L. Marshall, C. Moni Bidin, J. L. Prieto, K. C. Rasmussen, C. Rojas-Bravo, A. L. Strom, N. Ulloa, J. Vargas-González, Z. Wan, and D. D. Whitten. Light Curves of the Neutron Star Merger GW170817/SSS17a: Implications for R-Process Nucleosynthesis. *ArXiv e-prints*, October 2017.
- A. S. Eddington. The pulsation theory of Cepheid variables. *The Observatory*, 40:290–293, August 1917.
- A. S. Eddington. *The Internal Constitution of the Stars*. 1926.
- J. Engel, M. Bender, J. Dobaczewski, W. Nazarewicz, and R. Surman. β decay rates of r-process waiting-point nuclei in a self-consistent approach. *Physical Review C*, 60(1):014302, July 1999. doi: 10.1103/PhysRevC.60.014302.
- P. Feautrier. A Procedure for computing the Mean Intensity and the Flux. *SAO Special Report*, 167: 80, December 1964.
- M. U. Feuchtinger. A nonlinear model for RR Lyrae double mode pulsation. *Astronomy and Astrophysics*, 337:L29–L33, September 1998.
- B. D. Fields and K. A. Olive. The evolution of ${}^6\text{Li}$ in standard cosmic-ray nucleosynthesis. *New Astronomy*, 4:255–263, July 1999. doi: 10.1016/S1384-1076(99)00009-3.
- A. J. Fleischer, A. Gauger, and E. Sedlmayr. Circumstellar dust shells around long-period variables. I - Dynamical models of C-stars including dust formation, growth and evaporation. *Astronomy and Astrophysics*, 266:321–339, December 1992.
- A. B. Fokin. On hydrogen line formation in the atmospheres of pulsating giants. *Monthly Notices of the RAS*, 250:258–269, May 1991. doi: 10.1093/mnras/250.2.258.
- A. B. Fokin and D. Gillet. Theoretical interpretation of the metallic line doubling phenomenon in the variable star RR Lyrae. *Astronomy and Astrophysics*, 325:1013–1024, September 1997.
- A. B. Fokin, D. Gillet, and M. G. Breitfellner. Pulsating motions and turbulence in δ Cephei. *Astronomy and Astrophysics*, 307:503–515, March 1996.
- A. B. Fokin, D. Gillet, and M. Chadid. Shock waves and microturbulence in RR Lyrae. *Astronomy and Astrophysics*, 344:930–934, April 1999.

-
- B.-Q. For, C. Sneden, and G. W. Preston. The Chemical Compositions of Variable Field Horizontal-branch Stars: RR Lyrae Stars. *Astrophysical Journal, Supplement*, 197:29, December 2011. doi: 10.1088/0067-0049/197/2/29.
- P. Fouque and W. P. Gieren. An improved calibration of Cepheid visual and infrared surface brightness relations from accurate angular diameter measurements of cool giants and supergiants. *Astronomy and Astrophysics*, 320:799–810, April 1997.
- C. Freiburghaus, T. Rauscher, F.-K. Thielemann, K.-L. Kratz, and B. Pfeiffer. The r-Process in the High Entropy Bubble. *Nuclear Physics A*, 621:405–408, February 1997. doi: 10.1016/S0375-9474(97)00280-7.
- C. Freiburghaus, J.-F. Rembges, T. Rauscher, E. Kolbe, F.-K. Thielemann, K.-L. Kratz, B. Pfeiffer, and J. J. Cowan. The Astrophysical r-Process: A Comparison of Calculations following Adiabatic Expansion with Classical Calculations Based on Neutron Densities and Temperatures. *Astrophysical Journal*, 516:381–398, May 1999a. doi: 10.1086/307072.
- C. Freiburghaus, S. Rosswog, and F.-K. Thielemann. R-Process in Neutron Star Mergers. *Astrophysical Journal, Letters*, 525:L121–L124, November 1999b. doi: 10.1086/312343.
- B. Freytag, M. Steffen, H.-G. Ludwig, S. Wedemeyer-Böhm, W. Schaffner-Bergner, and O. Steiner. Simulations of stellar convection with CO5BOLD. *Journal of Computational Physics*, 231:919–959, February 2012. doi: 10.1016/j.jcp.2011.09.026.
- B. Freytag, S. Liljegren, and S. Höfner. Global 3D radiation-hydrodynamics models of AGB stars. Effects of convection and radial pulsations on atmospheric structures. *Astronomy and Astrophysics*, 600:A137, April 2017. doi: 10.1051/0004-6361/201629594.
- G. M. Fuller and B. S. Meyer. Neutrino Capture and Supernova Nucleosynthesis. *Astrophysical Journal*, 453:792, November 1995. doi: 10.1086/176442.
- A. J. Gallagher, M. Steffen, E. Caffau, P. Bonifacio, H.-G. Ludwig, and B. Freytag. Enhanced methods for computing spectra from CO5BOLD models using Linfor3D. Molecular bands in metal-poor stars. *ArXiv e-prints*, October 2016.
- A. J. Gallagher, M. Steffen, E. Caffau, P. Bonifacio, H.-G. Ludwig, and B. Freytag. Enhanced methods for computing spectra from CO5BOLD models using Linfor3D. Molecular bands in metal-poor stars. *Mem. Societa Astronomica Italiana*, 88:82, 2017.
- G. Gamow. Expanding Universe and the Origin of Elements. *Physical Review*, 70:572–573, October 1946. doi: 10.1103/PhysRev.70.572.2.
- A. Gautschi. On the Baade-Wesselink method. *Vistas in Astronomy*, 30:197–241, 1987. doi: 10.1016/0083-6656(87)90002-X.

-
- K. Genovali, B. Lemasle, G. Bono, M. Romaniello, F. Primas, M. Fabrizio, R. Buonanno, P. François, L. Inno, C. D. Laney, N. Matsunaga, S. Pedicelli, and F. Thévenin. On the metallicity distribution of classical Cepheids in the Galactic inner disk. *Astronomy and Astrophysics*, 554:A132, June 2013. doi: 10.1051/0004-6361/201321650.
- K. Genovali, B. Lemasle, G. Bono, M. Romaniello, M. Fabrizio, I. Ferraro, G. Iannicola, C. D. Laney, M. Nonino, M. Bergemann, R. Buonanno, P. François, L. Inno, R.-P. Kudritzki, N. Matsunaga, S. Pedicelli, F. Primas, and F. Thévenin. On the fine structure of the Cepheid metallicity gradient in the Galactic thin disk. *Astronomy and Astrophysics*, 566:A37, June 2014. doi: 10.1051/0004-6361/201323198.
- K. Genovali, B. Lemasle, R. da Silva, G. Bono, M. Fabrizio, M. Bergemann, R. Buonanno, I. Ferraro, P. François, G. Iannicola, L. Inno, C. D. Laney, R.-P. Kudritzki, N. Matsunaga, M. Nonino, F. Primas, M. Romaniello, M. A. Urbaneja, and F. Thévenin. On the α -element gradients of the Galactic thin disk using Cepheids. *Astronomy and Astrophysics*, 580:A17, August 2015. doi: 10.1051/0004-6361/201525894.
- W. P. Gieren, T. G. Barnes, III, and T. J. Moffett. The period-radius relation for classical Cepheids from the visual surface brightness technique. *Astrophysical Journal*, 342:467–475, July 1989. doi: 10.1086/167606.
- D. Gillet, J. F. Debieve, A. B. Fokin, and S. Mazauric. Turbulence amplification in the atmosphere of pulsating stars: a first approach. *Astronomy and Astrophysics*, 332:235–244, April 1998.
- D. Gillet, A. B. Fokin, M. G. Breitfellner, S. Mazauric, and A. Nicolas. Turbulence variation in the atmosphere of delta Cephei. *Astronomy and Astrophysics*, 344:935–941, April 1999.
- D. Gillet, N. Fabas, and A. Lèbre. First detection of helium emissions in RR Lyrae. *Astronomy and Astrophysics*, 553:A59, May 2013. doi: 10.1051/0004-6361/201220835.
- G. Gilmore, S. Randich, M. Asplund, J. Binney, P. Bonifacio, J. Drew, S. Feltzing, A. Ferguson, R. Jeffries, G. Micela, and et al. The Gaia-ESO Public Spectroscopic Survey. *The Messenger*, 147: 25–31, March 2012.
- D. O. Gough, J. P. Ostriker, and R. S. Stobie. On the Periods of Pulsating Stars. *Astrophysical Journal*, 142:1649–1652, November 1965. doi: 10.1086/148450.
- D. F. Gray. *The observation and analysis of stellar photospheres*. 1992.
- D. F. Gray. Spectral line-depth ratios as temperature indicators for cool stars. *Publications of the ASP*, 106:1248–1257, December 1994. doi: 10.1086/133502.
- D. F. Gray and K. Brown. Line-Depth Ratios: Temperature Indices for Giant Stars. *Publications of the ASP*, 113:723–735, June 2001. doi: 10.1086/320811.

-
- D. F. Gray and H. L. Johanson. Precise measurement of stellar temperatures using line-depth ratios. *Publications of the ASP*, 103:439–443, May 1991. doi: 10.1086/132839.
- M. A. T. Groenewegen. Baade-Wesselink distances to Galactic and Magellanic Cloud Cepheids and the effect of metallicity. *Astronomy and Astrophysics*, 550:A70, February 2013. doi: 10.1051/0004-6361/201220446.
- B. Gustafsson, B. Edvardsson, K. Eriksson, U. G. Jørgensen, Å. Nordlund, and B. Plez. A grid of MARCS model atmospheres for late-type stars. I. Methods and general properties. *Astronomy and Astrophysics*, 486:951–970, August 2008. doi: 10.1051/0004-6361:200809724.
- U. Heiter and K. Eriksson. Geometry of giant star model atmospheres: a consistency test. *Astronomy and Astrophysics*, 452:1039–1048, June 2006. doi: 10.1051/0004-6361:20064925.
- N. Hernitschek, E. F. Schlafly, B. Sesar, H.-W. Rix, D. W. Hogg, Z. Ivezić, E. K. Grebel, E. F. Bell, N. F. Martin, W. S. Burgett, H. Flewelling, K. W. Hodapp, N. Kaiser, E. A. Magnier, N. Metcalfe, R. J. Wainscoat, and C. Waters. VizieR Online Data Catalog: QSOs and RR Lyrae in Pan-STARRS1 3π Data (Hernitschek+ 2016). *VizieR Online Data Catalog*, 181, April 2016.
- N. Hernitschek, B. Sesar, H.-W. Rix, V. Belokurov, D. Martinez-Delgado, N. F. Martin, N. Kaiser, K. Hodapp, K. C. Chambers, R. Wainscoat, E. Magnier, R.-P. Kudritzki, N. Metcalfe, and P. W. Draper. The Geometry of Sagittarius Stream from Pan-STARRS1 3π RR Lyrae. *ArXiv e-prints*, October 2017.
- S. Hoefner and E. A. Dorfi. Dust formation in winds of long-period variables. IV. Atmospheric dynamics and mass loss. *Astronomy and Astrophysics*, 319:648–654, March 1997.
- S. Hoefner, M. U. Feuchtinger, and E. A. Dorfi. Dust formation in winds of long-period variables. III. Dynamical models and confirmation of a dust-induced κ -mechanism. *Astronomy and Astrophysics*, 297:815, May 1995.
- S. Hoefner, U. G. Jørgensen, R. Loidl, and B. Aringer. Dynamic model atmospheres of AGB stars. I. Atmospheric structure and dynamics. *Astronomy and Astrophysics*, 340:497–507, December 1998.
- E. Hubble. A Relation between Distance and Radial Velocity among Extra-Galactic Nebulae. *Proceedings of the National Academy of Science*, 15:168–173, March 1929. doi: 10.1073/pnas.15.3.168.
- P. Kervella, N. Nardetto, D. Bersier, D. Mourard, and V. Coudé du Foresto. Cepheid distances from infrared long-baseline interferometry. I. VINCI/VLTI observations of seven Galactic Cepheids. *Astronomy and Astrophysics*, 416:941–953, March 2004. doi: 10.1051/0004-6361:20031743.
- H. Kjeldsen and T. R. Bedding. Amplitudes of stellar oscillations: the implications for asteroseismology. *Astronomy and Astrophysics*, 293:87–106, January 1995.

-
- A. J. Korn, J. Shi, and T. Gehren. Kinetic equilibrium of iron in the atmospheres of cool stars. III. The ionization equilibrium of selected reference stars. *Astronomy and Astrophysics*, 407: 691–703, August 2003. doi: 10.1051/0004-6361:20030907.
- G. Kovacs, E. G. Kisvarsanyi, and J. R. Buchler. Cepheid radial velocity curves revisited. *Astrophysical Journal*, 351:606–616, March 1990. doi: 10.1086/168499.
- V. V. Kovtyukh. High-precision effective temperatures of 161 FGK supergiants from line-depth ratios. *Monthly Notices of the RAS*, 378:617–624, June 2007. doi: 10.1111/j.1365-2966.2007.11804.x.
- V. V. Kovtyukh and N. I. Gorlova. Precise temperatures of classical Cepheids and yellow supergiants from line-depth ratios. *Astronomy and Astrophysics*, 358:587–592, June 2000.
- V. V. Kovtyukh, S. M. Andrievsky, S. I. Belik, and R. E. Luck. Phase-dependent Variation of the Fundamental Parameters of Cepheids. II. Periods Longer than 10 Days. *Astronomical Journal*, 129:433–453, January 2005. doi: 10.1086/426339.
- V. V. Kovtyukh, C. Soubiran, O. Bienaymé, T. V. Mishenina, and S. I. Belik. High-precision effective temperatures of 215 FGK giants from line-depth ratios. *Monthly Notices of the RAS*, 371:879–884, September 2006. doi: 10.1111/j.1365-2966.2006.10719.x.
- R. Kuhfuss. A model for time-dependent turbulent convection. *Astronomy and Astrophysics*, 160: 116–120, May 1986.
- R. L. Kurucz. Model Atmospheres for Population Synthesis. In B. Barbuy and A. Renzini, editors, *The Stellar Populations of Galaxies*, volume 149 of *IAU Symposium*, page 225, 1992.
- A. Kučinskas, M. Steffen, H.-G. Ludwig, V. Dobrovolskas, A. Ivanauskas, J. Klevas, D. Prakashavičius, E. Caffau, and P. Bonifacio. Three-dimensional hydrodynamical CO⁵BOLD model atmospheres of red giant stars. II. Spectral line formation in the atmosphere of a giant located near the RGB tip. *Astronomy and Astrophysics*, 549:A14, January 2013. doi: 10.1051/0004-6361/201220240.
- L. D. Landau and E. M. Lifshitz. *Fluid mechanics*. 1959.
- C. D. Laney and R. S. Stobie. JHKL observations of galactic Cepheids. *Astronomy and Astrophysics, Supplement*, 93:93–120, April 1992.
- A. C. Layden, R. B. Hanson, S. L. Hawley, A. R. Klemola, and C. J. Hanley. The Absolute Magnitude and Kinematics of RR Lyrae Stars Via Statistical Parallax. *Astronomical Journal*, 112:2110, November 1996. doi: 10.1086/118167.
- H. S. Leavitt. 1777 variables in the Magellanic Clouds. *Annals of Harvard College Observatory*, 60: 87–108.3, 1908.
- H. S. Leavitt and E. C. Pickering. Periods of 25 Variable Stars in the Small Magellanic Cloud. *Harvard College Observatory Circular*, 173:1–3, March 1912.

-
- G. Lemaître. Un Univers homogène de masse constante et de rayon croissant rendant compte de la vitesse radiale des nébuleuses extra-galactiques. *Annales de la Société Scientifique de Bruxelles*, 47:49–59, 1927.
- B. Lemasle, P. François, G. Bono, M. Mottini, F. Primas, and M. Romaniello. Detailed chemical composition of Galactic Cepheids. A determination of the Galactic abundance gradient in the 8-12 kpc region. *Astronomy and Astrophysics*, 467:283–294, May 2007. doi: 10.1051/0004-6361:20066375.
- B. Lemasle, P. François, A. Piersimoni, S. Pedicelli, G. Bono, C. D. Laney, F. Primas, and M. Romaniello. Galactic abundance gradients from Cepheids. On the iron abundance gradient around 10-12 kpc. *Astronomy and Astrophysics*, 490:613–623, November 2008. doi: 10.1051/0004-6361:200810192.
- B. Lemasle, P. François, K. Genovali, V. V. Kovtyukh, G. Bono, L. Inno, C. D. Laney, L. Kaper, M. Bergemann, M. Fabrizio, N. Matsunaga, S. Pedicelli, F. Primas, and M. Romaniello. Galactic abundance gradients from Cepheids. α and heavy elements in the outer disk. *Astronomy and Astrophysics*, 558:A31, October 2013. doi: 10.1051/0004-6361/201322115.
- B. Lemasle, M. A. T. Groenewegen, E. K. Grebel, G. Bono, G. Fiorentino, P. François, L. Inno, V. V. Kovtyukh, N. Matsunaga, S. Pedicelli, F. Primas, J. Pritchard, M. Romaniello, and R. da Silva. Detailed chemical composition of classical Cepheids in the LMC cluster NGC 1866 and in the field of the SMC. *ArXiv e-prints*, September 2017.
- R. E. Luck and S. M. Andrievsky. Phase-dependent Variation of the Fundamental Parameters of Cepheids. I. Periods from 6 to 10 Days. *Astronomical Journal*, 128:343–356, July 2004. doi: 10.1086/420991.
- R. E. Luck, T. J. Moffett, T. G. Barnes, III, and W. P. Gieren. Magellanic Cloud Cepheids - Abundances. *Astronomical Journal*, 115:605, February 1998. doi: 10.1086/300227.
- R. E. Luck, S. M. Andrievsky, A. Fokin, and V. V. Kovtyukh. Phase-Dependent Variation of the Fundamental Parameters of Cepheids. Iv. s-CEPHEIDS. *Astronomical Journal*, 136:98–110, July 2008. doi: 10.1088/0004-6256/136/1/98.
- R. E. Luck, S. M. Andrievsky, V. V. Kovtyukh, W. Gieren, and D. Graczyk. The Distribution of the Elements in the Galactic Disk. II. Azimuthal and Radial Variation in Abundances from Cepheids. *Astronomical Journal*, 142:51, August 2011. doi: 10.1088/0004-6256/142/2/51.
- H.-G. Ludwig and A. Kučinskas. Three-dimensional hydrodynamical CO⁵BOLD model atmospheres of red giant stars. I. Atmospheric structure of a giant located near the RGB tip. *Astronomy and Astrophysics*, 547:A118, November 2012. doi: 10.1051/0004-6361/201220264.
- H.-G. Ludwig, B. Freytag, and M. Steffen. A calibration of the mixing-length for solar-type stars based on hydrodynamical simulations. I. Methodical aspects and results for solar metallicity. *Astronomy and Astrophysics*, 346:111–124, June 1999.

-
- H.-G. Ludwig, F. Allard, and P. H. Hauschildt. Numerical simulations of surface convection in a late M-dwarf. *Astronomy and Astrophysics*, 395:99–115, November 2002. doi: 10.1051/0004-6361:20021153.
- M. Marconi, I. Musella, and G. Fiorentino. Cepheid pulsation models at varying metallicity and y/z . *The Astrophysical Journal*, 632(1):590, 2005. URL <http://stacks.iop.org/0004-637X/632/i=1/a=590>.
- M. Marconi, I. Musella, and G. Fiorentino. Cepheid Pulsation Models at Varying Metallicity and $\Delta Y/\Delta Z$. *Astrophysical Journal*, 632:590–610, October 2005. doi: 10.1086/432790.
- M. Marconi, I. Musella, G. Fiorentino, G. Clementini, A. Aloisi, F. Annibali, R. Contreras Ramos, A. Saha, M. Tosi, and R. P. van der Marel. Pulsation Models for Ultra-low ($Z = 0.0004$) Metallicity Classical Cepheids. *Astrophysical Journal*, 713:615–625, April 2010. doi: 10.1088/0004-637X/713/1/615.
- M. Marconi, G. Coppola, G. Bono, V. Braga, A. Pietrinferni, R. Buonanno, M. Castellani, I. Musella, V. Ripepi, and R. F. Stellingwerf. On a New Theoretical Framework for RR Lyrae Stars. I. The Metallicity Dependence. *Astrophysical Journal*, 808:50, July 2015. doi: 10.1088/0004-637X/808/1/50.
- R. P. Martin, S. M. Andrievsky, V. V. Kovtyukh, S. A. Korotin, I. A. Yegorova, and I. Saviane. Oxygen, α -element and iron abundance distributions in the inner part of the Galactic thin disc. *Monthly Notices of the RAS*, 449:4071–4078, June 2015. doi: 10.1093/mnras/stv590.
- G. Martínez-Pinedo and K. Langanke. Shell-Model Half-Lives for $N = 82$ Nuclei and Their Implications for the r Process. *Physical Review Letters*, 83:4502–4505, November 1999. doi: 10.1103/PhysRevLett.83.4502.
- D. Mihalas. *Stellar atmospheres (2nd edition)*. 1978.
- E. Mundprecht, H. J. Muthsam, and F. Kupka. Multidimensional realistic modelling of Cepheid-like variables - I. Extensions of the ANTARES code. *Monthly Notices of the RAS*, 435:3191–3205, November 2013. doi: 10.1093/mnras/stt1511.
- E. Mundprecht, H. J. Muthsam, and F. Kupka. Multidimensional realistic modelling of Cepheid-like variables - II. Analysis of a Cepheid model. *Monthly Notices of the RAS*, 449:2539–2552, May 2015. doi: 10.1093/mnras/stv434.
- N. Nardetto, A. Fokin, D. Mourard, P. Mathias, P. Kervella, and D. Bersier. Self consistent modelling of the projection factor for interferometric distance determination. *Astronomy and Astrophysics*, 428:131–137, December 2004. doi: 10.1051/0004-6361:20041419.
- N. Nardetto, D. Mourard, P. Kervella, P. Mathias, A. Mérand, and D. Bersier. High resolution spectroscopy for Cepheids distance determination. I. Line asymmetry. *Astronomy and Astrophysics*, 453:309–319, July 2006. doi: 10.1051/0004-6361:20054333.

-
- N. Nardetto, D. Mourard, P. Mathias, A. Fokin, and D. Gillet. High-resolution spectroscopy for Cepheids distance determination. II. A period-projection factor relation. *Astronomy and Astrophysics*, 471:661–669, August 2007. doi: 10.1051/0004-6361/20066853.
- N. Nardetto, W. Gieren, P. Kervella, P. Fouqué, J. Storm, G. Pietrzynski, D. Mourard, and D. Queloz. High-resolution spectroscopy for Cepheids distance determination. V. Impact of the cross-correlation method on the p-factor and the γ -velocities. *Astronomy and Astrophysics*, 502:951–956, August 2009. doi: 10.1051/0004-6361/200912333.
- N. Nardetto, P. Mathias, A. Fokin, E. Chapellier, G. Pietrzynski, W. Gieren, D. Graczyk, and D. Mourard. Understanding the dynamical structure of pulsating stars: The center-of-mass velocity and the Baade-Wesselink projection factor of the β Cephei star α Lupi. *Astronomy and Astrophysics*, 553:A112, May 2013. doi: 10.1051/0004-6361/201220644.
- N. Nardetto, E. Poretti, M. Rainer, A. Fokin, P. Mathias, R. I. Anderson, A. Gallenne, W. Gieren, D. Graczyk, P. Kervella, A. Mérand, D. Mourard, H. Neilson, G. Pietrzynski, B. Pilecki, and J. Storm. HARPS-N high spectral resolution observations of Cepheids I. The Baade-Wesselink projection factor of δ Cep revisited. *Astronomy and Astrophysics*, 597:A73, January 2017. doi: 10.1051/0004-6361/201629400.
- H. R. Neilson, N. Nardetto, C.-C. Ngeow, P. Fouqué, and J. Storm. Cepheid limb darkening, angular diameter corrections, and projection factor from static spherical model stellar atmospheres. *Astronomy and Astrophysics*, 541:A134, May 2012. doi: 10.1051/0004-6361/201118550.
- H. R. Neilson, A. C. Bisol, E. Guinan, and S. Engle. Pulsation Period Change and Classical Cepheids: Probing the Details of Stellar Evolution. In G. Meynet, C. Georgy, J. Groh, and P. Stee, editors, *New Windows on Massive Stars*, volume 307 of *IAU Symposium*, pages 224–225, January 2015. doi: 10.1017/S1743921314006802.
- J. M. Nemec, A. F. L. Nemec, and T. E. Lutz. Period-luminosity-metallicity relations, pulsation modes, absolute magnitudes, and distances for population 2 variable stars. *Astronomical Journal*, 108:222–246, July 1994. doi: 10.1086/117062.
- C.-C. Ngeow, M. Marconi, I. Musella, M. Cignoni, and S. M. Kanbur. Theoretical Cepheid Period-Luminosity and Period-Color Relations in Spitzer IRAC Bands. *Astrophysical Journal*, 745:104, February 2012. doi: 10.1088/0004-637X/745/2/104.
- Chow-Choong Ngeow, Marcella Marconi, Ilaria Musella, Michele Cignoni, and Shashi M. Kanbur. Theoretical cepheid period-luminosity and period-color relations in spitzer irac bands. *The Astrophysical Journal*, 745(2):104, 2012. URL <http://stacks.iop.org/0004-637X/745/i=2/a=104>.
- P. P. Parenago and B. V. Kukarkin. *Peremennye zvezdy*. 1947.

-
- S. B. Parsons. The Conversion Factor from Radial to Pulsational Velocity and the Radii of Classical Cepheids. *Astrophysical Journal*, 174:57, May 1972. doi: 10.1086/151468.
- S. Pedicelli, B. Lemasle, M. Groenewegen, M. Romaniello, G. Bono, C. D. Laney, P. François, R. Buonanno, F. Caputo, J. Lub, J. W. Pel, F. Primas, and J. Pritchard. New Baade-Wesselink distances and radii for four metal-rich Galactic Cepheids. *Astronomy and Astrophysics*, 518:A11, July 2010. doi: 10.1051/0004-6361/201014262.
- A. A. Penzias and R. W. Wilson. A Measurement of Excess Antenna Temperature at 4080 Mc/s. *Astrophysical Journal*, 142:419–421, July 1965. doi: 10.1086/148307.
- S. Perlmutter, G. Aldering, G. Goldhaber, R. A. Knop, P. Nugent, P. G. Castro, S. Deustua, S. Fabbro, A. Goobar, D. E. Groom, I. M. Hook, A. G. Kim, M. Y. Kim, J. C. Lee, N. J. Nunes, R. Pain, C. R. Pennypacker, R. Quimby, C. Lidman, R. S. Ellis, M. Irwin, R. G. McMahon, P. Ruiz-Lapuente, N. Walton, B. Schaefer, B. J. Boyle, A. V. Filippenko, T. Matheson, A. S. Fruchter, N. Panagia, H. J. M. Newberg, W. J. Couch, and T. S. C. Project. Measurements of Ω and Λ from 42 High-Redshift Supernovae. *Astrophysical Journal*, 517:565–586, June 1999. doi: 10.1086/307221.
- P. Pietrukowicz, W. A. Dziembowski, P. Mróz, I. Soszyński, A. Udalski, R. Poleski, M. K. Szymański, M. Kubiak, G. Pietrzyński, Ł. Wyrzykowski, K. Ulaczyk, S. Kozłowski, and J. Skowron. Large Variety of New Pulsating Stars in the OGLE-III Galactic Disk Fields. *Acta Astronomica*, 63:379–404, December 2013.
- P. Pietrukowicz, S. Kozłowski, J. Skowron, I. Soszyński, A. Udalski, R. Poleski, Ł. Wyrzykowski, M. K. Szymański, G. Pietrzyński, K. Ulaczyk, P. Mróz, D. M. Skowron, and M. Kubiak. Deciphering the 3D Structure of the Old Galactic Bulge from the OGLE RR Lyrae Stars. *Astrophysical Journal*, 811:113, October 2015. doi: 10.1088/0004-637X/811/2/113.
- P. Pietrukowicz, W. A. Dziembowski, M. Latour, R. Angeloni, R. Poleski, F. di Mille, I. Soszyński, A. Udalski, M. K. Szymański, Ł. Wyrzykowski, S. Kozłowski, J. Skowron, D. Skowron, P. Mróz, M. Pawlak, and K. Ulaczyk. Blue large-amplitude pulsators as a new class of variable stars. *Nature Astronomy*, 1:0166, August 2017. doi: 10.1038/s41550-017-0166.
- B. Pilecki, G. Pietrzyński, D. Graczyk, and W. Gieren. Cepheids in eclipsing binary systems. In A. Różańska and M. Bejger, editors, *37th Meeting of the Polish Astronomical Society*, volume 3, pages 31–34, June 2016.
- Planck Collaboration, P. A. R. Ade, N. Aghanim, M. Arnaud, M. Ashdown, J. Aumont, C. Baccigalupi, A. J. Banday, R. B. Barreiro, J. G. Bartlett, and et al. Planck 2015 results. XIII. Cosmological parameters. *Astronomy and Astrophysics*, 594:A13, September 2016. doi: 10.1051/0004-6361/201525830.
- F. Pont, M. Mayor, and G. Burki. New radial velocities for classical cepheids. Local galactic rotation revisited. *Astronomy and Astrophysics*, 285:415–439, May 1994.

-
- G. W. Preston. Helium lines in RR Lyrae spectra. *Astronomy and Astrophysics* , 507:1621–1624, December 2009. doi: 10.1051/0004-6361/200912984.
- G. W. Preston. RR Lyrae Atmospherics: Wrinkles Old and New. A Preview. *Astronomical Journal* , 141:6, January 2011. doi: 10.1088/0004-6256/141/1/6.
- V. C. Reddish. The period-luminosity relation and stellar composition. *Monthly Notices of the RAS* , 116:533, 1956. doi: 10.1093/mnras/116.5.533.
- A. G. Riess, L. M. Macri, S. L. Hoffmann, D. Scolnic, S. Casertano, A. V. Filippenko, B. E. Tucker, M. J. Reid, D. O. Jones, J. M. Silverman, R. Chornock, P. Challis, W. Yuan, P. J. Brown, and R. J. Foley. A 2.4% Determination of the Local Value of the Hubble Constant. *Astrophysical Journal* , 826:56, July 2016. doi: 10.3847/0004-637X/826/1/56.
- M. Romaniello, F. Primas, M. Mottini, M. Groenewegen, G. Bono, and P. François. The influence of chemical composition on the properties of Cepheid stars. I. Period-Luminosity relation vs. iron abundance. *Astronomy and Astrophysics* , 429:L37–L40, January 2005. doi: 10.1051/0004-6361:200400110.
- M. Romaniello, F. Primas, M. Mottini, S. Pedicelli, B. Lemasle, G. Bono, P. François, M. A. T. Groenewegen, and C. D. Laney. The influence of chemical composition on the properties of Cepheid stars. II. The iron content. *Astronomy and Astrophysics* , 488:731–747, September 2008. doi: 10.1051/0004-6361:20065661.
- C. N. Sabbey, D. D. Sasselov, M. S. Fieldus, J. B. Lester, K. A. Venn, and R. P. Butler. On Spectral Line Formation and Measurement in Cepheids: Implications to Distance Determination. *Astrophysical Journal* , 446:250, June 1995. doi: 10.1086/175783.
- D. Sasselov and M. Karovska. On Cepheid diameter and distance measurement. *Astrophysical Journal* , 432:367–372, September 1994. doi: 10.1086/174574.
- H. Shapley and S. B. Nicholson. On the Spectral Lines of a Pulsating Star. *Proceedings of the National Academy of Science*, 5:417–423, October 1919. doi: 10.1073/pnas.5.10.417.
- G. Shaviv and E. E. Salpeter. Convective Overshooting in Stellar Interior Models. *Astrophysical Journal* , 184:191–200, August 1973. doi: 10.1086/152318.
- L. Siess, M. Livio, and J. Lattanzio. Structure, Evolution, and Nucleosynthesis of Primordial Stars. *Astrophysical Journal* , 570:329–343, May 2002. doi: 10.1086/339733.
- M. S. Smith, L. H. Kawano, and R. A. Malaney. Experimental, computational, and observational analysis of primordial nucleosynthesis. *Astrophysical Journal, Supplement*, 85:219–247, April 1993. doi: 10.1086/191763.
- R. Smolec. Metallicity Dependence of the Blazhko Effect. *Acta Astronomica*, 55:59–84, March 2005.

-
- R. Smolec and P. Moskalik. Convective Hydrocodes for Radial Stellar Pulsation. Physical and Numerical Formulation. *Acta Astronomica*, 58:193–232, September 2008.
- I. Soszynski, R. Poleski, A. Udalski, M. K. Szymanski, M. Kubiak, G. Pietrzynski, L. Wyrzykowski, O. Szewczyk, and K. Ulaczyk. The Optical Gravitational Lensing Experiment. The OGLE-III Catalog of Variable Stars. I. Classical Cepheids in the Large Magellanic Cloud. *Acta Astronomica*, 58:163–185, September 2008.
- I. Soszyński, A. Udalski, M. K. Szymański, M. Kubiak, G. Pietrzyński, Ł. Wyrzykowski, O. Szewczyk, K. Ulaczyk, and R. Poleski. The Optical Gravitational Lensing Experiment. The OGLE-III Catalog of Variable Stars. II. Type II Cepheids and Anomalous Cepheids in the Large Magellanic Cloud. *Acta Astronomica*, 58:293, December 2008.
- I. Soszyński, R. Poleski, A. Udalski, M. K. Szymański, M. Kubiak, G. Pietrzyński, Ł. Wyrzykowski, O. Szewczyk, and K. Ulaczyk. The Optical Gravitational Lensing Experiment. The OGLE-III Catalog of Variable Stars. VII. Classical Cepheids in the Small Magellanic Cloud. *Acta Astronomica*, 60:17–39, March 2010a.
- I. Soszyński, A. Udalski, M. K. Szymański, M. Kubiak, G. Pietrzyński, Ł. Wyrzykowski, K. Ulaczyk, and R. Poleski. The Optical Gravitational Lensing Experiment. The OGLE-III Catalog of Variable Stars. VIII. Type II Cepheids in the Small Magellanic Cloud. *Acta Astronomica*, 60:91–107, June 2010b.
- I. Soszyński, A. Udalski, P. Pietrukowicz, M. K. Szymański, M. Kubiak, G. Pietrzyński, Ł. Wyrzykowski, K. Ulaczyk, R. Poleski, and S. Kozłowski. The Optical Gravitational Lensing Experiment. The OGLE-III Catalog of Variable Stars. XIV. Classical and Type II Cepheids in the Galactic Bulge. *Acta Astronomica*, 61:285–301, December 2011.
- I. Soszyński, A. Udalski, M. K. Szymański, Ł. Wyrzykowski, K. Ulaczyk, R. Poleski, P. Pietrukowicz, S. Kozłowski, D. M. Skowron, J. Skowron, P. Mróz, and M. Pawlak. The OGLE Collection of Variable Stars. Over 45 000 RR Lyrae Stars in the Magellanic System. *Acta Astronomica*, 66:131–147, June 2016.
- M. Steffen. A model atmosphere analysis of the F5 IV-V subgiant Procyon. *Astronomy and Astrophysics, Supplement*, 59:403–427, March 1985.
- M. Steffen, E. Caffau, and H.-G. Ludwig. Micro- and macroturbulence predictions from CO5BOLD 3D stellar atmospheres. *Memorie della Societa Astronomica Italiana Supplementi*, 24:37, 2013.
- R. F. Stellingwerf. Convection in pulsating stars. I - Nonlinear hydrodynamics. II - RR Lyrae convection and stability. *Astrophysical Journal*, 262:330–343, November 1982. doi: 10.1086/160425.
- D. W. N. Stibbs. On the differential galactic rotation of the system of cepheid variable stars. *Monthly Notices of the RAS*, 116:453, 1956. doi: 10.1093/mnras/116.4.453.

-
- R. S. Stobie. Cepheid pulsation-I. Numerical technique and test calculations. *Monthly Notices of the RAS*, 144:461, 1969a. doi: 10.1093/mnras/144.4.461.
- R. S. Stobie. Cepheid pulsation-II. Models fitted to evolutionary tracks. *Monthly Notices of the RAS*, 144:485, 1969b. doi: 10.1093/mnras/144.4.485.
- R. S. Stobie. Cepheid pulsation-III. Models fitted to a new mass-luminosity relation. *Monthly Notices of the RAS*, 144:511, 1969c. doi: 10.1093/mnras/144.4.511.
- J. Storm, W. Gieren, P. Fouqué, T. G. Barnes, G. Pietrzyński, N. Nardetto, M. Weber, T. Granzer, and K. G. Strassmeier. Calibrating the Cepheid period-luminosity relation from the infrared surface brightness technique. I. The p-factor, the Milky Way relations, and a universal K-band relation. *Astronomy and Astrophysics*, 534:A94, October 2011. doi: 10.1051/0004-6361/201117155.
- L. Szabados and P. Klagyivik. Observational studies of Cepheid amplitudes. II. Metallicity dependence of pulsation amplitudes. *Astronomy and Astrophysics*, 537:A81, January 2012. doi: 10.1051/0004-6361/201117815.
- P.-E. Tremblay, H.-G. Ludwig, M. Steffen, P. Bergeron, and B. Freytag. Solution to the problem of the surface gravity distribution of cool DA white dwarfs from improved 3D model atmospheres. *Astronomy and Astrophysics*, 531:L19, July 2011. doi: 10.1051/0004-6361/201117310.
- T. G. Tsvetkov. Population I pulsating stars. IV - Period-radius and period-gravity relations. *Astrophysics and Space Science*, 150:357–378, December 1988. doi: 10.1007/BF00641730.
- D. G. Turner. The Progenitors of Classical Cepheid Variables. *Journal of the RAS of Canada*, 90:82, April 1996.
- D. G. Turner, M. Abdel-Sabour Abdel-Latif, and L. N. Berdnikov. Rate of Period Change as a Diagnostic of Cepheid Properties. *Publications of the ASP*, 118:410–418, March 2006. doi: 10.1086/499501.
- D. G. Turner, D. J. Majaess, D. J. Lane, J. M. Rosvick, and A. A. B. D. D. Henden. The Galactic Calibration of the Cepheid Period-Luminosity Relation and its Implications for the Universal Distance Scale. *Odessa Astronomical Publications*, 23:119, December 2010.
- H. Umeda and K. Nomoto. First-generation black-hole-forming supernovae and the metal abundance pattern of a very iron-poor star. *Nature*, 422:871–873, April 2003. doi: 10.1038/nature01571.
- V. Vasilyev, H.-G. Ludwig, B. Freytag, B. Lemasle, and M. Marconi. Spectroscopic properties of a two-dimensional time-dependent Cepheid model. I. Description and validation of the model. *Astronomy and Astrophysics*, 606:A140, October 2017a. doi: 10.1051/0004-6361/201731422.
- V. Vasilyev, H.-G. Ludwig, B. Freytag, B. Lemasle, and M. Marconi. Spectroscopic properties of a two-dimensional time-dependent Cepheid model II. Determination of stellar parameters and abundances. *ArXiv e-prints*, November 2017b.

-
- J. Von Neumann and R. D. Richtmyer. A Method for the Numerical Calculation of Hydrodynamic Shocks. *Journal of Applied Physics*, 21:232–237, March 1950. doi: 10.1063/1.1699639.
- T. P. Walker, G. Steigman, H.-S. Kang, D. M. Schramm, and K. A. Olive. Primordial nucleosynthesis redux. *Astrophysical Journal*, 376:51–69, July 1991. doi: 10.1086/170255.
- G. Wallerstein. The Cepheids of Population II and Related Stars. *Publications of the ASP*, 114: 689–699, July 2002. doi: 10.1086/341698.
- D. L. Welch, F. Wieland, C. W. McAlary, R. McGonegal, B. F. Madore, R. A. McLaren, and G. Neugebauer. JHK observations of classical Cepheids. *Astrophysical Journal, Supplement*, 54:547–579, April 1984. doi: 10.1086/190943.
- A. J. Wesselink. The observations of brightness, colour and radial velocity of δ Cephei and the pulsation hypothesis (Errata: 10 258, 310). *Bulletin Astronomical Institute of the Netherlands*, 10:91, January 1946.
- R. Wielen. Space Velocities of Nearby Classical Cepheids. *Astronomy and Astrophysics, Supplement*, 15, April 1974.
- P. Wielgorski, G. Pietrzynski, W. Gieren, R.-P. Kudritzki, B. Zgirski, F. Bresolin, J. Storm, N. Matsumaga, D. Graczyk, and I. Soszynski. A precision determination of the metallicity effect on Cepheid absolute magnitudes in VIJHK bands from Magellanic Cloud Cepheids. *ArXiv e-prints*, May 2017.
- T. D. Wilson, T. G. Barnes, III, S. L. Hawley, and W. H. Jefferys. Absolute magnitudes and kinematic properties of Cepheids. *Astrophysical Journal*, 378:708–717, September 1991. doi: 10.1086/170472.
- S. A. Zhevakin. *Teoriia pul'satsionnoi zvezdnoi peremennosti*. 1957.
- S. A. Zhevakin. Physical Basis of the Pulsation Theory of Variable Stars. *Annual Review of Astron and Astrophys*, 1:367, 1963. doi: 10.1146/annurev.aa.01.090163.002055.
- D. B. Zucker, G. de Silva, K. Freeman, J. Bland-Hawthorn, and Hermes Team. The Galactic Archaeology with HERMES Survey. In W. Aoki, M. Ishigaki, T. Suda, T. Tsujimoto, and N. Arimoto, editors, *Galactic Archaeology: Near-Field Cosmology and the Formation of the Milky Way*, volume 458 of *Astronomical Society of the Pacific Conference Series*, page 421, August 2012.

ACKNOWLEDGEMENTS

First, I would like to thank Dr. Hans-Günter Ludwig for his guidance, encouragement, many interesting and helpful discussions. They allowed me to expand my knowledge and skills, to study better the subject as well as to understand aspects of the research work, and to develop as a scientist. I highly appreciate for his willingness to help me, helpful tips, enthusiasm and the research philosophy, which has inspired me.

My PhD thesis would not have been possible without support of the thesis committee members, namely, Prof. Dr. Hans-Walter Rix and Prof. Dr. Norbert Christlieb. I am grateful you for giving me the opportunity for this scientific research.

I would like to thank to my collaborators Dr. Bernd Freytag who has calculated the 2D model with the CO5BOLD code and gave helpful comments for my paper as well as Dr. Marcella Marconi for the help with nonlinear models. Also, I want to thank Dr. Bertrand Lemasle for valuable scientific comments for papers.

I am grateful to everyone from MPIA and LSW for the amazing inspiring atmosphere, interesting seminars and conversations as well as for Mirandella on Fridays.

I want to thank IMPRS and, particularly, Christian Fendt, for the organization of seminars, wonderful retreats, financial support to go to conferences conference, and help, when I had difficulties.

Thanks to Dr. Anish Amarsi and Diana for the valuable comments concerning the manuscript of the thesis, which have improved its content. I would like to thank my friend Michael for the translation of the abstract into German and for interesting discussions in mensa and the library.

My special thanks goes to Dr. Dima Semenov for winter trips to Schwarzwald as well as soulful discussions.

I also would like to thank my friends from MSU, Natasha and Misha for visiting me, wonderful trips, and support.

Thanks to my office mates from MPIA.

Ачай, авай, Санюк и Леңук, пеш кугу тау полшымыланда, чытымыланда неле жапыште. Олаш тунемаш колтымыланда, вара Москваш, вара Германийыш. Ачалан телескопым кондымылажлан кунам мый 5 ияш улам ыле, 1997 ийысе кометым, шўдыр-йўрым ончыктымылан. Тунам мый астрономийым йўратенам.

